

**Doctoral Dissertation**

**COUPLED DYNAMIC ANALYSIS AND STRUCTURAL DESIGN  
OF A PRESTRESSED CONCRETE SPAR FLOATER SUPPORTING A 10 MW FLOATING  
OFFSHORE WIND TURBINE**

**[10MW 級風車を搭載するプレストレストコンクリート製スパー型浮体の空力—流体力連  
成解析および構造設計]**

**by**

**WICHUDA MUNBUA**  
**(ウィチュダ- ムンブア)**

A dissertation submitted to  
Graduate School of Urban Innovation  
Yokohama National University  
in partial fulfillment of the requirements for the award of the degree of  
**Doctor of Philosophy in Engineering**

Supervised by

**Dr. CHIKAKO FUJIYAMA**

Assoc. Professor, Graduate School of Urban Innovation

**Yokohama National University**

**Yokohama, Japan**

**March 2023**

**Yokohama National University, Japan**  
**Graduate School of Urban Innovation**

This thesis, written by Wichuda Munbua has been accepted by her advisor and thesis committee members. And, it is presented to Graduate School of Urban Innovation, Yokohama National University, Japan, in partial fulfillment of the requirement for the degree of Doctor of Philosophy in Engineering.

**Committee members:**

Assoc. Prof. Dr. Chikako Fujiyama, chair and academic supervisor

Graduate School of Urban Innovation, Yokohama National University, Japan

Prof. Dr. Koichi Maekawa, member

Graduate School of Urban Innovation, Yokohama National University, Japan

Prof. Dr. Akira Hosoda, member

Graduate School of Urban Innovation, Yokohama National University, Japan

Prof. Dr. Hitoshi Yamada, member

Graduate School of Urban Innovation, Yokohama National University, Japan

Prof. Dr. Motohiko Murai, member

Graduate School of Engineering Science, Yokohama National University, Japan

© Wichuda Mumbua 2023

## **ACKNOWLEDGMENTS**

I would like to express my deepest gratitude and sincere appreciation to my research supervisor, Associate Professor Dr. Chikako Fujiyama, for the endless support and guidance, valuable suggestions, and encouragement throughout the course to the successful completion of the study. This dissertation would not have been accomplished without her enthusiasm and persistent supervision.

I am equally grateful to Assistant Professor Dr. Rodolfo T. Gonçalves, Department of System Innovation, The University of Tokyo, Japan, for his consistent advice and painstaking efforts to support me in mastering the process of numerical analysis and perform model testing of the structure under wave action. Without his constant encouragement, this research would not have been successful.

I am grateful to Professor Dr. Koichi Maekawa and Professor Dr. Akira Hosoda for providing me with valuable contributions and constructive comments during my study. I am equally thankful to Professor Dr. Motohiko Murai and Professor Dr. Hitoshi Yamada for their valuable advice and review of this dissertation.

I would like to thank Mr. Bartosz Stachowicz for implementing WAMIT and OpenFAST at the very beginning of this research. Only do we know each other through the online world, but his comprehensive advice and guideline lightened up this journey. I am equally grateful to Dr. Edgard B. Malta, Director, Tecnhomar Engenharia Oceânica, Brazil, for his support in utilizing WAMIT and OpenFAST to perform the hydrodynamic, aerodynamic, and coupled dynamic analyses. Special thanks to Dr. Nguyen Huu Quoc Hung for his consistent friendly advice on implementing finite element code COM3D.

My appreciation also goes to friends, colleagues, juniors, and members of the Concrete Laboratory of Yokohama National University; their friendship, kindness, laughing, and smiling made me precious memories of being a Ph.D. student in our laboratory. Special thanks to Ms. Emiko Ishii and Ms. Morosawa Kumiko for their support with administrative concerns.

Finally, I would like to dedicate this research work to my beloved family, a very special gratitude is offered to my other half, Premsan Invichai, the wind beneath my wings, for his love and endless support. My parents and my sister who are always constant sources of inspiration and encouragement throughout my life.

## TABLE OF CONTENTS

ACKNOWLEDGMENTS .....	iii
ABSTRACT .....	- 1 -
CHAPTER 1 .....	- 3 -
INTRODUCTION .....	- 3 -
1.1 Background and Motivation .....	- 3 -
1.2 Objectives / Target and Scope of the Study .....	- 5 -
1.3 Outline of the Dissertation .....	- 6 -
Nomenclature in Chapter 1 .....	- 7 -
References in Chapter 1 .....	- 7 -
CHAPTER 2 .....	- 10 -
THEORETICAL BACKGROUND .....	- 10 -
2.1 Introduction .....	- 10 -
2.2 Ocean Waves .....	- 10 -
2.3 Frequency and Time Domain of the Sea States .....	- 13 -
2.4 Definitions of Rigid-Body Motions .....	- 13 -
2.5 Floater Hydrostatics and Upright Stability .....	- 14 -
2.6 Floater Hydrodynamics .....	- 19 -
2.6.1 Potential Flow Theory .....	- 19 -
2.6.2 Wave loads on a Structure .....	- 21 -
2.6.3 Morison's Equation .....	- 22 -
2.7 Constitutive Modeling and Time-Dependent Mechanics of Structural Concrete .....	- 24 -

2.7.1 Elasto-Plastic and Fracturing Model in Compression .....	- 24 -
2.7.2 Model for Tension and Bond.....	- 26 -
2.7.3 Contact Density Model (Shear Transfer Model).....	- 29 -
2.8 Constitutive Model of Concrete with Multi-Directional Cracks .....	- 30 -
2.9 Constitutive Model of Concrete for High-Cycle Fatigue in Compression, Tension, and Shear .....	- 32 -
2.9.1 High Cycle Fatigue of Concrete in Compression .....	- 33 -
2.9.2 High Cycle Fatigue of Concrete in Tension .....	- 36 -
References in Chapter 2 .....	- 37 -
<b>CHAPTER 3 .....</b>	<b>- 41 -</b>
<b>COUPLED DYNAMIC ANALYSIS OF A FLOATING WIND TURBINE .....</b>	<b>- 41 -</b>
3.1 Introduction.....	- 41 -
3.2 Parametric Analysis .....	- 42 -
3.3 Sensitivity Analysis.....	- 43 -
3.4 Hydrostatic Modeling.....	- 44 -
3.5 Hydrostatic Equilibrium.....	- 46 -
3.6 Environmental Condition.....	- 47 -
3.6.1 Wave Condition.....	- 47 -
3.6.2 Wind Condition .....	- 49 -
3.7 Coupled Dynamic Analysis.....	- 49 -
3.7.1 Verification of Coupled Dynamic Model and Resonance Assessment.....	- 49 -
3.7.2 Spectral Analysis of Rigid Body Motion.....	- 50 -
3.8 Coupled Dynamic Analysis Results.....	- 52 -

3.9 Conclusion for Chapter 3 .....	- 57 -
Nomenclature in Chapter 3 .....	- 58 -
References in Chapter 3 .....	- 60 -
<b>CHAPTER 4 .....</b>	<b>- 62 -</b>
<b>MODEL TEST .....</b>	<b>- 62 -</b>
4.1 Introduction .....	- 62 -
4.2 Experiment Setup .....	- 62 -
4.2.1 Reduced Scale Model .....	- 62 -
4.2.2 Wave Tank Setup .....	- 64 -
4.2.3 Environmental Conditions .....	- 65 -
4.3 Response Motion of the Model .....	- 67 -
4.3.1 Free Vibration Tests .....	- 67 -
4.3.2 Experiments with Waves .....	- 70 -
4.3.3 Comparison of the Response Amplitude Operators (RAOs) .....	- 78 -
4.4 Conclusion for Chapter 4 .....	- 81 -
Nomenclature in Chapter 4 .....	- 82 -
References in Chapter 4 .....	- 82 -
<b>CHAPTER 5 .....</b>	<b>- 84 -</b>
<b>CONCRETE FINITE ELEMENT ANALYSIS AND STRUCTURAL DESIGN .....</b>	<b>- 84 -</b>
5.1 Introduction .....	- 84 -
5.2 Finite Element Model .....	- 84 -
5.3 Material and Boundary Condition .....	- 85 -

5.4 Hull Concrete under Water Pressure .....	- 87 -
5.4.1 Hydrostatic and Hydrodynamics Pressure .....	- 87 -
5.4.2 FE Analysis Results of Spar's Hull Concrete under Large Pressure .....	- 89 -
5.5 Hull Concrete's Sectional Design .....	- 90 -
5.5.1 Free Body Diagram .....	- 90 -
5.5.2 Design Flexural Bending Moment .....	- 91 -
5.5.3 Ultimate Moment Capacity of a Circular Section Prestressed Concrete .....	- 92 -
5.5.4 Interaction Diagram of the Section .....	- 94 -
5.6 Tower Connection and Fairlead Connection Design .....	- 96 -
5.6.1 Study Cases and Loading Conditions .....	- 96 -
5.6.2 FE Analysis and Preliminary Design of the Steel-Concrete Connections .....	- 97 -
5.6.3 Structural Behavior of the Five Study Cases .....	- 101 -
5.7 FE Analysis Results of a Proposed Concrete Spar .....	- 102 -
5.8 Advantages of the Proposed Concrete Spar .....	- 104 -
5.9 Conclusion for Chapter 5 .....	- 105 -
Nomenclature in Chapter 5 .....	- 106 -
References in Chapter 5 .....	- 108 -
CHAPTER 6 .....	- 109 -
PROPOSED FAIRLEAD CONNECTIONS .....	- 109 -
6.1 Introduction .....	- 109 -
6.2 FE Model .....	- 109 -
6.3 Five Types of Proposed Fairlead Connections .....	- 110 -



6.4 FE Analysis Results .....	- 112 -
6.4.1 Stress and Strain Distribution .....	- 112 -
6.5 Fatigue Analysis .....	- 114 -
6.5.1 Load Conditions .....	- 114 -
6.5.2 Fatigue Life Estimation .....	- 115 -
6.6 Conclusion for Chapter 6 .....	- 125 -
Nomenclature in Chapter 6 .....	- 126 -
References in Chapter 6 .....	- 127 -
CHAPTER 7 .....	- 129 -
CONCLUSIONS AND RECOMMENDATIONS .....	- 129 -
7.1 General Conclusions .....	- 129 -
7.2 Coupled Dynamic Analysis of a Floating Wind Turbine .....	- 129 -
7.3 Model Test .....	- 130 -
7.4 Concrete Finite Element Analysis and Structural Design .....	- 131 -
7.5 Proposed Fairlead Connections .....	- 132 -
7.6 Recommendations for the Future Study .....	- 133 -

## LIST OF FIGURES

FIGURE 2.1: A progressive wave definition.....	- 11 -
FIGURE 2.2: Definition of the rigid-body motion modes for a deep draft concrete floater.....	- 14 -
FIGURE 2.3: Stability conditions.....	- 15 -
FIGURE 2.4: Linear measurements in stability.....	- 16 -
FIGURE 2.5: Second moment of area: the moment of inertia of area .....	- 17 -
FIGURE 2.6: Moment of inertia of water plane area .....	- 17 -
FIGURE 2.7: Classification of wave forces.....	- 21 -
FIGURE 2.8: Concept of elasto-plastic fracture model of uncracked concrete .....	- 25 -
FIGURE 2.9: Uniaxial compression model parallel to crack.....	- 26 -
FIGURE 2.10: Stress distribution and space-averaged tension stiffening model .....	- 26 -
FIGURE 2.11: Tension softening curves adjusted based on finite element length.....	- 27 -
FIGURE 2.12: Re-contact model.....	- 27 -
FIGURE 2.13: Mechanism of bond and formation of tensile crack.....	- 28 -
FIGURE 2.14: Unique relation between bond stress, slip, and strain.....	- 28 -
FIGURE 2.15: Contact density of each direction.....	- 29 -
FIGURE 2.16: Shear transfer model for one-directional crack.....	- 30 -
FIGURE 2.17: Overview of the advanced RC model and multidirectional crack .....	- 31 -
FIGURE 2.18: Switch of coordinate with the active crack.....	- 32 -
FIGURE 2.19: Calculation of crack concrete based on the active crack.....	- 32 -

FIGURE 2.20: Constitutive laws of concrete structure for high-cycle fatigue.....	- 33 -
FIGURE 3.1: Interfacing modules employed to achieve coupled dynamics and concrete FE analyses...	- 41 -
FIGURE 3.2: Main dimensions and variables of the spar considered during the parametric analysis. ....	- 42 -
FIGURE 3.3: Sensitivity analysis of spar dimensions at different hull diameter and thicknesses.....	- 44 -
FIGURE 3.5: Righting/heeling moment.....	- 47 -
FIGURE 3.6: ISSC wave spectrum for the selected Japanese environmental conditions.....	- 48 -
FIGURE 3.7: RAO comparison of WAMIT and OpenFAST results without wind.....	- 50 -
FIGURE 3.8: Power spectra of motion response attributed to the storm condition.....	- 52 -
FIGURE 3.9: Local tower load distribution at wind speed 11 m/s under storm condition.....	- 53 -
FIGURE 3.10: Tower base force at wind speed 11 m/s under storm condition.....	- 54 -
FIGURE 4.1: Main dimensions and mass distribution of the scale model.....	- 63 -
FIGURE 4.2: Experiment setup and towing tank dimension.....	- 64 -
FIGURE 4.3: Prototype full-scale wave and model-scale wave.....	- 65 -
FIGURE 4.4: Operational wave's signal and spectrum.....	- 66 -
FIGURE 4.5: Storm wave's signal and spectrum.....	- 66 -
FIGURE 4.6: Centenary wave's signal and spectrum.....	- 66 -
FIGURE 4.7: Surge motion response obtained from free vibration test.....	- 67 -
FIGURE 4.8: Sway motion response obtained from free vibration test.....	- 68 -
FIGURE 4.9: Heave motion response obtained from free vibration test.....	- 68 -
FIGURE 4.10: Roll motion response obtained from free vibration test.....	- 68 -
FIGURE 4.11: Pitch motion response obtained from free vibration test.....	- 69 -

FIGURE 4.12: Yaw motion response obtained from free vibration test .....	- 69 -
FIGURE 4.13: Surge motion response obtained from operational wave .....	- 71 -
FIGURE 4.14: Sway motion response obtained from operational wave.....	- 71 -
FIGURE 4.15: Heave motion response obtained from operational wave .....	- 71 -
FIGURE 4.16: Roll motion response obtained from operational wave .....	- 72 -
FIGURE 4.17: Pitch motion response obtained from operational wave.....	- 72 -
FIGURE 4.18: Yaw motion response obtained from operational wave .....	- 72 -
FIGURE 4.19: Surge motion response obtained from storm wave.....	- 73 -
FIGURE 4.20: Sway motion response obtained from storm wave .....	- 73 -
FIGURE 4.21: Heave motion response obtained from storm wave.....	- 73 -
FIGURE 4.22: Roll motion response obtained from storm wave.....	- 74 -
FIGURE 4.23: Pitch motion response obtained from storm wave .....	- 74 -
FIGURE 4.24: Yaw motion response obtained from storm wave.....	- 74 -
FIGURE 4.25: Surge motion response obtained from centenary wave .....	- 75 -
FIGURE 4.26: Sway motion response obtained from centenary wave .....	- 75 -
FIGURE 4.27: Heave motion response obtained centenary wave .....	- 75 -
FIGURE 4.28: Roll motion response obtained centenary wave .....	- 76 -
FIGURE 4.29: Pitch motion response obtained centenary wave.....	- 76 -
FIGURE 4.30: Yaw motion response obtained centenary wave .....	- 76 -
FIGURE 4.31: RAOs of the operational wave .....	- 78 -
FIGURE 4.32: RAOs of the storm wave .....	- 78 -

FIGURE 4.33: RAOs of the centenary wave .....	- 79 -
FIGURE 4.34: RAOs comparison of the operational wave .....	- 79 -
FIGURE 4.35: RAOs comparison of the storm wave.....	- 80 -
FIGURE 4.36: RAOs comparison of the centenary wave.....	- 80 -
FIGURE 5.1: COM3 FE model mesh details.....	- 85 -
FIGURE 5.2: Hydrodynamic pressure excites on four faces of the hull surface using WAMIT.....	- 88 -
FIGURE 5.3: Hydrostatic and hydrodynamic pressure profile applied to FEM.....	- 88 -
FIGURE 5.4: Structural deformation and strain distribution (scale factor 1000).....	- 89 -
FIGURE 5.5: Free body diagram for the structural analysis.....	- 91 -
FIGURE 5.6: Concrete stress area and assumed stress distribution in a circular section.....	- 92 -
FIGURE 5.7: Stress and strain distribution of the section and the sectional design at equilibrium.....	- 94 -
FIGURE 5.8: M-N diagram of the section at five control points.....	- 95 -
FIGURE 5.9: Stress-strain localization of normal RC with a 0.1% reinforcement ratio.....	- 97 -
FIGURE 5.10: Stress-strain localization of normal RC with a 1% reinforcement ratio.....	- 98 -
FIGURE 5.11: Preliminary designed tower connection and strain localization after installation.....	- 98 -
FIGURE 5.12: Preliminary designed mooring connection and strain localization after installation.....	- 99 -
FIGURE 5.13: Preliminary designed prestressed concrete and strain localization after installation.....	- 100 -
FIGURE 5.14: Stress-strain relationship of a critical element of study cases CS3, CS4 and CS5.....	- 101 -
FIGURE 5.15: M- $\phi$ diagrams in vertical and horizontal directions of the five study cases.....	- 101 -
FIGURE 5.16: Structural displacements of study cases CS1 and CS3 (scale factor 300).....	- 102 -
FIGURE 5.17: Structural deformation and strain distribution (scale factor 1000).....	- 103 -

FIGURE 5.18: Precast segment hull concrete and final design reinforcement .....	- 104 -
FIGURE 6.1: 3D FE model of the connection zone and main dimension of the steel connection plate .	- 109 -
FIGURE 6.2: Drawing and FEM of Plate-Plate model.....	- 111 -
FIGURE 6.3: Drawing and FEM of Wire-Plate model .....	- 111 -
FIGURE 6.4: Drawing and FEM of Wire-Wire model.....	- 111 -
FIGURE 6.5: Drawing and FEM of Anchor Bolt model .....	- 112 -
FIGURE 6.6: Drawing and FEM of Anchor Bolt – Prestress model.....	- 112 -
FIGURE 6.7: Stress-strain distribution of Plate-Plate model.....	- 112 -
FIGURE 6.8: Stress-strain distribution of Wire-Plate model.....	- 113 -
FIGURE 6.9: Stress-strain distribution of Wire-Wire model .....	- 113 -
FIGURE 6.10: Stress-strain distribution of Anchor Bolt model .....	- 113 -
FIGURE 6.11: Stress-strain distribution of Anchor Bolt–Prestress model.....	- 113 -
FIGURE 6.12: Load amplitude of mooring tension versus time applied at fairlead connection .....	- 115 -
FIGURE 6.13: Location of the critical elements taken for fatigue life estimation .....	- 115 -
FIGURE 6.14: Stress amplitude and the number of cycles of concrete under tension .....	- 117 -
FIGURE 6.15: Tensile strain and the number of cycles of concrete under tension.....	- 117 -
FIGURE 6.16: S-N relation of concrete under tension according to the model code .....	- 119 -
FIGURE 6.17: Stress amplitude in the x-axis and number of cycles of concrete under compression.....	- 121 -
FIGURE 6.18: Stress amplitude in the y-axis and number of cycles of concrete under compression.....	- 122 -
FIGURE 6.19: Stress amplitude in the z-axis and number of cycles of concrete under compression .....	- 122 -
FIGURE 6.20: Compressive strain and the number of cycles of concrete under compression.....	- 123 -

FIGURE 6.21: S-N relation according to the model code ..... - 125 -

## LIST OF TABLES

TABLE 3.1: Key parameters of the IEA 10-MW RWT .....	- 43 -
TABLE 3.2: Mooring system properties and coordinates .....	- 45 -
TABLE 3.3: Trial geometry parameters.....	- 46 -
TABLE 3.4: Spar properties at equilibrium condition.....	- 47 -
TABLE 3.5: Irregular wave condition parameters.....	- 48 -
TABLE 3.6: Wind speed condition parameters .....	- 49 -
TABLE 3.7: Spectral analysis results using WAMIT .....	- 51 -
TABLE 3.8: Maximum force obtained from coupled dynamic analysis .....	- 55 -
TABLE 3.8: Maximum force obtained from coupled dynamic analysis (continue).....	- 56 -
TABLE 3.9: Motion statistics obtained using OpenFAST .....	- 57 -
TABLE 4.1: Scale factors using Froude Scaling.....	- 63 -
TABLE 4.2: Main dimensions of the floater .....	- 63 -
TABLE 4.3: Main properties of the floater .....	- 64 -
TABLE 4.4: Irregular wave in full-scaled analysis and the model test .....	- 65 -
TABLE 4.5: Natural periods obtained from the free vibration test.....	- 70 -
TABLE 4.6: The peak period obtained from the experiment with wave.....	- 70 -
TABLE 4.7: Comparison of natural periods between free vibration and wave tests .....	- 77 -
TABLE 5.1: Concrete and steel material properties .....	- 86 -
TABLE 5.2: Bond element properties.....	- 87 -



TABLE 5.3: Maximum force under the operational and storm conditions.....	- 91 -
TABLE 5.4: Sectional capacity and the assumption at each control point.....	- 95 -
TABLE 5.5: The five study cases of FE analysis.....	- 96 -
TABLE 6.1: Name and concept of the fairlead connection systems.....	- 110 -
TABLE 6.2: Fatigue life approximated by the reference point of tensile strain.....	- 118 -
TABLE 6.3: Fatigue life of the concrete under tensile force evaluated by the model code.....	- 118 -
TABLE 6.4: Fatigue life approximated by the reference point of compressive strain.....	- 124 -
TABLE 6.5: Fatigue life of the concrete under compression evaluated by the model code.....	- 124 -

## **ABSTRACT**

The Government of Japan implemented a new law to promote offshore wind in 2019. However, more than 90% of the 9,074 TWh of Japanese annual wind generation potential is located in the deep ocean, requiring the development of floating platform technology. This study, therefore, evaluates a conceptual design for a spar-type concrete floater to support a 10 MW offshore wind turbine using precast segment prestressed concrete. This conceptual design is developed based on the economic advantages of using normal-strength concrete. The preliminary dynamic analysis considers the environmental conditions of the Sea of Japan. The stability and motion analyses consider irregular waves under the operational, storm, and centenary conditions at the rated wind speed and cut-out wind speed of the wind turbine, as well as typhoon conditions. The geometry of the spar is determined using a coupled dynamic analysis to satisfy hydrostatic and hydrodynamic stabilities under wind turbine operation performed by WAMIT and OpenFAST. A cross-spectral analysis of the rigid body is then carried out to investigate the response motions of the proposed model under the input wind and wave conditions. The results show that the highest force occurred under the rated wind speed in storm conditions, serving as the dominant case for the investigated stress and strain distributions; although the typhoon conditions exhibit higher wind speeds, they correspond to a relatively small thrust force owing to the action of the wind turbine control system. The proposed concrete spar can be applied to support an RWT, and the structure is shown to avoid the structural resonance induced by wave excitation, as confirmed by a spectral analysis that indicated significant response motions that are much smaller than the input wave energies. To investigate and verify the hydrodynamic behavior of the proposed spar under wave action, the model test of the spar-scaled model 1:100 applied the Froude scale is carried out. The model is excited by three irregular wave conditions, operational, storm, and centenary, and the response motions are captured. The experiment results show good consistency with the full-scale analysis.

The nonlinear behavior of the concrete structure excited by the cyclic motions of the wind turbine tower and mooring tensions is numerically studied using the finite element code COM3. The maximum forces obtained from the dominant case of the hydrodynamic motion analyses under the wind turbine operation are applied to the FE model investigating stress-strain distribution. The preliminary steel-concrete connections are

then designed, and prestressing force is determined at the critical area indicated by the concrete ultimate tensile strain. The analytical results show the preliminary designed connections and prestressing force can prevent microcrack generation and propagation at the spar's tower base and fairlead locations. The designed tower connection can also prevent the bottom part of the steel tower from buckling failure and pulling out of concrete due to a large bending moment under the operation of the wind turbine. Investigation and design of the hull concrete have shown that although the hull concrete is under large hydrostatic and hydrodynamic pressure. However, the hull surface becomes under compression attributed to enough thickness of the hull concrete, indicated by tensile strain. Therefore, it is not necessary to design horizontal prestressing tendons to resist any tensile force induced by water pressure.

Finally, five types of fairlead connections are proposed in this research. The stress and strain distributions of each connection type are investigated. The analytical results show that all connection types satisfied the design objective to control crack development. Concrete under tension and compression at the fairlead connection zone significantly affects structural service life; therefore, fatigue analysis is carried out to estimate the fatigue life of the proposed structure. For concrete under tension, the fatigue life evaluated by FE analysis is longer than the model code's prediction. However, it is below the expected 1000 million cycles. Lower tensile fatigue life indicates the possibility of cracking at the fairlead zone, which can be improved in the following design phase. For concrete under compression, the compressive strain of four connection types doesn't reach the ultimate compressive strain, even if around 84 million cycles are applied to the model, except for the plate-plate model, which has a possibility of fatigue failure. The design of the plate-plate model can be improved in the next design phase.

On the deep discussion of experimental and analytical results, the findings in the dissertation successfully demonstrated an alternative concrete to steel floater based on assumptions to facilitate future mass production. In this research, a precast segment prestressed concrete spar floating platform capable of supporting a 10 MW floating offshore wind turbine is successfully performed.

# CHAPTER 1

## INTRODUCTION

### 1.1 Background and Motivation

Offshore wind farms have been developed as alternative sources for clean energy production. The average annual growth of offshore wind energy from 2010 to 2018 was 30% and continues to exhibit a great deal of unexploited potential globally [1]. In 2019, Japan implemented a law enabling offshore wind farms to be operated by local and foreign companies along its 29,750 km of coastal waters, which possess the potential to generate 1,600 GW of wind energy. Greater than 90% of the 9,074 TWh of Japan's annual wind energy generation potential is in the deep ocean and will require floating platform technology to utilize [1]. Overall, the energy generated by global floating offshore wind turbine (FOWT) systems grew from 7,663 MW in 2019 to 26,529 MW in 2020 and is expected to increase further as several projects, mainly in Asian markets, began their planning phases in 2020 [2].

Floating platforms that support offshore wind turbines in the deep ocean have been actively researched as near-shore offshore wind farms have become less competitive owing to limitations such as low harvesting wind speed, high construction cost, and negative environmental effects around coastal areas [3]. Thus far, three types of floating supporting structures have been studied in terms of stability [4]: gravity-based platforms, which include spar platforms; waterplane-based platforms, which include semi-submersible platforms; and external-constraint-based platforms, which include the tension-leg platform. The differences among these concepts are associated with their corresponding motions in heave, roll, and pitch; so-called vertical plane motions [5]. As a semi-submersible platform has a small water-plane area, it has relatively high natural periods in vertical modes; however, it requires flexible mooring and power take-off systems that can operate in extreme conditions. A tension-leg platform is very rigid in the vertical direction but flexible when subjected to horizontal motions because it relies upon tendon stiffness rather than water-plane stiffness. A gravity-based spar platform exhibits small heave motions owing to its deep draft, which is also advantageous for power take-off cables, umbilicals, and moorings [4]. Though this deep draft means that spar platforms cannot be used in

shallow waters (less than 100 m) [6], the simple cylindrical shape of the spar-based concept has been shown to be technically feasible and achieve cost reductions [7].

In 2009, Statoil Hywind launched the first 2.3 MW full-scale spar-buoy FOWT system installed close to Karmøy Island, Norway using steel materials [7]. Furthermore, in 2010, the Offshore Code Comparison Collaboration (OC3) for the International Energy Agency (IEA) Wind Task 23 Offshore Wind Technology and Deployment [8] selected the same "Hywind" spar buoy concept for a comparison of simulation codes. The spar buoy was modified to mount the NREL 5-MW wind turbine, a model known as the OC3-Hywind [9]. In 2012, a half-scale model of a hybrid spar mounted with a 100 kW wind turbine was installed at Goto Island, Nagasaki Prefecture, Japan, to conduct sea-state experiments [10]; in April 2016, a full-size 2 MW wind turbine was installed at the same location after the half-scale turbine was removed [11]. Both spar platforms were hybrid structures in which the upper and lower parts were composed of steel and prestressed concrete, respectively. Notably, these structures suffered severe typhoons during installation; however, they experienced no damage, and their structural stability was confirmed [10]. Simulation codes introduced by Utsunomiya et al. [12] and measurement data presented by Ishida et al. [10] were compared in [13], [14], and [15], which respectively investigated the dynamic response during severe typhoon events, various power generation conditions, and the effects of extreme environmental conditions. In 2014, the Fukushima Forward Project Phase 2 constructed the 7 MW "Advanced Spar" from steel. One of the general requirements of this spar was to accommodate the installation of 2–10 MW class wind turbines to achieve economies of scale [16]. The Advanced Spar concept comprised three hulls: the center of buoyancy (COB), middle, and lower hulls, all of which contain water ballast tanks.

Importantly, a marine structure is susceptible to corrosion that affects its long-term performance and fatigue life [17]. The decreasing fatigue life attributed to corrosion in the connection joints of the hull is a crucial concern when discussing steel platforms because offshore wind structures must withstand up to  $10^9$  (1,000 million) load cycles during their normal design service life of 20 to 25 years [18]. As a result, concrete materials have been increasingly used to develop FOWTs owing to their advantageous properties, such as high resistance to corrosion, low material requirements, and low construction costs [18]. The recent development of both bottom-fixed and floating concrete support structures demonstrates the likelihood of an

increase in the use of such structures in future offshore wind farms [18]. Most research to date has studied the use of reinforced or prestressed concrete in marine substructures [18], but the use of precast concrete segments prestressed by a post-tensioning system has not yet been widely investigated.

The ability of this approach to facilitate dockside pre-assembly followed by float-out to installation is expected to create a turning point that will considerably decrease the costs of installing future concrete supporting structures [18]. The precast concrete spar can be cast at any place before being transported to the fabrication site. The use of an unbonded post-tensioning system can then be employed to connect the precast segments instead of a pre-tensioning system, as the former method eliminates all grouting operations [19], addressing the economic aspects of this study. However, the tendon anchorage zone must be an object of focus to prevent strand corrosion owing to chloride ion infiltration [19]. The prestressing force applied to connect precast segments ensures the watertightness of the structure through the precompression induced by the tendons, which considerably increases the external force required to crack the concrete, resulting in a strong, tough, and stiff member [19]. The elimination of cracking (and limiting of crack widths) prevents the corrosion of reinforcing steel owing to chloride ion transport and diffusivity through the penetration of water into the concrete [20]. In addition, unlike steel fabrication, the production of precast concrete segments for use in post-tensioned spars does not require highly skilled labor; workers in the local communities of most any area can do this job.

## **1.2 Objectives / Target and Scope of the Study**

The main objective of this research is to develop a precast segment prestressed concrete spar floating platform capable of supporting a 10 MW floating offshore wind turbine. In order to achieve this main purpose, this research includes four following sub-objectives:

1. Investigation of the motion responses under wind turbine operation of the proposed precast segment prestressed concrete spar.
2. Investigation of the nonlinear behaviors of concrete under the maximum forces during wind turbine operation of the proposed precast segment prestressed concrete spar.

3. Investigation and design of hull concrete and steel-concrete connection systems of the proposed precast segment prestressed concrete spar.
4. Propose fairlead connection systems for the proposed precast segment prestressed concrete spar.

In this thesis, the numerical analysis is performed in two parts, and one experiment is carried out. First, the coupling model comprising the target spar, reference wind turbine (RWT), and mooring lines is studied in the coupled dynamic analysis. Here, the response motions of the proposed spar are investigated and thereby ensuring that the spar can be applied to support an RWT. Furthermore, the model test experiment is conducted for the verification of the spar's hydrodynamic model.

Second, the finite element (FE) analysis of the stresses in the concrete components is performed to observe the nonlinear behavior of concrete. The preliminary connection systems and prestressing force are then designed to prevent stress transfer to the spar floater and prevent crack generation at the critical area indicated by concrete ultimate tensile strain. Finally, five fairlead connection types are proposed in this thesis, and the fatigue life of each type is investigated. This thesis effectively demonstrated an alternative concrete to steel spar based on assumptions to facilitate future mass production.

### **1.3 Outline of the Dissertation**

This dissertation is composed of seven chapters which are briefly explained as follows.

**Chapter 1** introduces the background and motivation of this research. The objectives, target, and scope, as well as the research methodology, are briefly described.

**Chapter 2** reviews the basic knowledge of relevant theoretical backgrounds for analyzing and designing a proposed precast segment prestressed concrete spar.

**Chapter 3** illustrates the analytical simulation of coupled dynamic analysis of a floating wind turbine. Stability analysis and parametric study to define the first feasible geometry of the spar and cross-spectral analysis of the rigid body motion are also described. The geometry of the proposed precast segment prestressed concrete spar is successfully defined in this chapter.

**Chapter 4** is related to the model test, the experiment to verify the hydrodynamic model of the proposed precast segment prestressed concrete spar under wave action.

**Chapter 5** investigates concrete's nonlinear behavior of the proposed precast segment prestressed concrete spar under the maximum force of the wind turbine during operation through the analytical simulation of FE analysis. The preliminary steel-concrete connections and structural design are also performed in this chapter.

**Chapter 6** proposes five fairlead connection types to resist the large tensile forces transferring from mooring lines to the proposed precast segment prestressed concrete spar. The fatigue analysis and fatigue life estimation are illustrated in this chapter.

**Chapter 7** concludes the findings of this research and recommendation for further studies

### **Nomenclature in Chapter 1**

COB	center of buoyancy
FE	finite element
FOWT	floating offshore wind turbine
IEA	International energy agency
RWT	reference wind turbine

### **References in Chapter 1**

- [1] Insurer Consulting Group Asia, 2020, *Asia Offshore Wind Insurance Opportunities*, MARSH JLT SPECIALTY, Marsh Ltd.
- [2] Musial, W., Spitsen, P., Beiter, P., Duffy, P., Marquis, M., Cooperman, A., Hammond, R., and Shields, M., 2021, "Offshore Wind Market Report: 2021 Edition," p. 119.
- [3] Tracy, C. H., 2007, "Parametric Design of Floating Wind Turbines," M.S. thesis, Mechanical Engineering, MIT.
- [4] Hopstad, A. L. H., Argyriadis, K., Manjock, A., Goldsmith, J., and Ronold, K. O., 2018, "DNV GL Standard for Floating Wind Turbines," *International Conference on*



- Offshore Mechanics and Arctic Engineering*, American Society of Mechanical Engineers, p. V001T01A020.
- [5] Karimirad, M., 2011, "Stochastic Dynamic Response Analysis of Spar-Type Wind Turbines with Catenary or Taut Mooring Systems," Ph.D. thesis, Marine Technology, Norwegian University of Science and Technology.
- [6] Xue, W., 2016, "Design, Numerical Modelling and Analysis of a Spar Floater Supporting the DTU 10MW Wind Turbine," M.S. thesis, Marine Technology, Norwegian University of Science and Technology.
- [7] Yu Q., and Chen, X., 2012, *Floating Wind Turbines Final Report*, American Bureau of Shipping, Houston, Texas.
- [8] Jonkman, J., and Musial, W., 2010, "IEA Wind Task 23 Offshore Wind Technology and Deployment," National Renewable Energy Laboratory, Technical Report No. NREL/TP-5000-48191, p. 74.
- [9] Driscoll, F., Jonkman, J., Robertson, A., Simivas, S., Skaare, B., and Nielsen, F. G., 2016, "Validation of a FAST Model of the Statoil-Hywind Demo Floating Wind Turbine," *Energy Procedia*, 94, pp. 3–19.
- [10] Ishida, S., Kokubun, K., Nimura, T., Utsunomiya, T., Sato, I., and Yoshida, S., 2013, "At-Sea Experiment of a Hybrid SPAR Type Offshore Wind Turbine," *International Conference on Offshore Mechanics and Arctic Engineering*, Nantes, France, OMAE2013-10655, p. V008T09A035.
- [11] Tanaka, K., Sato, I., Utsunomiya, T., and Kakuya, H., 2020, "Validation of Dynamic Response of a 2-MW Hybrid-Spar Floating Wind Turbine during Typhoon Using Full-Scale Field Data," *Ocean Eng.*, 218, p. 108262.
- [12] Utsunomiya, T., Sato, I., Kobayashi, O., Shiraishi, T., and Harada, T., 2019, "Numerical Modeling and Analysis of a Hybrid-Spar Floating Wind Turbine," *J. Offshore Mech. Arct. Eng.*, 141(3).

- [13] Utsunomiya, T., Sato, I., Yoshida, S., Ookubo, H., and Ishida, S., 2013, "Dynamic Response Analysis of a Floating Offshore Wind Turbine During Severe Typhoon Event," *International Conference on Offshore Mechanics and Arctic Engineering*, Nantes, France, OMAE2013-55423, p. V008T09A032.
- [14] Utsunomiya, T., Yoshida, S., Kiyoki, S., Sato, I., and Ishida, S., 2014, "Dynamic Response of a Spar-Type Floating Wind Turbine at Power Generation," *International Conference on Offshore Mechanics and Arctic Engineering*, San Francisco, CA, USA, OMAE2014-45493, p. V007T05A027.
- [15] Utsunomiya, T., Yoshida, S., Ookubo, H., Sato, I., and Ishida, S., 2014, "Dynamic Analysis of a Floating Offshore Wind Turbine Under Extreme Environmental Conditions," *J. Offshore Mech. Arct. Eng.*, 136(2), p. 020904.
- [16] Yoshimoto, H., Awashima, Y., Kitakoji, Y., and Suzuki, H., 2013, "Development of Floating Offshore Substation and Wind Turbine for Fukushima FORWARD," *Proceedings of the International Symposium of Marine and Offshore Renewable Energy*, Tokyo, Japan, p. 28.
- [17] Bhattacharya, S., 2019, *Design of Foundations for Offshore Wind Turbines*, John Wiley & Sons Ltd, University of Surrey, UK.
- [18] Mathern, A., von der Haar, C., and Marx, S., 2021, "Concrete Support Structures for Offshore Wind Turbines: Current Status, Challenges, and Future Trends," *Energies*, 14(7), p. 1995.
- [19] Collins, M. P., and Mitchell, D., 1997, *Prestressed Concrete Structures*, Response Publications.
- [20] Maekawa, K., 2008, *Multi-Scale Modeling of Structural Concrete*, CRC Press.

## **CHAPTER 2**

### **THEORETICAL BACKGROUND**

#### **2.1 Introduction**

Studying of a prestressed concrete spar floating offshore wind turbine is a multidisciplinary area. It encompasses structural mechanics, hydrodynamics, aerodynamics, and a wind turbine control system. This must be analyzed as an integrative simulation before performing a structural design [1]. The coupled dynamic analysis of this thesis mainly focuses on the structure's motions, hydrostatic stability, and hydrodynamic and aerodynamic performance of a spar-type floating wind turbine. The concrete structural design is numerically investigated using concrete finite element analysis (FEA) considering the nonlinear behavior of a prestressed concrete spar under wind turbine operation. Then the life cycle assessment taken the critical part has been investigated considering the effect of the time dependency of the concrete structure under high cyclic fatigue. In the post-peak region where the damage has been developed, time-dependent becomes significant and affects the concrete structure's service life [2]. The relevant theoretical backgrounds for the analysis and design of a proposed prestress concrete spar are discussed in this chapter. First, an account of ocean waves, hydrostatics, and hydrodynamics are given. Later, the constitutive laws of the nonlinear behavior of structural concrete and the effect of time-dependency applied in the analysis have been discussed.

#### **2.2 Ocean Waves**

It should be reminded that the waves in the ocean environment are very complex and are normally described by their variance density spectrum [3]. The wave may be regular or irregular, unidirectional or omnidirectional, linear or nonlinear and etc. For a small offshore structure immersed in ocean waves, the understanding of separate flow or Morison's Equation is required. However, for the medium or large offshore structure, diffraction analysis is needed. Several wave theories describe the behavior of ocean waves and are summarized in [3]. The Airy waves or Linear wave theory, which is linearized the exact solution obtained from the potential theory, is applicable for waves that are not too steep, and the water depths are not too shallow. In other circumstances, high-order approximations or nonlinear wave theories are applied. The well-known

nonlinear wave theories, for example, Stokes's second-order, third-order, and fifth-order theories, Dean's stream function theory for steep waves, and cnoidal wave theory of Korteweg and de Vries [3],[4]. However, unlike natural waves, these waves are periodic, not harmonic.

### Linear wave theory and high-order wave theory

Begin with the simplest assumption that waves are two-dimensional, progressive, permanent gravity waves of period ( $T$ ), amplitude ( $H$ ), and length ( $L$ ) over a smooth horizontal bed, as shown in Figure 2.1 [3]. The wave was ideally created by the external impulse and the gravitational force; once it was created, it could sustain itself continually. This is fundamental to all other waves, from a simple sine wave to Stokes' fifth-order theory [3].

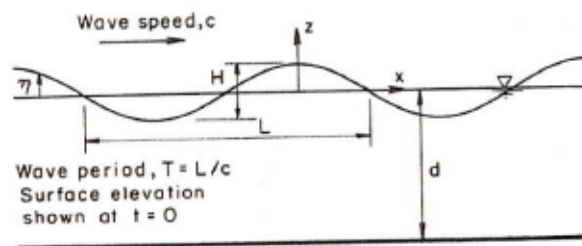


**FIGURE 2.1:** A progressive wave definition

The determination of wave speed ( $c$ ) and particle motion throughout the flow required a velocity potential that satisfies the Laplace equation.

$$\frac{\partial^2 \phi}{\partial x^2} + \frac{\partial^2 \phi}{\partial z^2} = 0 \quad (2-1)$$

The boundary condition at the seabed

$$\frac{\partial \phi}{\partial z} = 0 \text{ at } z = -d \quad (2-2)$$

The kinetic and dynamic boundary conditions at the free surface are respectively given by

$$\frac{\partial \eta}{\partial t} + \frac{\partial \phi}{\partial x} \frac{\partial \eta}{\partial x} - \frac{\partial \phi}{\partial z} = 0 \text{ at } z = \eta \quad (2-3)$$

and by

$$\frac{\partial \phi}{\partial t} + \frac{1}{2} \left[ \left( \frac{\partial \phi}{\partial x} \right)^2 + \left( \frac{\partial \phi}{\partial z} \right)^2 \right] + g\eta = f(t) \text{ at } z = \eta \quad (2-4)$$

In Equations 2-3 and 2-4 above, there are several nonlinear terms, and the free-surface conditions need to be applied at the initial unknown free surface. The exact solution of the above equation is indeed very complex. However, by linearization of the governing equation assuming that wave amplitude ( $H$ ) is much smaller than wavelength ( $L$ ) and water depth ( $d$ ), and ignoring the nonlinear terms, the boundary conditions are satisfied at  $z = 0$ .

The linear theory describes a regular sine wave in which the crest equals the trough. The free surface profile of a wave ( $\eta$ ) as a function of space ( $x$ ) and time ( $t$ ) is given by the following equation:

$$\eta(x, t) = \frac{H}{2} \sin(kx - \omega t) \quad (2-5)$$

Here,  $k$  is wave number, and  $\omega$  is wave frequency.

The linear theory is represented the sea states of irregular waves as a linear sum of  $i$  regular components through superposition [5]. The phase shift for each element is represented by  $\epsilon$

$$\eta(t) = \sum_i \eta_i \sin(\omega t - k_j x + \epsilon_i) \quad (2-6)$$

When the wave height to water depth ratio increases, the crest amplitude becomes larger in comparison to the trough. The wave becomes steep; thus, the behavior changes. In this circumstance, the high-order wave theories replace the linear theory. The selection of the theory relies upon the wave height and water dept. Airy waves have the advantage of being a linear solution, and spectral analysis can be applied. Higher-order waves

are recommended for mooring and riser analysis, drag-dominated structures, storm waves, and air gap analysis [4],[6],[7].

### 2.3 Frequency and Time Domain of the Sea States

The sea state needs to be represented as a power spectrum in the frequency domain calculations. The spectral amplitude per oscillation period characterizes the wave conditions. Several spectral models have been proposed; among them, ISSC, JONSWAP, and The Pierson-Moskowitz are well-known single-peaked spectra [4]. Many widely-used models for the spectrum of waves are of the form [8].

$$S(f) = \frac{A}{f^5} \exp\left(-\frac{B}{f^4}\right) \quad (2-7)$$

Where  $f$  is the frequency and  $A$ , and  $B$  are constants. ISSC spectrum is also referred to as this model; however, it differs from other types in determining  $A$  and  $B$  parameters.

The time domain calculation related to frequency domain spectral through inverse Fourier transform. The Cooley–Tukey algorithm is the most common Fast Fourier Transform (FFT) algorithm for this solution. In this thesis, NREL's Open FAST is utilized. The explanation of the FFT for the time domain solution can be found in [9].

### 2.4 Definitions of Rigid-Body Motions

Any marine structures in the relevant sea conditions, waves, current, and wind will be subject to the induced loads and motions. The definition of the motions of each structure is necessary because different marine structures are relevant to different types of motions [1]. Motions of floating structures can be divided into wave-frequency motion, high-frequency motion, slow-drift, and mean drift motion [10]. The wave-frequency motion is mainly linearly excited motion in the wave-frequency range of the significant wave energy. This motion is significant for a spar floating platform, which will be the focus of this research. High-frequency motion is significant for TLPs platforms. In waves and currents, slow-drift motion and mean drift

motion are caused by nonlinear wave effects; and also, wind-induced drift and mean motion. Slow-drift motion arises from resonance oscillations; for a moored structure, it occurs in the surge, sway, and yaw [10].

Surge, sway, and heave are the oscillatory rigid-body translatory motions, in which surge is the longitudinal motion and heave is the vertical motion. The oscillatory angular motions are called the roll, pitch, and yaw, in which roll is the angular motion about the longitudinal axis, and yaw is about the vertical axis. Heave is an important response motion for many marine structures, and the restoring force of the structure may cause heave resonance that must be avoided. A deep draft spar exhibits a small heave motion because the deep draft is related to the waterplane area; therefore, it has a low possibility of heave resonance. Figure 2.2 shows an example of the definition of rigid-body motion modes of a deep concrete floater [10].

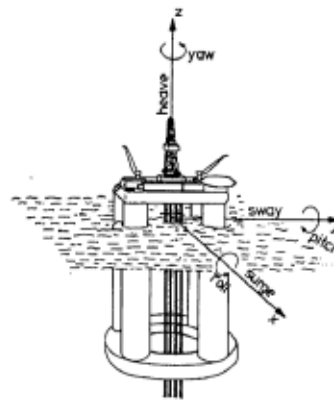


**FIGURE 2.2:** Definition of the rigid-body motion modes for a deep draft concrete floater

## 2.5 Floater Hydrostatics and Upright Stability

Hydrostatic pressure  $p$  is the pressure distribution in a fluid on a submerged body. It depends only on the depth  $z$  with no shearing stress [11]. The hydrostatic pressure can be defined as

$$\frac{dp}{dz} = -\rho g \quad (2-8)$$

Where  $g$  is gravitational acceleration 9.81 m/s, and  $\rho$  is a fluid density.

Hydrostatic restoring force provides stability for the floating structure attributed to the structure's overall stiffness. Therefore, it is relevant to the platform motion and the natural frequency. The buoyancy force acts on the centroid of the displaced fluid of the floating structure. The displaced volume of the structure with  $n$  parts can be defined as

$$\nabla = \sum_{l=1}^n \nabla_l \quad (2-9)$$

The centroid of the volumes in  $x$ ,  $y$ , and  $z$  axes computed with reference to the keel point ( $K$ ) are

$$(x_b, y_b, z_b) = \left( \frac{\sum_{l=1}^n \nabla_l x_l}{\nabla}, \frac{\sum_{l=1}^n \nabla_l y_l}{\nabla}, \frac{\sum_{l=1}^n \nabla_l z_l}{\nabla} \right) \quad (2-10)$$

In the static equilibrium, the structural weight and the buoyancy force act on the center of gravity at the same vertical line in the opposite direction. When the structure tilts or rotates, the submerged geometry changes, and the center of buoyancy is shifted. Here, the metacenter ( $M$ ) is the point where the new action line of buoyancy force intersects with the previous one, as shown in Figures 2.3 and 2.4 [12]. The distance of this point to the center of gravity, so-called  $GM$  or metacentric height, expresses the initial stability of the structure. If the  $GM$  is positive, the floating structure is stable in that position. However, if it is negative, the structure will rotate until it achieves the static equilibrium point [4],[12].

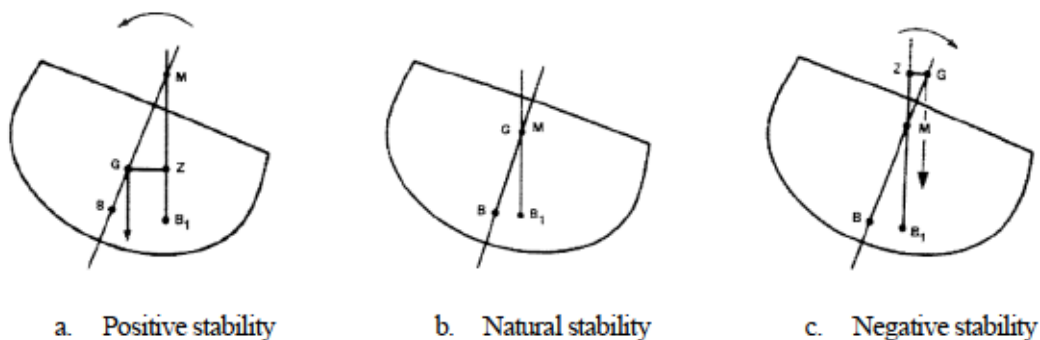


**FIGURE 2.3:** Stability conditions



The metacentric height, referenced from keel  $K$ , is defined as

$$\overline{GM} = \overline{KB} + \overline{BM} - \overline{KG} \quad (2-11)$$

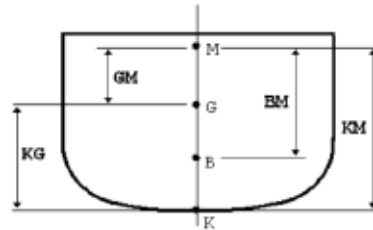


**FIGURE 2.4:** Linear measurements in stability

Here,  $KG$  is the height of the floater's center of gravity above the keel.  $KM$  represents the height of the metacenter above the keel. The metacentric radius, the radius of the circle for the movements of "B" at small angles of the heel [12], denotes by  $BM$  defined as;

$$BM = \frac{I_{ij}^w}{\nabla} \quad (2-12)$$

In Equation 2-12, the term  $I_{ij}^w$  means the moment of inertia of the waterplane area. When the  $x$  and  $y$ -axes are defined as the longitudinal and transverse axes, respectively, If the subscript  $ij$  is replaced with  $xx$ , it represents the roll motion, and  $yy$  represents the pitch motion.

The moment of inertia of area and moment of inertia of waterplane area of the closed polygon; or known as vertices  $V(x_i, y_i)$  can be defined as shown in Figures 2.5 to 2.6 [13] and Equations 2.13 to 2.15, respectively.

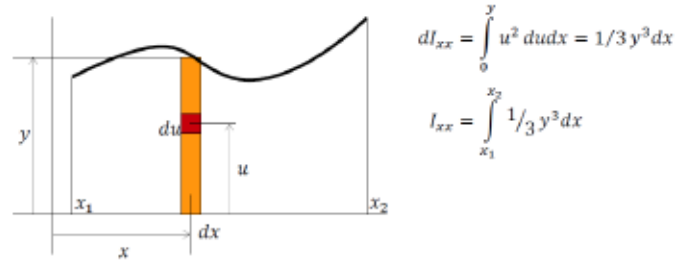


**FIGURE 2.5:** Second moment of area: the moment of inertia of area

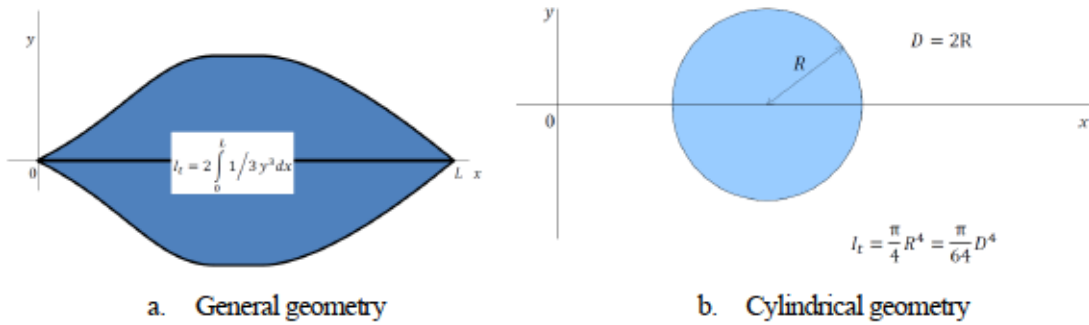


**FIGURE 2.6:** Moment of inertia of water plane area

$$I_{xx} = \frac{1}{12} \sum_{i=1}^n (y_i^2 + y_i y_{i1} + y_{i+1}^2) (x_i y_{i1} - x_{i+1} y_{i1}) \quad (2-13)$$

$$I_{yy} = \frac{1}{12} \sum_{i=1}^n (x_i^2 + x_i x_{i1} + x_{i+1}^2) (x_i y_{i1} - x_{i+1} y_{i1}) \quad (2-14)$$

$$I_{xy} = \frac{1}{12} \sum_{i=1}^n (x_i^2 + x_i x_{i1} + x_{i+1}^2 + y_i^2 + y_i y_{i1} + y_{i+1}^2) (x_i y_{i1+1} - x_{i+1} y_{i1}) \quad (2-15)$$

The hydrostatic forces affect the motion of the free-float body through hydrostatic stiffness or hydrostatic restoring coefficients  $C_{kj}$ , which depended only on the waterplane geometry [1]. For a symmetrical waterplane body such as a spar with diameter  $D$ , the hydrostatic restoring coefficients  $C_{35}$  and  $C_{53}$  is zero, and the moment of inertia of water plane area about all axis is  $I_t = \frac{\pi D^4}{64}$ . The nonzero terms in the hydrodynamic stiffness matrix for a body with a symmetrical  $x - z$  plane assuming small motion, can be defined from the center of buoyancy ( $Z_B$ ) and the center of gravity ( $Z_G$ ) as [1],[10].

$$C_{33} = \rho g A_{wp} \quad (2-16)$$

$$C_{35} = C_{53} = -\rho g \iint_{A_{wp}} x ds \quad (2-17)$$

$$C_{44} = \rho g \nabla (Z_B - Z_G) + \rho g \iint_{A_{wp}} y^2 ds = \rho g \nabla \overline{GM_T} \quad (2-18)$$

$$C_{55} = \rho g \nabla (Z_B - Z_G) + \rho g \iint_{A_{wp}} x^2 ds = \rho g \nabla \overline{GM_L} \quad (2-19)$$

Here  $A_{wp}$  is the waterplane area for a cylindrical geometry  $A_{wp} = \frac{\pi D^2}{4}$ , and  $\nabla$  is the water's displaced volume.  $\overline{GM_T}$  is the transverse metacentric height and  $\overline{GM_L}$  is the longitudinal metacentric height.

Then the hydrostatic stiffness or hydrostatic restoring coefficients  $C_{kj}$  is defined as

$$C_{kj} = \begin{bmatrix} 0 & 0 & 0 & 0 & 0 & 0 \\ 0 & 0 & 0 & 0 & 0 & 0 \\ 0 & 0 & C_{33} & 0 & C_{35} & 0 \\ 0 & 0 & 0 & C_{44} & 0 & 0 \\ 0 & 0 & C_{53} & 0 & C_{55} & 0 \\ 0 & 0 & 0 & 0 & 0 & 0 \end{bmatrix} \quad (2-20)$$

For a free float body assuming small displacement around the resting position, the linear restoring forces and restoring moment can be defined by [10].

$$F_k = -C_{kj} \eta_j \quad (2-21)$$

Where  $F_k$  is the vector of restoring forces and  $\eta_j$  is the vector of displacements around the equilibrium position.

The stability of a gravity-based spar platform relies on buoyancy force and ballast. Therefore, hydrostatic restoration and upright stability are critical in the dynamic motion of the structure. In other types, such as tension leg platform, which is very rigid in the vertical direction but flexible when subjected to horizontal motions, the stiffness relies on the tendon or mooring lines rather than waterplane stiffness like a spar.

## 2.6 Floater Hydrodynamics

In this research, the calculation is based on the numerical code WAMIT [14], which is a radiation/diffraction program developed for the analysis of the interaction of surface waves with offshore structures. Most details are taken from [1], [4], [10], and [14].

### 2.6.1 Potential Flow Theory

Potential flow theory can be accurate in predicting a large body's hydrodynamics forces that associate with the nonzero relative velocity of the surrounding fluid and is not related to viscous effects [15]. In other words, potential flow theory considers particularly boundary conditions of the natural flow fluid. It solves the hydrodynamic problem with a set of simplifications. Even though the high-order solution does exist, however linearization solution can reduce the complexity and provide preliminary structural behavior during the conceptual design process. Here, specific conditions are applied to the water and kinematics to reduce the complexity. Water is defined as incompressible and homogeneous fluid; it is inviscid and has no vorticity [4]. These conditions allow the formation of the following equations.

If the water is incompressible and homogeneous, we can have the equation of continuity as

$$\frac{\partial u}{\partial x} + \frac{\partial v}{\partial y} + \frac{\partial w}{\partial z} = 0 \quad (2-22)$$

Where  $u$ ,  $v$  and  $w$  are the fluid velocity vectors in  $x$ ,  $y$ , and  $z$  axes.

If the fluid is inviscid and has no vorticity, then it is irrotational and remains constant. The fluid velocity vector may be expressed by a scalar function, the velocity potential ( $\phi$ ). Thus, the velocity vector ( $\vec{V}$ ) can be defined as the gradient ( $\nabla$ ) of the velocity potential. Under this hypothesis, the hydrodynamic problem is generated in terms of the potential flow theory.

$$\vec{V} = \nabla\phi \quad (2-23)$$

The fluid velocity potential reduces the continuity equation to the Laplace Equation.

$$\nabla^2 \phi(\vec{x}_0, t) = \frac{\partial^2 \phi}{\partial x^2} + \frac{\partial^2 \phi}{\partial y^2} + \frac{\partial^2 \phi}{\partial z^2} = 0 \quad (2-24)$$

If boundary conditions of the floating body surface, free surface, and the sea bottom surface (deep water or infinite distance from the body) are known. Together with the dynamic free surface and kinematic boundary conditions are defined, the solution of the Laplace Equation can be obtained. In practice, the problem is solved by expanding  $\phi$  as a series of functions with increasing order [15].

$$\phi = \phi_1 \epsilon + \phi_2 \epsilon^2 + \dots \quad (2-25)$$

Generally, loads related with  $\phi_1$  (first-order wave load) and  $\phi_2$  (second-order wave load) are the most significant problems of large floating bodies. The first-order problem is divided into the radiation and diffraction problems which are accurate in evaluating the hydrodynamics forces of a large body. The second-order problem results in loads with different frequency ( $\omega_i - \omega_j$ ) and sum frequency ( $\omega_i + \omega_j$ ) components. The difference-frequency wave loads excite low-frequency motions in the surge, sway, and yaw for typical floating structures and are important in the analysis of mooring systems [15].

In the linear solution, the fluid velocity potential  $\phi(\vec{x}_0, t)$  in Equation 2.24 is considered to compose of two components; steady term or steady flow ( $\bar{\phi}$ ), and unsteady term or oscillatory flow ( $\tilde{\phi}$ ) which is expressed by [4].

$$\phi(\vec{x}_0, t) = \phi(x + Ut, x, z, t) = \bar{\phi}(\vec{x}) + \tilde{\phi}(\vec{x}, t) \quad (2-26)$$

The unsteady term  $\tilde{\phi}(\vec{x}, t)$  is composed of incident waves (incoming waves  $\phi^I$ ), diffracted waves ( $\phi^D$ ), and radiated waves ( $\phi^R$ ).

$$\tilde{\phi} = \phi^I + \phi^D + \phi^R \quad (2-27)$$

Here, the radiation potential is the summary of the six oscillatory motions.

$$\phi^R = \sum_{j=1}^6 \phi_j^R, j = [1: 6] \quad (2-28)$$

Finally, if the velocity potential is known, the fluid pressure can be determined by applying the Bernoulli Equation shown in Equation 2-29. Then the exciting force  $F^E$ , radiation force  $F^R$ , and hydrostatic force  $F^H$ , that acts on the structure can be obtained [4].

$$p(\vec{x}_0, t) = -\rho \left( \frac{\partial \phi}{\partial t} + \frac{1}{2} |\nabla \phi|^2 + g z_0 \right) \quad (2-29)$$

Here,  $p(\vec{x}_0, t)$  is the fluid pressure,  $\rho$  denoted as the fluid-specific mass, and  $g$  is the gravitational acceleration. The hydrodynamic forces acting on the hull is the integration of the fluid pressure over the wetted surface [4].

### 2.6.2 Wave loads on a Structure

Hydrodynamics forces are the integration of the water pressure field over the wetted surface of a rigid body using the appropriate approach. It is dependent on the ratio of wave amplitude and size of the structure compared to the wavelength, as shown in Figure 2.7 [10].

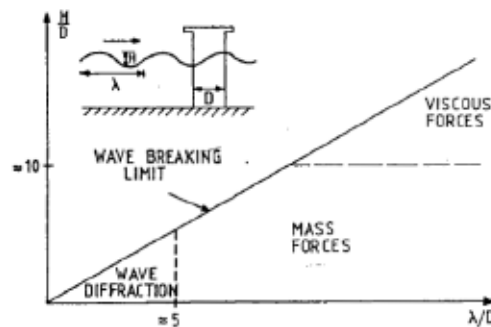


**FIGURE 2.7:** Classification of wave forces

In Morison Equation, it is assumed that the structure is small enough so that it does not disturb the pressure field around it. However, for the large structure, the existent body will change the pressure field.

Pressure effects on the floating structures may be divided into

1. Incident wave potential, the so-called inertia or Froude-Krylov forces.
2. Radiation component due to relative velocity and acceleration between water and structure. It assumes that the body is forced to oscillate in calm waters. As a reaction, the fluid exerts forces and moments on the body, with their related hydrodynamic added mass and damping forces, as shown in Equation 2-30.
3. Diffraction component caused by diffracted waves on the body surface. Here, the structure is assumed to be fixed and subjected to incident waves. For large-volume bodies, when the wave  $\lambda$  is much longer compared with the body length  $D$  (Figure 2.7), then the body is assumed not to disturb the wave field around them; the diffraction effects can be negligible.

Radiation force is defined as

$$F_{R,i}(\omega) = -a_{ij}(\omega)\ddot{x}_j - b_{ij}(\omega)\dot{x}_j \quad (2-30)$$

where  $a_{ij}$  and  $b_{ij}$  are the added mass and radiation-damping coefficients, respectively.

### 2.6.3 Morison's Equation

In fluid dynamics, Morison's Equation serves to calculate the load on the structure by presenting them as the sum of two force components: an inertia force and a drag force.

Morison's equation for the fixed body in an oscillatory flow expresses by

$$F = \underbrace{\rho C_m V \dot{u}}_{\text{Froude-Krylov (Inertia)}} + \underbrace{\frac{1}{2} \rho C_d A u |u|}_{\text{Viscous (Drag)}} \quad (2-31)$$

In Equation 2-31, the first term represents the inertia or Froude-Krylov force. The second term is the drag or viscous force. Here,  $\dot{u} = \frac{du}{dt}$  is the flow acceleration which is the time derivative of the flow velocity  $u(t)$ , and  $C_d$  and  $C_m$  are the drag and mass coefficients, respectively. The mass coefficient  $C_m = 1 + C_a$ , and  $C_a$  is the added mass coefficient. These coefficients should be calibrated based on experiments, but reference values for typical cross-sections are provided in DNV-RP-C205 [16].

For a circular cylinder of diameter  $D$  in oscillatory flow, the reference area per unit length  $A = D$ , and the volume per unit length  $V = \frac{\pi D^2}{4}$  the formula is obtained as follows [17].

$$F = \rho C_m \frac{\pi D^2}{4} \dot{u} + \frac{1}{2} \rho C_d D u |u| \quad (2-32)$$

Morison's equation for the moving body in an oscillatory flow expresses by

$$F = \underbrace{\rho C_m V \dot{u}}_{\text{Froude-Krylov}} + \underbrace{\frac{1}{2} \rho C_d A (u - v) |u - v|}_{\text{Viscous (Drag)}} + \underbrace{\rho C_a V (\dot{u} - \dot{v})}_{\text{Hydrodynamics Mass (Added Mass)}} \quad (2-33)$$

In Morison's Equation, the structure is assumed to be much smaller than the wavelength; hence, it will not disturb the fluid flow around them. Therefore, the fluid flow acceleration is uniform; the diffraction effects can be ignored (Figure 2.7).

However, for a large structure, if the diameter of the body is not small compared to the wavelength, diffraction effects must be taken into account. Under this circumstance, the fluid flow becomes complicated and attached to the structure. The flow decomposes to wave scattering, radiation, and diffraction components as given in Equation 2-27. In this work, the numerical code WAMIT [14] is used for calculating wave loads on the structure. It needs the 3D description of underwater geometry up to the mean water level. The geometry is discretized to the panel, which is described by coordinates. Once the velocity potential is known, the pressure



at the center of each panel is obtained from the linear term of the Bernoulli equation. Forces and moments of the six degrees of freedom are the pressure field integrated over the structure's surface [4].

## **2.7 Constitutive Modeling and Time-Dependent Mechanics of Structural Concrete**

In this research, the nonlinear behavior of concrete calculation is based on finite element code COM3 [18], and most details are taken from [2],[19]. Unlike steel material, concrete is heterogeneous (non-homogeneous), highly pressure sensitive, cohesive-frictional material. The compressive stress transfer is accomplished by a frictional force attributed to cement paste, aggregates, and reinforcing bars [2]. The stress-strain response of concrete depends upon the rate of loading and the time history of loading. If the stress is kept constant for some period of time, the strain increase; this phenomenon is known as creep. If the strain is kept constant for some length of time, the stress will decrease; this phenomenon is known as relaxation [20]. When stress levels in concrete exceed 70% of uniaxial compressive strength, damage may occur in the form of creep rupture or other defects. One key is contributed to the nonlinearity of softened compression. Here, near-peak and post-peak regions are concerned in order to define the remaining capacity of the structural concrete from the structural safety point of view. There are two facts about structural concrete: first, confinement is very effective for improving post-peak response, and second, time dependency becomes significant in the post-peak region. Time-dependent constitutive models of structural concrete before and after cracks are discussing in this session.

### **2.7.1 Elasto-Plastic and Fracturing Model in Compression**

Time dependency becomes dominant when the stress levels in concrete exceed 70% of uniaxial compressive strength with regard to the nonlinearity of compression softening after the post-peak region. At this stage, damage may occur in the form of creep rupture within a shorter stress period. The loading rate accelerates the damage beyond the peak, shortening the period to collapse. The post-peak analysis is concerned with structural safety, and the rate effect is becoming significant in estimating the structure's capacity until it completely collapses [2]. To deal with this problem, the elasto-plastic fracture model is proposed by Maekawa et al.[19]. One system of uncracked concrete is composed of infinitesimal elasto-

plastic components in parallel. The elasticity of concrete is attributed to the elastic deformation of coarse aggregate and cement paste, which is a reversible reaction. It is modeled by Hook's law spring; each spring is assumed to have different stiffness. The plasticity of concrete is an irreversible reaction represented by sliders, contributed to the crushing of air bubbles, slip between coarse aggregate and mortar, water movement in micropores of cement paste, etc. Concrete damage is assumed to occur when the elastic springs break. Here, concrete strain  $\varepsilon$  (the summation of plastic strain  $\varepsilon_p$  and elastic strain  $\varepsilon_e$ ) is used as the indicator. Under loading conditions, if no elastic springs are damaged, we would have the perfect elasticity. However, if micro-cracks and other defects occurred, we could say some elastic springs were broken. The total stress is taken as the remaining internal components presented by the fracture parameter  $K_0$ . In other words, the fracture parameter means the ratio of survived elastic springs. Figure 2.8 presents the elasto-plastic fracture model (EPF) of uncracked concrete under compression [19]. This basic concept has extended to time dependency in the form of the plastic rate function and damage rate function shown in Section 2.9.

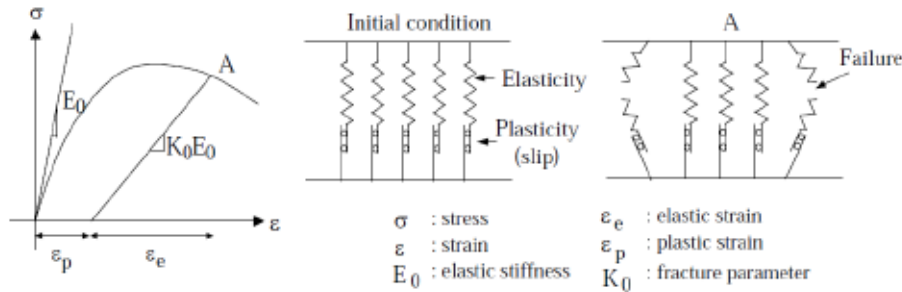


**FIGURE 2.8:** Concept of elasto-plastic fracture model of uncracked concrete

After the concrete crack, due to the past loading history, the concrete stress becomes complicated because of stress transfer along the crack and bond stress interfacing between concrete and reinforcing bars. The elasto-plastic fracture model can be used to express compressive stress parallel to the crack direction of the crack concrete, under loading, unloading, and reloading conditions, or the energy absorption during the cyclic load path. Compression field theory found that tensile strain causes damage that worsens strength and stiffness [19]; hence, under cyclic load, it has to be appropriately taken into account; otherwise, capacity can be overestimated. Figure 2.9 presents the uniaxial compression model parallel to the crack [19].

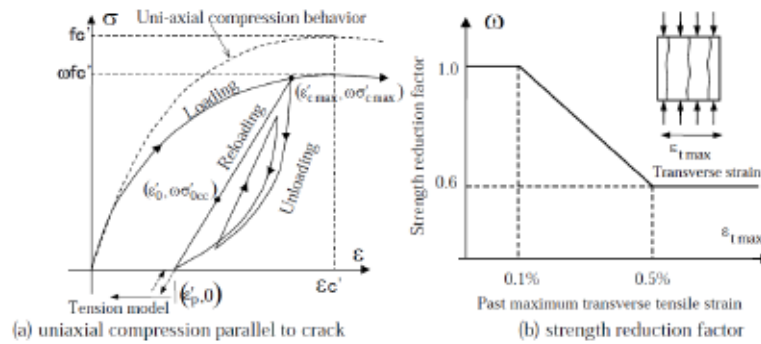


**FIGURE 2.9:** Uniaxial compression model parallel to crack

### 2.7.2 Model for Tension and Bond

After concrete crack attributed to the past loading history, the tensile strength of concrete decreases because of the continuum fracture under compression. Reinforced concrete (RC) can still support the part under tension even after cracking because of the bond interface between the concrete and reinforcing bar. This phenomenon is known as the tension stiffening effect, which increases the overall stiffness of RC in tension. Figure 2.10 presents the space-averaged tension stiffening model [19]. Here the curve control parameter  $c$  (the stiffening parameter), has been obtained from past experiments. For deformed bar  $c = 0.4$  and  $0.2$  for welded wire mesh.

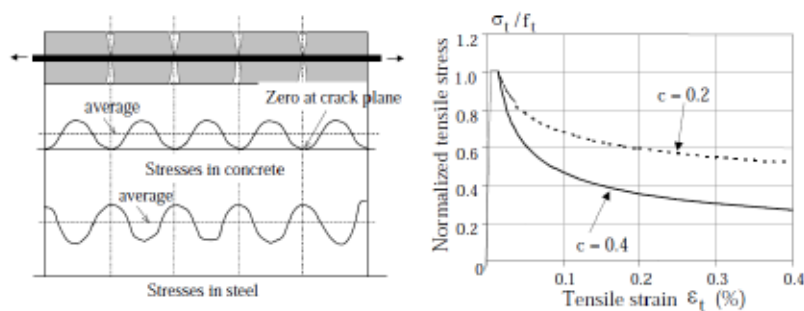


**FIGURE 2.10:** Stress distribution and space-averaged tension stiffening model

However, for the plain concrete, it was found that the strain softens after cracking due to the localization of single crack and tensile stress release [19]. This phenomenon is known as the tension softening effect, in

which the fracture energy is dependent on the dimension of the specimen. Figure 2.11 presents the tension softening model for plain concrete [19].

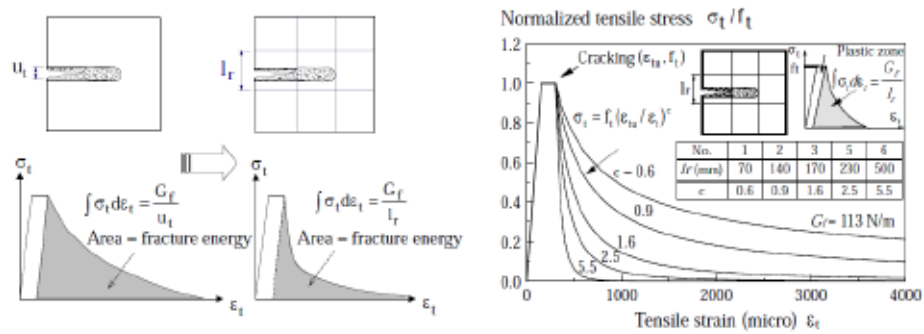


**FIGURE 2.11:** Tension softening curves adjusted based on finite element length

After cracking, under the cyclic reversal load, the crack will open when the load is given (loading), but when the load is removed (unloading), the crack opening close, and the crack surface of the opposite side re-contact again. Even though the opening does not perfectly close or recover, however, some amount of compressive stress can be transferred across the crack attributed to fragments of concrete, the roughness of coarse aggregate, shear slip, and bond action. Figure 2.12 presents the re-contact model [19] which the re-contact stress will be added to the compression or tension model to form the total normal stress transfer of cracked concrete [19].

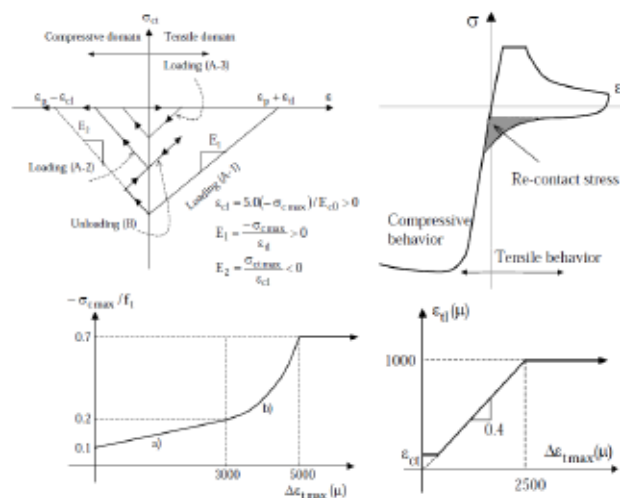


**FIGURE 2.12:** Re-contact model

In RC, the bond stress transfers from deformed bar to concrete derived from the bar lugs pushing against surrounding concrete. There are two functions in the bond between concrete and steel: interface friction attributed to fine aggregate and mechanical lock due to aggregate and bar lugs. Figure 2.13 presents the mechanism of RC bond and the formation of a tensile crack [19].

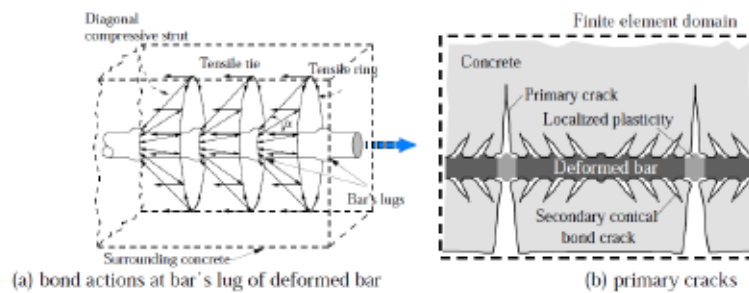


**FIGURE 2.13:** Mechanism of bond and formation of tensile crack

In FE analysis, the mechanical lock is rarely possible to model since it needs to model a very fine finite element mesh of each lug. On the other hand, the zero-thickness bond link element is placed between steel and concrete element to deal with interface bond/micro behavior [19]. Here, the bond-slip-strain model is presented to consider the magnitude of damage in concrete. Figure 2.14 presents the relation between bond stress, slip, and strain [19]. The bond stress is affected by the compressive strength of concrete and the strain distribution of the rebar, which is related to the rebar diameter. The three parameters of bond, slip, and strain have a mutual relationship; therefore, concrete strain can be expressed in terms of slip and bond stress.

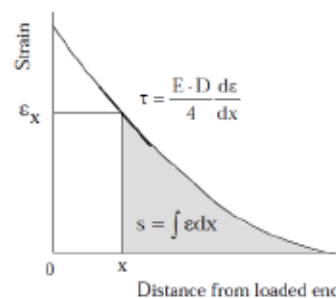


**FIGURE 2.14:** Unique relation between bond stress, slip, and strain

Under the reversed loading, the reduction in the tension stiffness of RC element after cracking can be attributed to bond creep and cracking in the new section. Time-dependent plasticity and fracturing are the keys of accumulated damage under tension. Similar to the compression model, the tensile fracture parameter  $K_T$ , which stands for path-dependent instantaneous fracturing, time-dependent tension creep, and accumulated damage, is considered to the constitutive model shown in Section 2.9.

### 2.7.3 Contact Density Model (Shear Transfer Model)

Stress transfer across crack contact may affect the deformation behavior and overall capacity of the RC and the structure. For normal concrete, the shape of the crack surface is rough regarding the crack path going along the coarse aggregate, which is different from the lightweight of high-strength concrete in that the crack path cuts through the aggregate. In normal concrete, when the opening crack is subjected to shear displacement or shear slip, the surfaces on the opposite side move relatively to each other and touch in some locations. Here, it transmits shear and normal compressive stress, which is depended on concrete strength and aggregate size. The contact density function, using a simple trigonometric function, is proposed based on the past experiments show in Figure 2.15 [19].

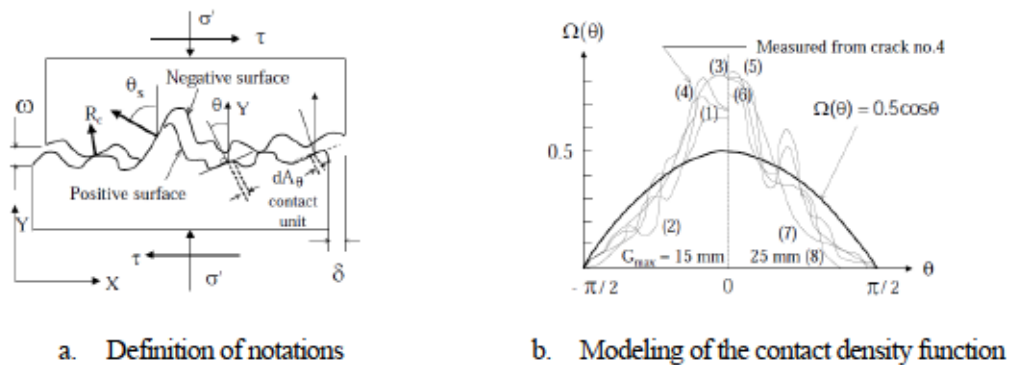


**FIGURE 2.15:** Contact density of each direction

For a crack width, the contact area is larger for a rough surface crack; here, the effective contact area denoted by  $K$  is introduced to present the effect of crack width attributed to the maximum size of coarse

aggregate. Finally, the contact stress transfer at any unloading-reloading paths can be derived by numerical integration by transforming the crack displacement in the global coordinate to the local coordinate since the constitutive model is defined with respect to the local coordinate. However, in FE analysis, the vigorous integral formation is not convenient to directly implement in the finite element program; the simpler shear constitutive law, which directly computes shear stress from shear strain, is used instead; details can be found in [19]. The unloading and reloading curve of the simplified shear model shows in Figure 2.16 [19].

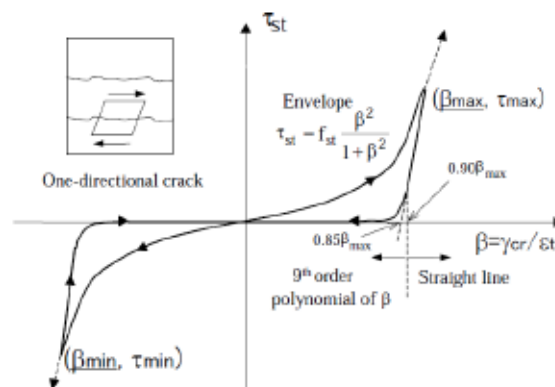


**FIGURE 2.16:** Shear transfer model for one-directional crack

## 2.8 Constitutive Model of Concrete with Multi-Directional Cracks

At present, an advanced concrete constitutive model that can consider cracks in up to 6 directions has been developed and implemented in Finite Element Code COM3 [18], which is adopted in this research. The constitutive models were developed for the specific path-dependent nonlinearity of reinforced concrete, mainly attributed to cracking, reinforcement plasticity, and bond interaction between concrete and reinforcement [19]. Before the concrete crack, the 3D elasto-plastic fracture model based on continuum mechanics is adopted for the uncracked concrete. After the concrete crack, the stress mechanism becomes anisotropic in the crack direction. The constitutive laws of cracked concrete are presumed to comprise stress transfer parallel to the crack axis, stress transfer normal to the crack axis, and shear transfer along the crack, which can be derived from a strain developed in the RC element. Figure 2.17 shows the spatially averaged stress of plain or reinforced concrete elements according to the cracking state [19].

In order to deal with the multi-directional crack condition, the active crack has been proposed. The assumption is that, in multiple directions, when more than one crack occurs and the cracks intersect with neighboring cracks, the most nonlinearity will concentrate in the larger crack because stress transfer across the crack is depended on crack width. Here, the first active crack is selected based on tensile strain (as the logic that cracks occur when tensile in concrete is greater than tensile capacity), and the crack coordinate is applied, cracks in other directions can be ignored [21],[22],[23],[24]. Under loading condition, the active crack and crack plane is re-judged based on the normal stress computed from the spatially averaged RC constitutive model, with quasi-orthogonal bi-directional cracking. This method has been extended to allow for more cracks in 3D stress fields. Figure 2.18 show the switch coordinate with the active crack concept [19]. Figure 2.19 shows the crack concrete stress based on active crack [19],[21].

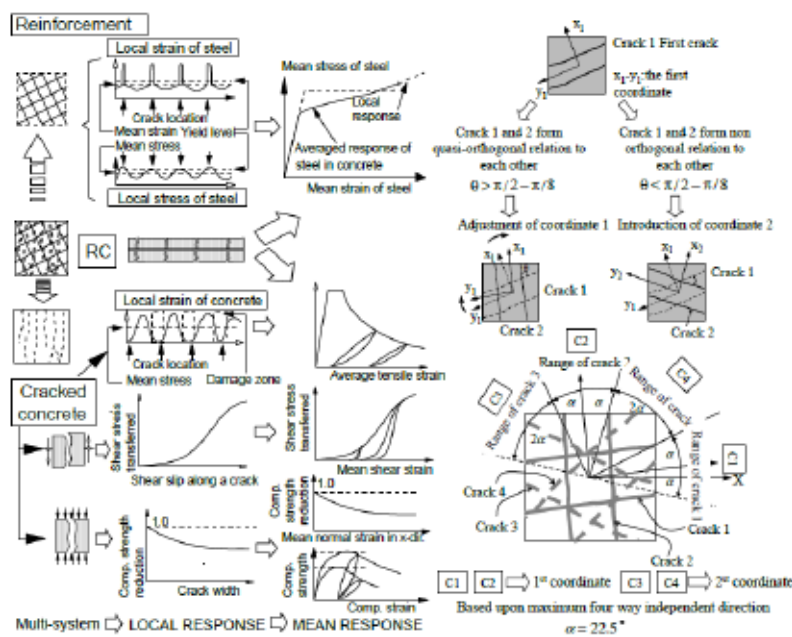


**FIGURE 2.17:** Overview of the advanced RC model and multidirectional crack



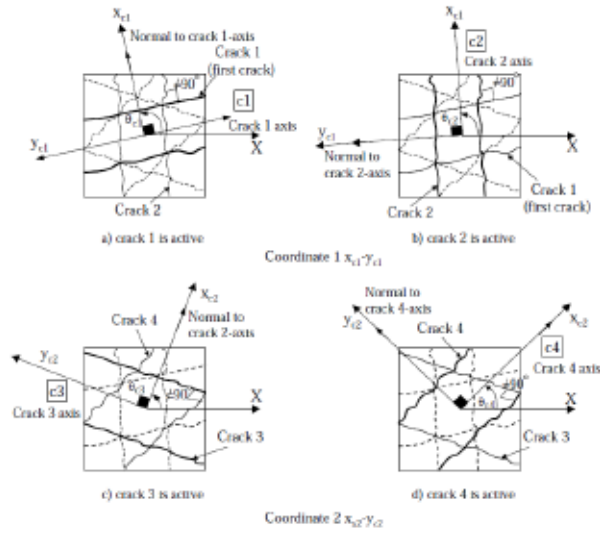


FIGURE 2.18: Switch of coordinate with the active crack

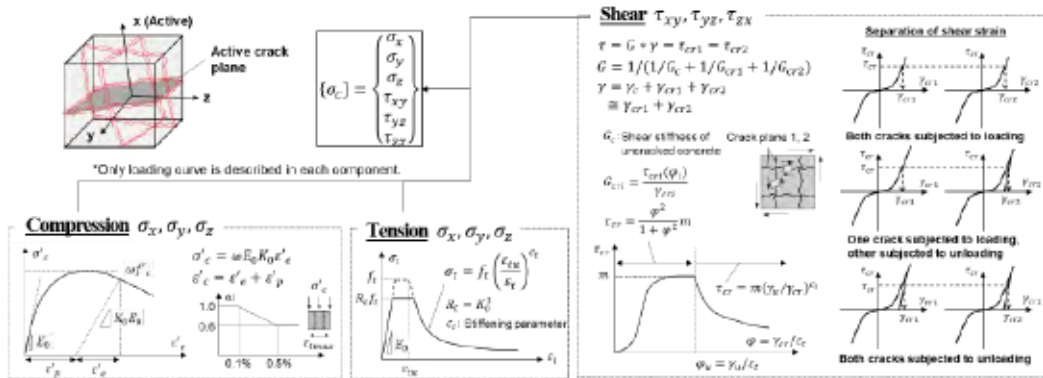


FIGURE 2.19: Calculation of crack concrete based on the active crack

## 2.9 Constitutive Model of Concrete for High-Cycle Fatigue in Compression, Tension, and Shear

To consider the time-dependent-high-cycle damage, the direct path-integral scheme is proposed and enhanced to compression, tension stiffening-softening, and shear transfer models. The proposed differential formula is verified by high cycle-fatigue experiments of dowel bars and pullout of reinforcement crossing a joint of structure concrete [2], [19]. The cyclic degradation is expressed by incremental plasticity and damage with respect to time and concrete strain. Here, the fracture parameter  $Kc$  is defined in the compression model. This value shows the capacity to store the elastic strain energy,

and the elastic strain path controls the damage evolution. Damage under high cyclic compression is expressed by the fracture degradation rate  $\lambda$  [25],[26]. For the tension model, the tensile fracture parameter  $K_T$  is a scalar to stand for path-dependent instantaneous fracture, time-dependent creep, and accumulation of fatigue damage [27]. Parameter  $X$  is assumed as fatigue damage of shear transfer based upon the contact density model and formulated by Gebreyouhannes [25],[26],[28]. Factors related to fatigue of the concrete model are listed in Figure 2.20 [19] and summarized in the following section.

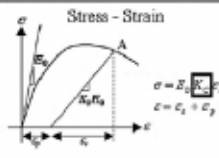
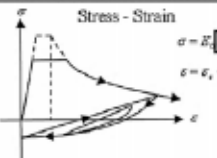
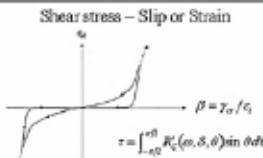
	Compression	Tension	Shear
Core Constitutive Laws	 <p>Mackawa et al. 2003</p>	 <p>Mackawa et al. 2003</p>	 <p>Mackawa et al. 2003</p>
Enhanced model for high cycle fatigue	<p>Fracture parameter <math>K_c</math> considers time dependent plasticity &amp; fracturing and cyclic fatigue damage</p> $dK_c = \left( \frac{\partial K_c}{\partial t} \right) dt + \left( \frac{\partial K_c}{\partial \epsilon_p} \right) d\epsilon_p$ <p>Time dependency <math>\frac{\partial K_c}{\partial t} = \lambda</math> when <math>F_s &gt; 0</math></p> <p>Cyclic fatigue <math>\left( \frac{\partial K_c}{\partial \epsilon_p} \right) = - \left( \frac{\partial F_s}{\partial \sigma_c} \right) \left( \frac{\partial F_s}{\partial K} \right) + \lambda</math> when <math>F_s = 0</math></p> $\lambda = K^2 \cdot (1 - K^4) \cdot g \cdot R$ <p>El-Kashif and Mackawa 2004</p>	<p>Fracture parameter <math>K_T</math> considers time dependent fracturing and cyclic fatigue damage</p> $dK_T = F dt + \left( \frac{\partial K_T}{\partial \sigma_t} \right) d\sigma_t + H d\epsilon_t$ <p>Time dependent fracturing <math>F</math></p> <p>Cyclic fatigue damage <math>\left( \frac{\partial K_T}{\partial \sigma_t} \right)</math></p> <p>Mackawa et al. 2003, Elbasue 2005</p>	<p>Accumulated path function <math>X</math> reduce shear associated with cyclic fatigue damage</p> $\tau = X \tau_o(\delta, \omega)$ <p>function Original model</p> $X = 1 - \frac{1}{10} \log_{10} \left( 1 + \int  d(\delta/\omega)  \right) \geq 0.1$ <p>Contact density model by Li &amp; Mackawa 1989 Modification of accumulated path function by Gebreyouhannes et al. 2006</p>
Physical meaning	Decrease of stiffness and plasticity accumulation by continuous fracturing concrete	Decrease of tension stiffness by bond fatigue	Decrease of shear transfer normal to crack by continuous deterioration of rough crack surface

FIGURE 2.20: Constitutive laws of concrete structure for high-cycle fatigue

### 2.9.1 High Cycle Fatigue of Concrete in Compression

The compression model of concrete is based on the scheme of elasto-plastic and fracture [27]. The basic constitutive equations for expressing the elasto-plastic and damaging concepts can be expressed as given as

$$\epsilon = \epsilon_e + \epsilon_p \quad (2-34)$$

The compressive stress  $\sigma$  associated with the elastic strain and compression fracture parameter  $K_c$  defined as

$$\sigma = E_0 \varepsilon_e K_c \quad (2-35)$$

Here,  $\varepsilon$  is the total compression strain,  $\varepsilon_e$  is elastic strains,  $\varepsilon_p$  is plastic strain, and  $E_0$  is the initial stiffness of concrete. The rate of plasticity  $\varepsilon_p$  and the rate of damage  $K_c$  are expressed as

$$d\varepsilon_p = \left( \frac{\partial \varepsilon_p}{\partial t} \right) dt + \left( \frac{\partial \varepsilon_p}{\partial \varepsilon_e} \right) d\varepsilon_e \quad (2-36)$$

$$dK_c = \left( \frac{\partial K_c}{\partial t} \right) dt + \left( \frac{\partial K_c}{\partial \varepsilon_e} \right) d\varepsilon_e \quad (2-37)$$

The strain increment indicates the instantaneous nonlinearity of the plain concrete as

$$\left( \frac{\partial \varepsilon_p}{\partial \varepsilon_e} \right) = 0 \text{ when } F_p > 0, \text{ and } \left( \frac{\partial \varepsilon_p}{\partial \varepsilon_e} \right) = - \left( \frac{\partial F_p}{\partial \varepsilon_e} \right) / \left( \frac{\partial F_p}{\partial \varepsilon_p} \right) \text{ when } F_p = 0 \quad (2-38)$$

$$\left( \frac{\partial K_c}{\partial \varepsilon_e} \right) = \lambda \text{ when } F_k < 0, \text{ and } \left( \frac{\partial K_c}{\partial \varepsilon_e} \right) = - \left( \frac{\partial F_k}{\partial \varepsilon_e} \right) / \left( \frac{\partial F_k}{\partial K_c} \right) + \lambda \text{ when } F_k = 0 \quad (2-39)$$

$\lambda$  is the accumulated damage rate which defines the instantaneous damaging of unconfined plain concrete, which validated the plastic potential  $F_p$  and the damage  $F_k$  by the experiments. The relevant parameters are defined as

$$F_p = \varepsilon_p - 0.038 \left[ \exp \left( \frac{\varepsilon_e}{0.55} \right) - 1 \right] \quad (2-40)$$

$$F_k = K - \exp[-0.73\beta(1 - \exp(-1.25\beta))] \quad (2-41)$$

$$\beta = -\frac{1}{0.35} \left[ \ln \left[ 1 - \frac{7\varepsilon_e}{20} \right] \right] \quad (2-42)$$

$$\lambda = K^3(1 - K)^4 g.R \quad (2-43)$$

$$R = 9\gamma^8 ; \gamma = -\frac{\varepsilon - \varepsilon_{e,tp}}{\varepsilon_{e,max}} \quad (2-44)$$

$$g = \frac{0.6}{1 + 10^{(30K-22)}} \text{ when } d\varepsilon_e < 0, \text{ otherwise } g = 0 \quad (2-45)$$

Where,  $K$  is the remaining effective volume,  $R$  is the effect of strain amplitude in high nonlinearity,  $\gamma$  indicates the normalized amplitude corresponding to updated stress variation,  $\varepsilon_{e,tp}$  denotes the turning point of compressive elastic strain, and  $\varepsilon_{e,max}$  is maximum elastic strain.

In order to apply for high-cycle fatigue, the slow-rate creep associated with ambient states in micropores becomes predominant at the middle and lower stress levels [2]. The simple linear creep rate represented by the linear viscous plasticity considered to cover the whole range of stress is added to the plastic rate function,  $\frac{\partial \varepsilon_p}{\partial t}$ ; then, the rate functions of plasticity and damage are given as

$$\frac{\partial \varepsilon_p}{\partial t} = \phi \left( \frac{\partial \varepsilon_p}{\partial t} \right)_b ; \left( \frac{\partial \varepsilon_p}{\partial t} \right)_b = 0.034 \left[ \exp \left[ \frac{\varepsilon_e}{4} \right] - 1 \right] \quad (2-46)$$

$$\phi = \exp \left[ -6 \left[ \frac{F_p^{0.6}}{\varepsilon_e^{1.2}} \right] \right] ; \frac{\partial K}{\partial t} = \left( \frac{\partial K}{\partial t} \right)_b \exp \left[ \xi \left[ \frac{K}{K - F_k} - 1 \right] \right] \quad (2-47)$$

$$\xi = 45(\psi^{-0.5(1-\exp(-5\varepsilon_c)))} \quad (2-48)$$

$$\left( \frac{\partial K}{\partial t} \right)_b = \left( \frac{\partial K}{\partial t} \right)_n (K - F_k) ; \left( \frac{\partial K}{\partial t} \right)_n = -0.05(0.95 - K + F_k)^2 \quad (2-49)$$

$$K - F_k < 0.95, \text{ otherwise } = 0$$

Where,  $\phi$  indicates the reduction factor in terms of the plastic evolution, and  $\xi$  is the integral acceleration.

## 2.9.2 High Cycle Fatigue of Concrete in Tension

Concrete is known as one that exhibits particularly large creep deformation, even under daily working stress. Tensile fatigue of concrete is attributed to bond creep deterioration with delay the cracking of the concrete, crack propagation, and reduction of tension stiffness of RC members after the initial cracking [24],[29]. Similar to the compression model, the tension nonlinearity is assumed to be governed by fracture damage rooted in cracks and expressed by stress and strain. Tensile stress  $\sigma$  is associated with elastic strain  $\varepsilon_e$  and fracture parameter  $K_T$  as

$$\sigma = E_0 \varepsilon_e K_T \quad (2-50)$$

The fracture parameter  $K_T$  is a scalar and standing for path-dependent instantaneous fracturing, time-dependent tension creep, and accumulated fatigue damage. Hence the total increment is given by

$$dK_T = Fdt + Gd\varepsilon + Hd\varepsilon \quad (2-51)$$

where,  $H$  is the instantaneous evolution of tension fracture defined as

$$H = -(1 + \alpha) \left[ \frac{f_t}{E_0} \right] \varepsilon_{cr}^\alpha \cdot \varepsilon_{max}^{-(\alpha+2)} ; \text{ when } d\varepsilon > 0 \text{ and } \varepsilon = \varepsilon_{max} \quad (2-52)$$

$$H = 0, \text{ when } d\varepsilon \leq 0 \text{ or } < \varepsilon_{max}$$

where  $\varepsilon_{cr}$  is the crack strain equal to  $2f_t/E_0$ , and  $\varepsilon_{max}$  is the maximum tensile strain in the past strain history measured from the compressive plastic strain.

$\alpha$  is 0.4 for RC; however, for plain concrete, it depends on the fracture energy in tension and the size of finite elements [30]. Here, the rate of damage is formulated in terms of  $S$  as,

$$S = \frac{E_0 K_T \varepsilon}{f_t} \quad (2-53)$$

where,  $f_t$  is the uniaxial tensile strength, and the rate of time-dependent fracture denoted by  $F$  as

$$F = -10^{-5} \cdot S^3 \cdot (K_T - 0.5)^2 \text{ when } \varepsilon_{max} < \varepsilon_{cr} \quad (2-54)$$

$$F = -10^{-6} \cdot S^6 \text{ when } \varepsilon_{max} \geq \varepsilon_{cr}$$

The cyclic fatigue damage in tension after cracking is expressed by  $G$  as

$$Gd\varepsilon = K_T \left( \frac{\sigma_{tp}}{\sigma_{env}} \right) \cdot d\varepsilon; \sigma_{env} = f_t \left( \frac{\varepsilon_{cr}}{\varepsilon_{tp}} \right)^\alpha \quad (2-55)$$

This formula is applied to the non-cracked state with  $\sigma_{tp}/\sigma_{env}=1.0$ .

### 2.9.3 High Cycle Fatigue Shear Transfer

The rate of the stiffness decrease was proposed from the original contact density modeling as [27]

$$\tau = X \cdot \tau_{or}(\delta, \omega) \quad (2-56)$$

$$X = 1 - \frac{1}{10} \log_{10} \left[ 1 + \int \left| d \left( \frac{\delta}{\omega} \right) \right| \right] \geq 0.1 \quad (2-57)$$

where,  $\tau_{or}$  is the transferred shear stress,  $\delta$  is the shear slip and  $\omega$  denotes the crack width, and  $X$  is the fatigue evolution factor to show the stiffness reduction of accumulated intrinsic shear deformation [27].

## References in Chapter 2

- [1] Wenfei Xue, 2016, "Design, Numerical Modelling and Analysis of a Spar Floater Supporting the DTU 10MW Wind Turbine," M.S. thesis, Marine Technology, Norwegian University of Science and Technology.
- [2] Maekawa, K., 2008, *Multi-Scale Modeling of Structural Concrete*, Crc Press.
- [3] Sarpkaya, T., 2010, *Wave Forces on Offshore Structures*, Cambridge university press.
- [4] Uzunoglu, E., 2019, "A System for the Hydrodynamic Design of Floating Wind Turbine Platforms," PhD thesis, Instituto Superior Tecnico, Lisbon, Portugal.

- [5] Architects, S. of N., and Engineers (US), M., 1918, *Transactions-The Society of Naval Architects and Marine Engineers*, Society of Naval Architects and Marine Engineers.
- [6] Wheeler, J. D., 1970, "Method for Calculating Forces Produced by Irregular Waves," *Journal of petroleum technology*, **22**(03), pp. 359–367.
- [7] Chakrabarti, S., 2005, *Handbook of Offshore Engineering (2-Volume Set)*, Elsevier.
- [8] Stansberg, C. T., Contento, G., Hong, S. W., Irani, M., Ishida, S., Mercier, R., Wang, Y., Wolfram, J., Chaplin, J., and Kriebel, D., 2002, "The Specialist Committee on Waves Final Report and Recommendations to the 23<sup>rd</sup> ITTC," *Proceedings of the 23<sup>rd</sup> ITTC*, **2**, pp. 505–551.
- [9] Jonkman, J. M., 2007, *Dynamics Modeling and Loads Analysis of an Offshore Floating Wind Turbine*, University of Colorado at Boulder.
- [10] Faltinsen, O., 1993, *Sea Loads on Ships and Offshore Structures*, Cambridge university press.
- [11] Munson, B. R., Young, D. F., Okiishi, T. H., and Huebsch, W. W., 2006, "Fundamentals of Fluid Mechanics, John Wiley & Sons," Inc., USA.
- [12] Federation of American Scientists, M. A. N., "Damage Control Training Stability and Buoyancy Lessons" [Online]. Available: <https://man.fas.org/dod-101/navy/docs/swos/dca/stg4-01.html>.
- [13] Dr. Pepijn de Jong, "Offshore Hydromechanics Module 1" [Online]. Available: [https://ocw.tudelft.nl/wp-content/uploads/3.OffshoreHydromech1\\_PotentialFlowsPart1.pdf](https://ocw.tudelft.nl/wp-content/uploads/3.OffshoreHydromech1_PotentialFlowsPart1.pdf).
- [14] Lee, C. H., and Newman, J. N., 2013, "WAMIT User Manual, Version 7.0," WAMIT Inc, Chestnut Hill, Massachusetts.
- [15] de Souza, C. E. S., 2022, "Structural Modelling, Coupled Dynamics, and Design of Large Floating Wind Turbines."
- [16] DNV, 2010, "Environmental Conditions and Environmental Loads (DNV-RP-C205)."

- [17] 2022, "Morison Equation," Wikipedia [Online]. Available: [https://en.wikipedia.org/w/index.php?title=Morison\\_equation&oldid=1104433788](https://en.wikipedia.org/w/index.php?title=Morison_equation&oldid=1104433788).
- [18] Maekawa, K., and Ishida, T., 2017, "MULTI-SCALE CONCRETE MODEL DuCOM-COM3 USERS MANUAL and GUIDE."
- [19] Maekawa, K., Okamura, H., and Pimanmas, A., 2003, *Nonlinear Mechanics of Reinforced Concrete*, CRC Press.
- [20] Collins, M. P., and Mitchell, D., 1997, *Prestressed Concrete Structures*, Response Publications.
- [21] Yamanoi, Y., 2022, "Multi-Directional Crack Model for Cementitious Composites in Consideration of Shear Graveling," Ph.D. thesis, Yokohama National University.
- [22] Okamura, H., and Maekawa, K., 1991, *Nonlinear Analysis and Constitutive Models of Reinforced Concrete*, Gihodo-Shuppan Co, Tokyo.
- [23] Nguyen, H. Q. H., 2020, "High Cycle Fatigue Modeling of Concrete Pavement Coupled with Soil Foundation," Ph.D. thesis, Yokohama National University.
- [24] Quadri, A. I., and Fujiyama, C., 2021, "Numerical Analysis of RC Gerber Bridge Girder Subjected to Fatigue Loading," *Bridge Maintenance, Safety, Management, Life-Cycle Sustainability and Innovations*, H. Yokota, and D.M. Frangopol, eds., CRC Press, pp. 2682–2689.
- [25] Takahashi, Y., Tanaka, Y., and Maekawa, K., 2018, "Computational Life Assessment of ASR-Damaged RC Decks by Site-Inspection Data Assimilation," *Journal of Advanced Concrete Technology*, **16**(1), pp. 46–60.
- [26] Maekawa, K., and El-Kashif, K. F., 2004, "Cyclic Cumulative Damaging of Reinforced Concrete in Post-Peak Regions," *Journal of Advanced Concrete Technology*, **2**(2), pp. 257–271.
- [27] Maekawa, K., Toongoenthong, K., Gebreyouhannes, E., and Kishi, T., 2006, "Direct Path-Integral Scheme for Fatigue Simulation of Reinforced Concrete in Shear," *Journal of Advanced Concrete Technology*, **4**(1), pp. 159–177.



- [28] Gebreyouhannes, E., 2006, "Shear Transfer of Cracked Concrete under Fatigue Loading," *6<sup>th</sup> International PhD Symposium in Civil Engineering*, p. 58.
- [29] Subramaniam, K. V., Popovics, J. S., and Shah, S. P., 2002, "Fatigue Fracture of Concrete Subjected to Biaxial Stresses in the Tensile C-T Region," *Journal of engineering mechanics*, **128**(6), pp. 668–676.
- [30] Bažant, Z. P., and Oh, B. H., 1983, "Crack Band Theory for Fracture of Concrete," *Matériaux et construction*, **16**(3), pp. 155–177.

## CHAPTER 3

### COUPLED DYNAMIC ANALYSIS OF A FLOATING WIND TURBINE

#### 3.1 Introduction

The aim of this chapter is to determine the feasible geometry of a concrete spar floater supporting a 10MW offshore wind turbine. After that, the dynamic behavior of the spar coupled with the reference wind turbine, steel tower, and mooring lines will be numerically investigated in the couple dynamic analysis. The first trial geometry of the spar is defined to achieve hydrostatic stability in parametric and sensitivity analysis by not considering the mooring system. The motion behavior under wave action of the structure will be evaluated using WAMIT [1], and coupled dynamics analysis during the operation of the wind turbine structure will be performed by OpenFAST [2]. Cross-spectral analysis of the rigid body is performed to investigate the response motions of the proposed model and thereby ensure that the spar can be applied to support an RWT. The coupled dynamics simulation outputs in the time domain will be applied as the forces in the FE analysis of the concrete. Figure 3.1 shows the concept of interfacing modules employed to achieve coupled dynamic and concrete FE analyses, which the yellow background is operated by OpenFAST.

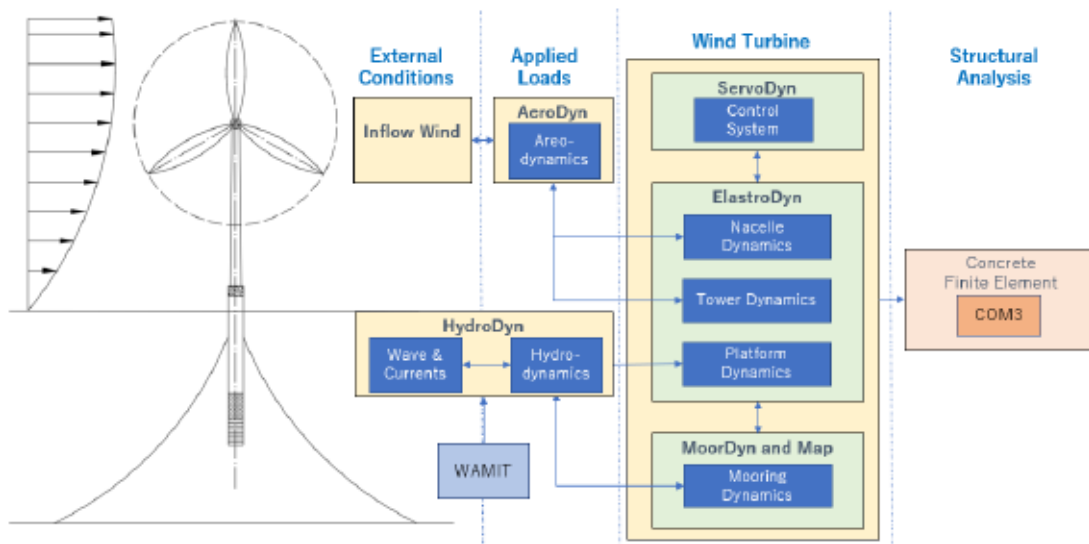
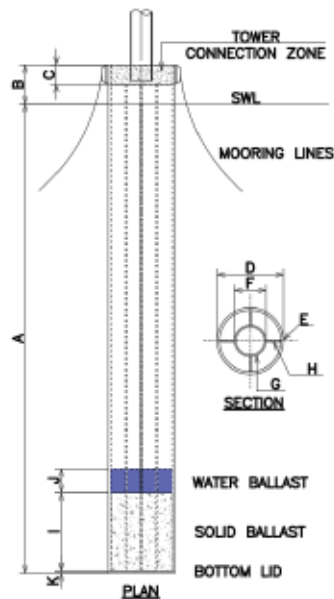


**FIGURE 3.1:** Interfacing modules employed to achieve coupled dynamics and concrete FE analyses

### 3.2 Parametric Analysis

In the conceptual design presented in this research, the platform is considered to be a simple cylindrical hull comprising two parts: a submerged part that carries the ballast tanks and an emerged part that consists of fairleads for the mooring lines and the tower connection. Normal concrete compressive strength 41 MPa with a density of 25 kN/m<sup>3</sup> is considered in the design of spar concrete. The ballast control system is designed considering the spar installation process to comprise both solid ballast (black blast furnace slag with a unit weight of 28.00 kN/m<sup>3</sup>) and liquid ballast (seawater with a density of 10.26 kN/m<sup>3</sup>). Each part of the spar is defined using 11 parameters, labeled A to K, in the parametric analysis. The parameters A, D, and E are modified to achieve a feasible initial trial geometry. Figure 3.2 presents the main spar dimensions and variables considered in the parametric analysis [3].



Parametric variable

A: Hull draft

B: Hull air gap

C: Hull tower connection

D: Hull external diameter

E: Hull thickness

F: Hull internal tank diameter

G: Hull internal tank thickness

H: Hull internal wall thickness

I: Fixed ballast height

J: Water ballast height

K: Bottom lid

**FIGURE 3.2:** Main dimensions and variables of the spar considered during the parametric analysis.

### 3.3 Sensitivity Analysis

A feasible spar geometry, regardless of the mooring system employed, must have sufficient hydrostatic stability as required by DNV's restriction [4]. The IEA 10-MW RWT [5] is used as a reference wind turbine, and the key parameters are shown in Table 3.1.

**TABLE 3.1:** Key parameters of the IEA 10-MW RWT

Parameter	Value
Wind Regime	IEC class 1A
Rotor Orientation	clockwise rotation-upwind
Control	variable speed, collective pitch
Cut-in wind speed	4 m/s
Cut-out wind speed	25 m/s
Rated wind speed	11 m/s
Rated electrical power	10 MW
Number of blades	3
Rotor diameter	198 m
Hub diameter	4.6 m
Hub height	119.0 m
Minimum rotor speed	6.0 rpm
Maximum rotor speed	8.68 rpm
Blade mass	47,700 kg (each)
Nacelle mass	542,600 kg
Tower mass	628,442 kg

The spar diameter  $D$  is varied from 12.00 to 24.00 m to determine a feasible geometry, and the hull thickness  $E$  is varied from 0.45 to 0.85 m, considered to be within the range of appropriate prestressed concrete thickness. The metacentric height (GM) and pitch angle are restricted indicators used to characterize the target structure. The lower limit of GM is set to 1.00 m, and the upper limit of the pitch angle is set to  $7.00^\circ$  [4]. Figure 3.3 shows the sensitivity analysis results of feasible geometries with five different hull thicknesses. The results indicated the preferability of the first trial geometry with a diameter of 18.00 m, thickness of 0.45 m,

draft of 123.00 m, GM of 7.32 m, and pitch angle of 6.98°. These dimensions are confirmed to satisfy the intact stability criteria [4] and are therefore applied in the subsequent analysis.

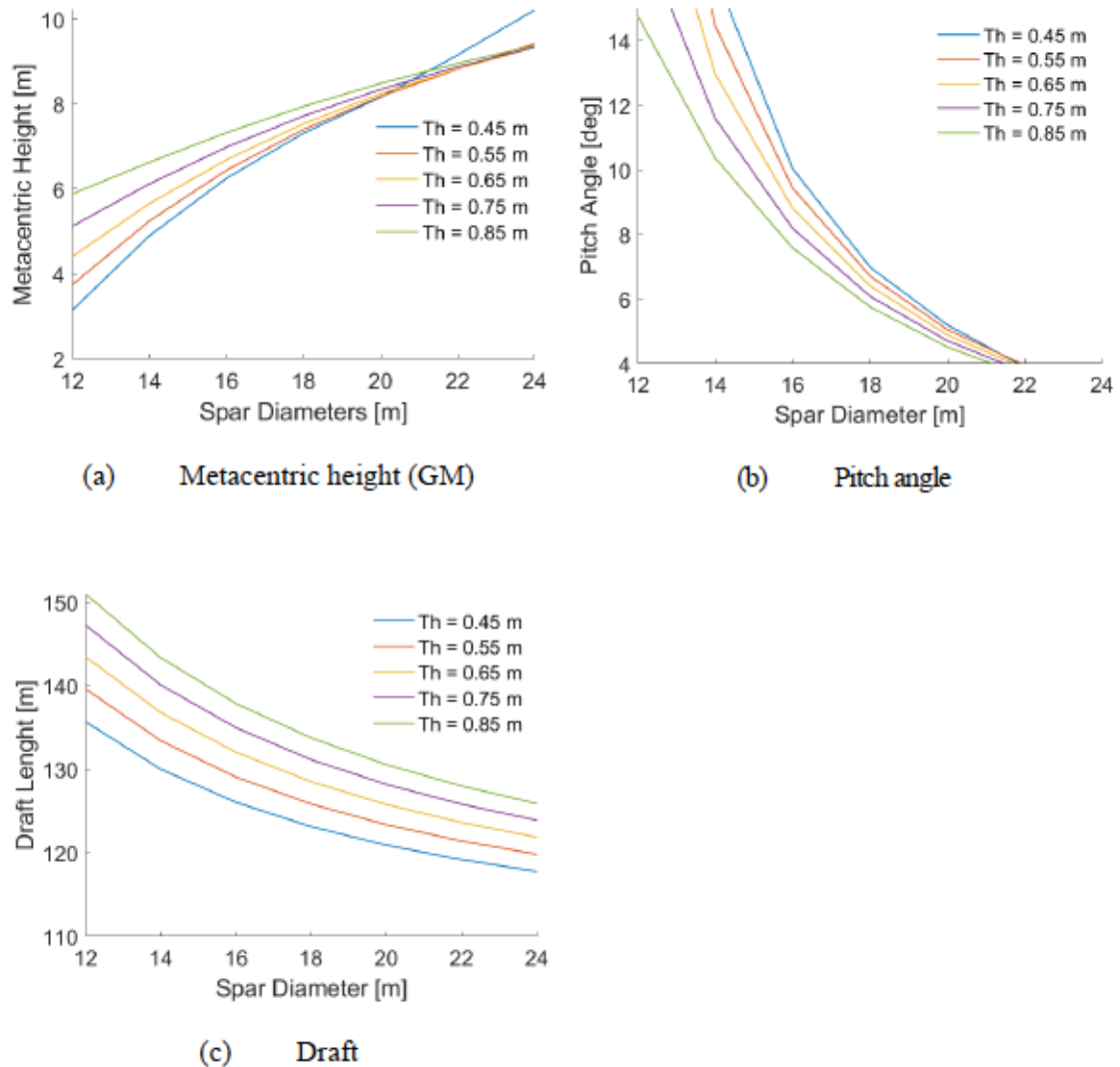


**FIGURE 3.3:** Sensitivity analysis of spar dimensions at different hull diameter and thicknesses

### 3.4 Hydrostatic Modeling

The hydrostatic properties at the equilibrium of the coupling model, comprising the target spar, RWT, and mooring lines, are evaluated using EDToolsX® to prepare the model for hydrodynamic analysis using the WAMIT code. In this case, mooring lines are included as an external linear stiffness matrix in the WAMIT model [6]. The EDToolsX® software [7], which calculates the full stiffness matrix using the formulation

presented in [8], is used to evaluate the stiffness matrix. The non-diagonal terms attributed to the degree-of-freedom coupling are also considered. The mooring line characteristics and coordinates are presented in Table 3.2, with each line at an angle of 120. The full-scale coupling model is presented in Figure 3.4

**TABLE 3.2:** Mooring system properties and coordinates

Line no.	Material	Chain diameter [m]	Unstretched length [m]	Mooring load [Ton]
Line 1	R4 stud	0.095	550	104.96
Line 2	R4 stud	0.095	550	100.67
Line 3	R4 stud	0.095	550	100.67
Line no.	Anchor X [m]	Anchor Y [m]	Anchor Z [m]	
Line 1	500	0.00	-220	
Line 2	-250	433.01	-220	
Line 3	-250	-433.01	-220	
Line no.	Fairlead X [m]	Fairlead Y [m]	Fairlead Z [m]	
Line 1	8.50	0.00	125	
Line 2	-4.25	7.36	125	
Line 3	-4.25	-7.36	125	

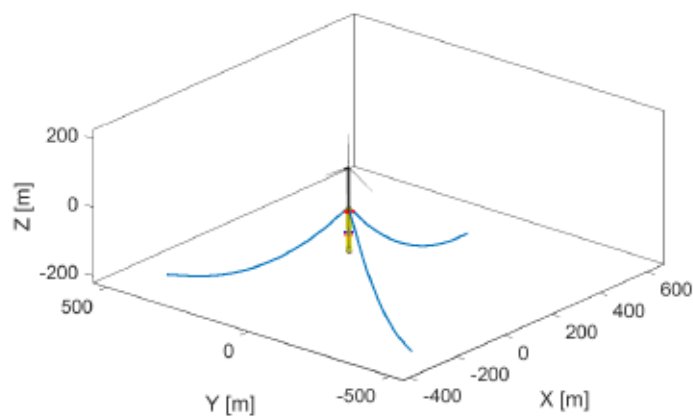


**FIGURE 3.4:** 3D view of the trial geometry including the mooring lines in Edtoolsx®

### 3.5 Hydrostatic Equilibrium

Table 3.3 shows the results of the main parameters at hydrostatic equilibrium. The structural properties of the coupling model under no-wind conditions are listed in Table 3.4. The results show that the spar diameter  $D$  needs to be adjusted to 17.00 m, the fixed ballast height (solid ballast)  $I$  to 10.50 m, the water ballast height  $J$  to 5.73 m, and the hull thickness  $E$  to 0.60 m at hydrostatic equilibrium. The final required draft is relatively close to the preliminary geometry obtained using a simple calculation; however, the spar diameter changed owing to the inclusion of the mooring and ballast system. The righting/heeling moment curves of the final spar geometry at static equilibrium are shown in Figure 3.5. The hydrostatic property obtained from this section will be applied in the subsequent coupled dynamic analysis.

**TABLE 3.3:** Trial geometry parameters

Parametric variable	[m]
A: Hull draft	120.00
B: Hull air gap	10.00
C: Hull tower connection	5.00
D: Hull external diameter	17.00
E: Hull thickness	0.60
F: Hull internal tank diameter	8.00
G: Hull internal tank thickness	0.40
H: Hull internal wall thickness	0.40
I: Fixed ballast height	10.50
J: Water ballast height	5.73
K: Bottom lid	0.60

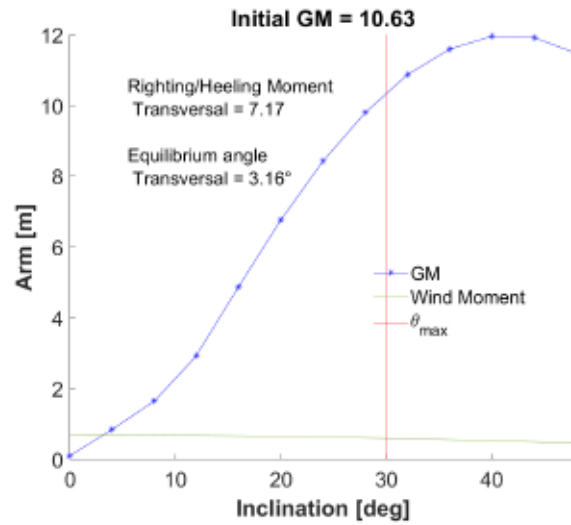


**FIGURE 3.5:** Righting/heeling moment

**TABLE 3.4:** Spar properties at equilibrium condition

Structural property	Value
Structural mass [ton]	26,965.00
Mooring vertical load [ton]	306.31
Displacement [ton]	27,227.05
CG [m]	-0.21, 0.00, 51.53
CB [m]	-0.00, 0.00, 60.04
Draft [m]	-120.08
GM [m]	10.63

### 3.6 Environmental Condition

#### 3.6.1 Wave Condition

In this study, wave conditions from locations around the Japanese coast are selected and described using the International Ship and Offshore Structures Congress (ISSC) spectrum [9], as shown in Figure 3.6, in which  $T_p$  represents the peak period of the wave spectrum, and  $H_s$  represents the significant wave height. Three wave conditions are evaluated in this study: operational, storm, and centenary. The irregular wave condition parameters for each condition are listed in Table 3.5 [6].



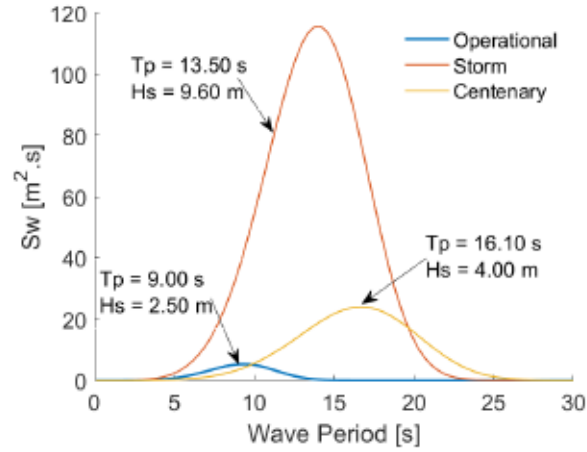


**FIGURE 3.6:** ISSC wave spectrum for the selected Japanese environmental conditions

**TABLE 3.5:** Irregular wave condition parameters

Condition	Significant height ( $H_s$ )	Period of peak ( $T_p$ )
Operational	2.50	9.00
Storm	9.60	13.50
Centenary	4.00	16.10

The ISSC spectrum can be expressed as follows.

$$S_w(f) = \frac{\alpha}{f^5} \exp\left(-\frac{\beta}{f^4}\right) \quad (3-1)$$

where  $f$  represents the wave frequency and  $f_p$  represents the frequency of the peak of the wave spectrum, defined as:

$$\bar{f} = 1.25f_p \quad (3-2)$$

The  $\alpha$  and  $\beta$  parameters in Eq. (1) are expressed as follows:

$$\alpha = 0.1107H_s^2\bar{f}^4 \quad (3-3)$$

$$\beta = 0.4427\bar{f}^4 \quad (3-4)$$

### 3.6.2 Wind Condition

The wind conditions applied with irregular waves in the coupled dynamics analysis are listed in Table 3.6.

**TABLE 3.6:** Wind speed condition parameters

Condition	Wind speed $U$ [m/s]
Maximum operation	11.00
Cut-out wind speed	25.00
Typhoon	41.90

## 3.7 Coupled Dynamic Analysis

### 3.7.1 Verification of Coupled Dynamic Model and Resonance Assessment

For the hydrodynamic stability and motion analyses, the response amplitude operator (RAO), defined as Equation 3-5, is used to access the frequency-domain linear wave-body responses of the spar platform [10]. The RAOs in the sway, roll, and yaw motions are found to be nearly zero because of the symmetric condition for a wave incidence of  $0^\circ$ . The RAOs of the surge, heave, and pitch motions computed by WAMIT and OpenFAST without wind conditions at wave incidence  $0^\circ$  are shown in Figure 3.7.

Comparisons of the results obtained using WAMIT and OpenFAST are undertaken to validate the use of the OpenFAST model under conditions with waves only also shown in Figure 3.7. Although OpenFAST exhibited small deviations owing to the coupled dynamic response under the operation of the ServoDyn, wind turbine control system, the results implied good agreement with WAMIT in terms of surge and heave motions under no-wind conditions. However, this coupled dynamic response decreased the pitch motion response. The effects of the wind turbine operation on the pitch motion must be therefore investigated in future studies.

The maximum amplitudes of the RAOs represent the resonance phenomena from which the platform's natural period can be derived. Ocean waves possess significant energy in the 5–25 s period range [11]; the RAO results indicated that the natural period of the spar structure is beyond this range, except for the heave motion. The natural period for heave is 22.00 s, nearly the same as the ocean wave period; however,

this is beyond the expected range for the installation location considered in this study [12], as indicated by the wave spectra in Figure 3.6. These results imply that the proposed FOWT structure can avoid any structural resonance induced by wave excitation.

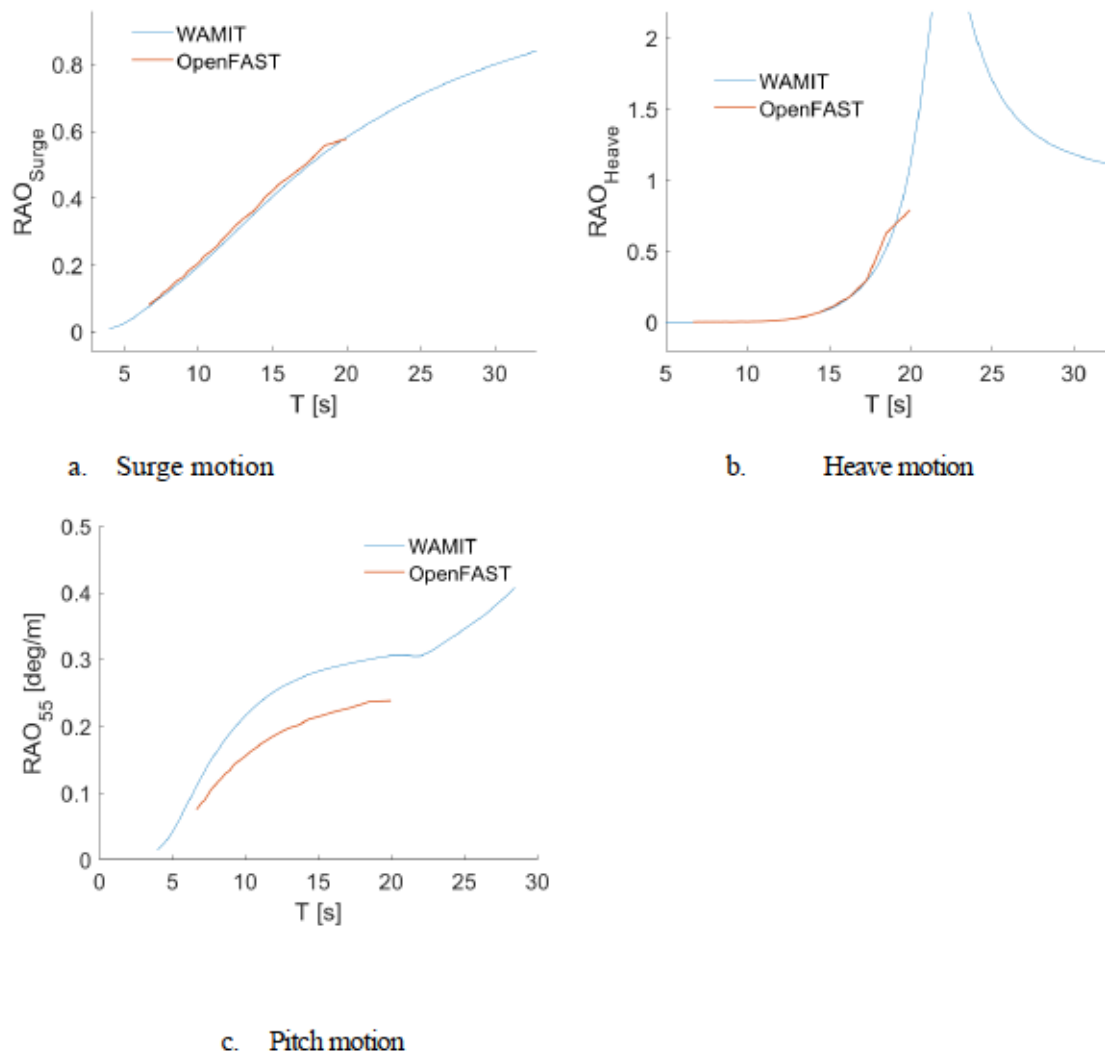


**FIGURE 3.7:** RAO comparison of WAMIT and OpenFAST results without wind

### 3.7.2 Spectral Analysis of Rigid Body Motion

A spectral analysis considering rigid body motion is then conducted to estimate the dynamic properties of the proposed model under actual input wave and wind conditions to confirm this behavior [13].

The power spectrum of motion response can be calculated as

$$S_{ii}(f) = |RAO_{ii}(f)|^2 S_w(f) \quad (3-5)$$

where  $ii$  represents the  $i$ -index corresponding to the  $DOF$ , which is 11, 33, and 55 for surge, heave, and pitch motions, respectively, and  $S_w$  is the power spectrum of the wave.

The variance of the motion response can be estimated at the 0<sup>th</sup> moment  $m_0$  as

$$m_0 = \int S_{ii}(f) df \quad (3-6)$$

Then, the significant motion response  $Hs$  can be computed as  $4\sqrt{m_0}$ .

The significant response  $Hs$  of the cross-spectrum analysis using the three sea states presented in Figure 3.6 and Table 3.5 are presented in Table 3.7.

**TABLE 3.7:** Spectral analysis results using WAMIT

WAMIT			
Wave	Surge $Hs$	Heave $Hs$	Pitch $Hs$
Operational	0.37	0.01	0.41
Storm	2.98	1.80	2.32
Centenary	1.60	2.41	1.06

Examples of spectral analysis results are shown in Figure 3.8, in which the power cross-spectra in the surge, heave, and pitch motion responses attributed to storm conditions are presented together with the corresponding input wave ISSC spectrum. The results show that significant response motions are much smaller than the input wave energies. This confirmed the structure successfully avoids structural resonance induced by wave excitation.

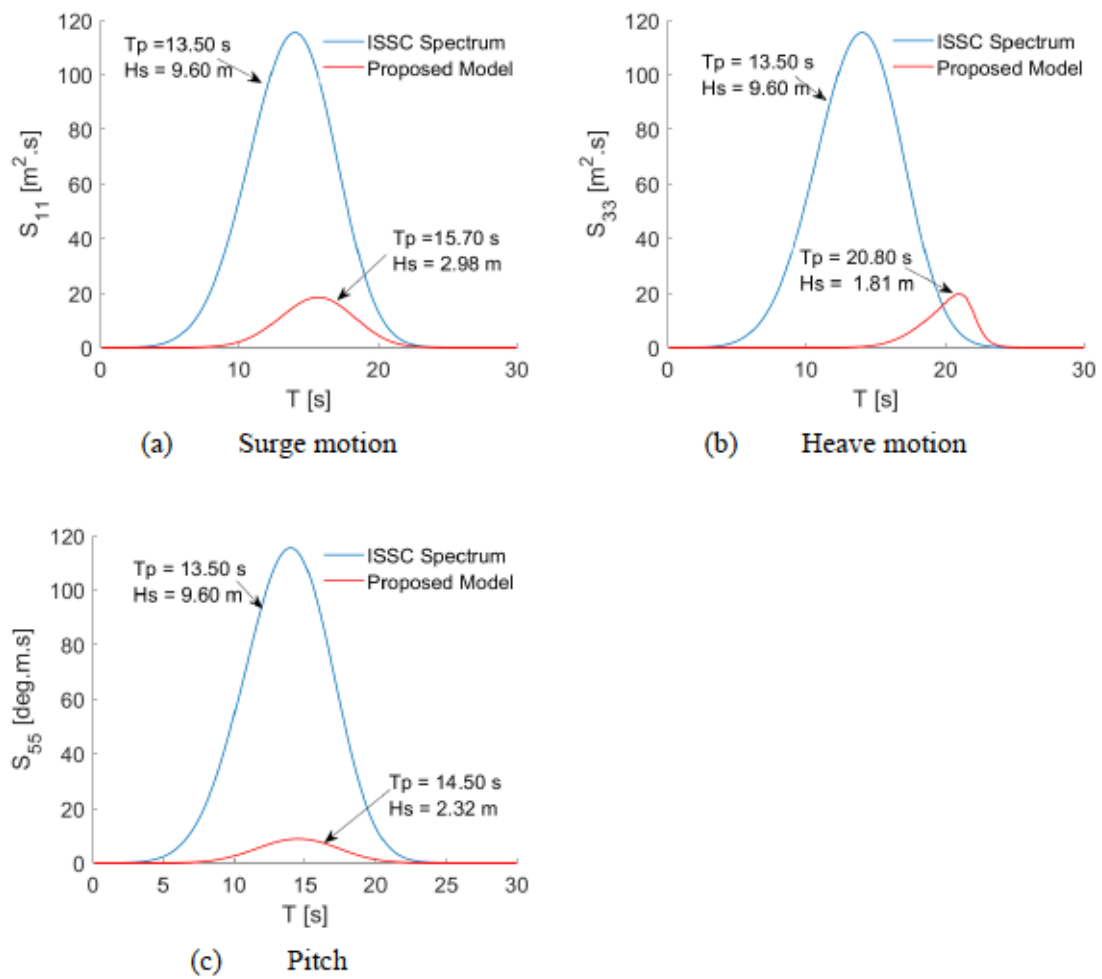
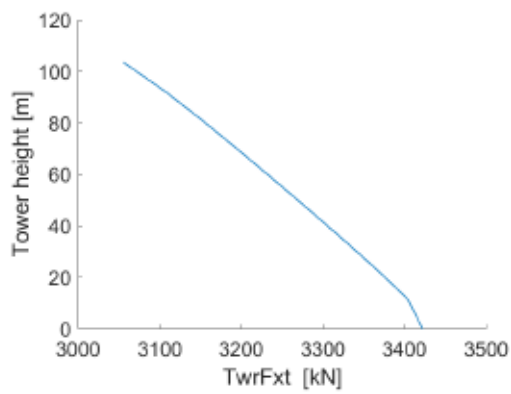


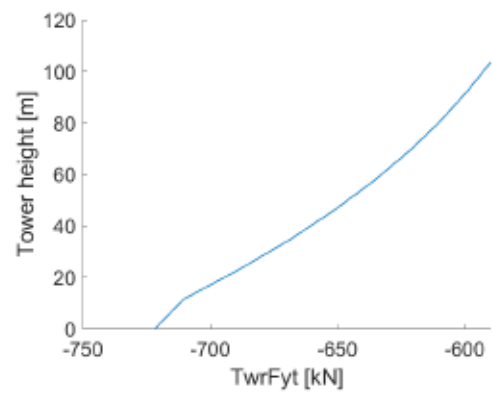
**FIGURE 3.8:** Power spectra of motion response attributed to the storm condition

### 3.8 Coupled Dynamic Analysis Results

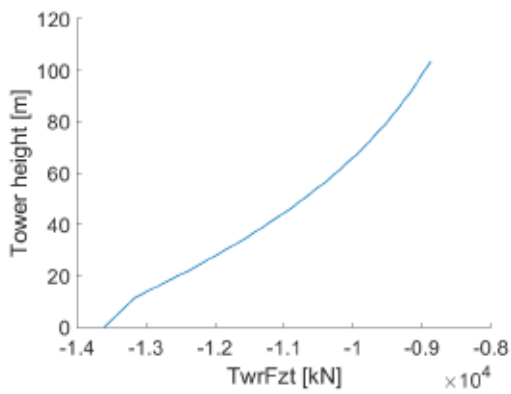
The examples of the force distributions along tower height at wind speed 11 m/s under storm wave obtained from OpenFAST and the tower base forces in the time domain at the same condition are presented in Figures 3.9 and 3.10, respectively.



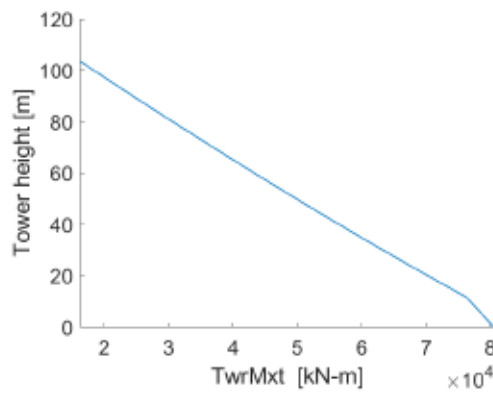
(a) Shear force in the x-direction



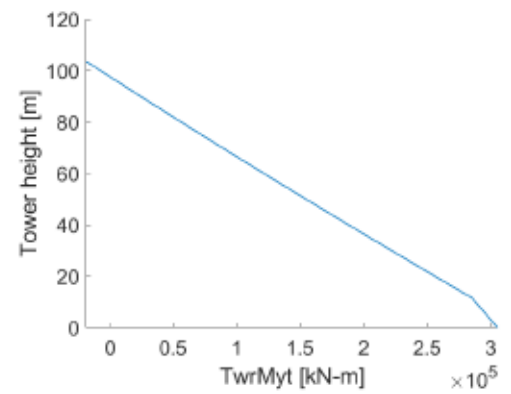
(b) Shear force in the y-direction



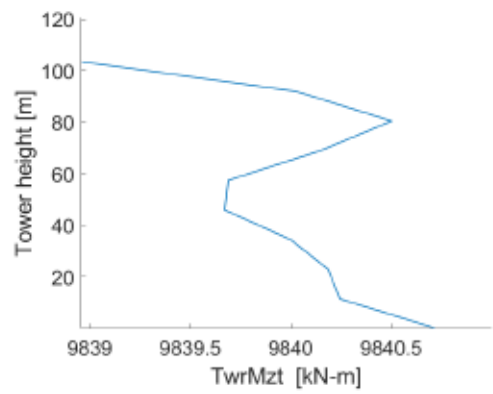
(c) Shear force in the z-direction



(d) Bending moment in the x-direction

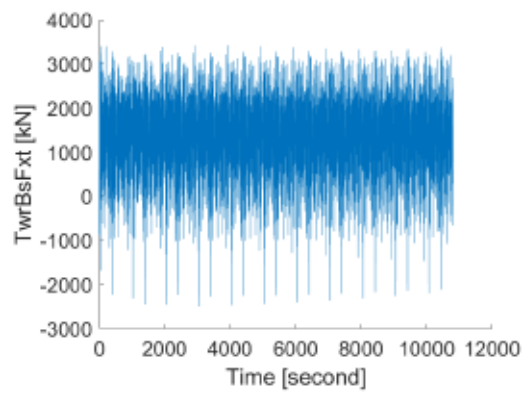


(e) Bending moment in the y-direction

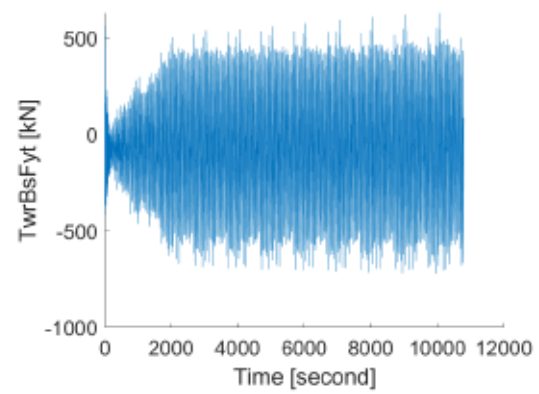


(f) Bending moment in the z-direction

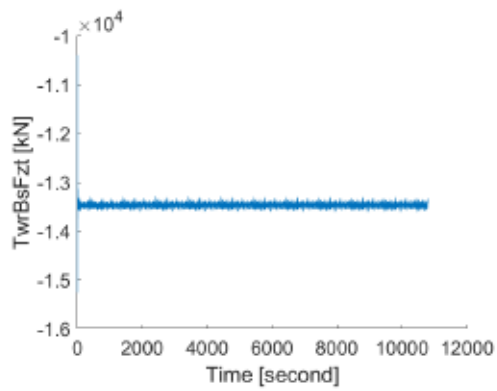
**FIGURE 3.9:** Local tower load distribution at wind speed 11 m/s under storm condition



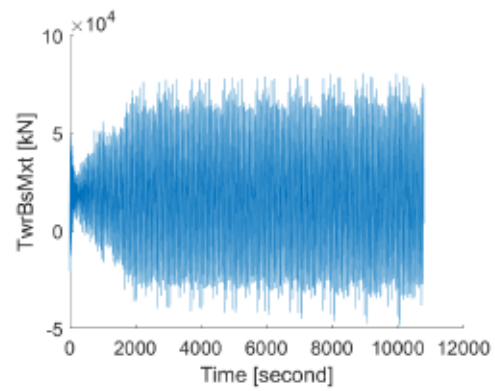
(a) Tower base shear force in the x-direction



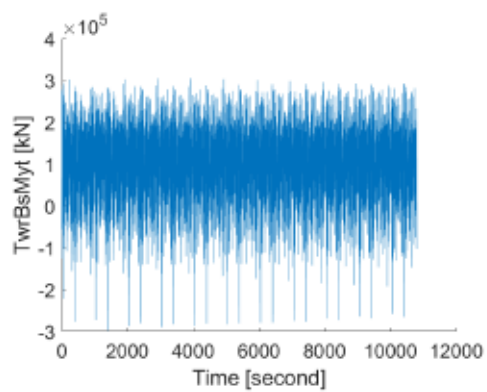
(b) Tower base shear force in the y-direction



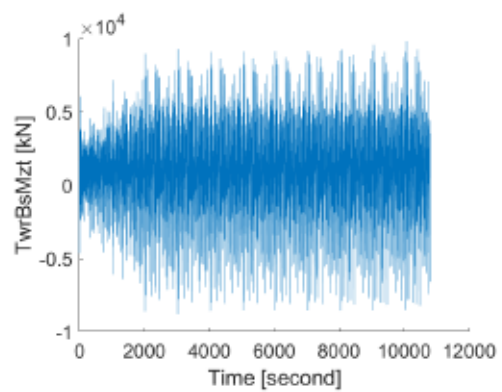
(c) Tower base shear force in the z-direction



(d) Tower base bending moment in the x-direction



(e) Tower base bending moment in the y-direction



(f) Tower base bending moment in the z-direction

**FIGURE 3.10:** Tower base force at wind speed 11 m/s under storm condition

In this research, the highest forces selected from the dominant case of coupled dynamics simulation outputs in the time domain of OpenFAST will be applied to the FEM as static forces. The tower base and mooring forces of the nine evaluated cases indicate the storm condition with a rated wind speed of 11 m/s yielded the highest tower base forces and mooring forces, as presented in Table 3.8. These results are expected because the rated wind speed of the RWT is set according to the maximum rotor thrust that can be accommodated by its control system [5]. These forces will be applied as the 20-time-step-monotonic static load in consequent FE analysis.

**TABLE 3.8:** Maximum force obtained from coupled dynamic analysis

Parameter	Operational Condition			Storm Condition		
	11 [m/s]	25 [m/s]	41.9 [m/s]	11 [m/s]	25 [m/s]	41.9 [m/s]
<i>Max.TwrBsFxt</i> [kN]	2994	2046	-1194	3422	3354	-2907
<i>Mean.TwrBsFxt</i> [kN]	1365	538	-205	1318	536	-205
<i>Max.TwrBsFyt</i> [kN]	-372	-947	111	-722	-1232	262
<i>Mean.TwrBsFyt</i> [kN]	-71	-381	0	-66	-380	0
<i>Max.TwrBsFzt</i> [kN]	-13537	-13480	-13404	-13609	-13568	-13533
<i>Mean.TwrBsFzt</i> [kN]	-13468	-13382	-13327	-13467	-13379	-13323
<i>Max.TwrBsMxt</i> [kN.m]	47661	102025	-10711	80551	128953	-25624
<i>Mean.TwrBsMxt</i> [kN.m]	18493	50098	-3	18003	49962	-7
<i>Max.TwrBsMyt</i> [kN.m]	261274	162804	-178273	305523	-291623	-344843
<i>Mean.TwrBsMyt</i> [kN.m]	102501	18364	-72361	97250	18187	-72367
<i>Max.TwrBsMzt</i> [kN.m]	3160	18407	4110	9841	30200	7808
<i>Mean.TwrBsMzt</i> [kN.m]	861	12399	0	905	12293	-1
<i>Max.PtfmSurge</i> [m]	23	11	2	21	11	4
<i>Mean.PtfmSurge</i> [m]	15	8	2	15	0	2
<i>Max.Heave</i> [m]	2113	5	5	6	6	6
<i>Mean.Heave</i> [m]	1548	5	5	5	5	5
<i>Max.Pitch</i> [°]	3	-3	-1	-3	-4	-3
<i>Mean.Pitch</i> [°]	0	0	-1	0	0	-1
<i>Max.RoThrust</i> [kN]	2113	1150	412	2343	1610	753
<i>Mean.RoThrust</i> [kN]	1548	721	175	1510	716	175
<i>Mean.MoorTension</i> [kN]	7916	2363	1590	7514	2386	1623



**TABLE 3.8:** Maximum force obtained from coupled dynamic analysis (continue)

Parameter	Centenary Condition		
	11 [m/s]	25 [m/s]	41.9 [m/s]
<i>Max.TwrBsFxt</i> [kN]	2988	2103	-1163
<i>Mean.TwrBsFxt</i> [kN]	1350	538	-205
<i>Max.TwrBsFyt</i> [kN]	-319	-964	-125
<i>Mean.TwrBsFyt</i> [kN]	-71	-381	0
<i>Max.TwrBsFzt</i> [kN]	-13590	-13534	-13449
<i>Mean.TwrBsFzt</i> [kN]	-13467	-13382	-13327
<i>Max.TwrBsMxt</i> [kN.m]	42608	103313	11512
<i>Mean.TwrBsMxt</i> [kN.m]	18402	50079	-6
<i>Max.TwrBsMyt</i> [kN.m]	259181	165663	-168402
<i>Mean.TwrBsMyt</i> [kN.m]	100778	18378	-72347
<i>Max.TwrBsMzt</i> [kN.m]	3297	20783	-2562
<i>Mean.TwrBsMzt</i> [kN.m]	859	12385	0
<i>Max.PtfmSurge</i> [m]	22	11	3
<i>Mean.PtfmSurge</i> [m]	15	8	2
<i>Max.Heave</i> [m]	6	6	6
<i>Mean.Heave</i> [m]	5	5	5
<i>Max.Pitch</i> [°]	3	-4	-2
<i>Mean.Pitch</i> [°]	0	0	-1
<i>Max.RoThrust</i> [kN]	2207	1231	375
<i>Mean.RoThrust</i> [kN]	1534	720	175
<i>Mean.MoorTension</i> [kN]	7781	2340	1590

The motion statistics obtained by the time domain calculation in OpenFAST, calculated considering only the steady-state range of the time series are presented in Table 3.9. For the OpenFAST calculations, the wind conditions presented in Table 3.6 are utilized to observe the impact of the wind turbine operation on the motions. Combinations of different wave conditions and wind speeds are also considered, as presented in Table 3.9. Notably, wind turbine operation increases all significant motions of the platform, particularly the pitch motion, implying that wind effects must be considered in any further optimization processes.

**TABLE 3.9:** Motion statistics obtained using OpenFAST

Motion statistics (OpenFAST)							
Wave condition	Wind speed	Surge $H_s$	Surge $H_{max}$	Heave $H_s$	Heave $H_{max}$	Pitch $H_s$	Pitch $H_{max}$
Operational	No wind	0.78	3.08	0.04	0.45	0.49	1.81
Operational	11 m/s	5.69	23.49	0.10	0.34	7.61	5.92
Operational	25 m/s	2.48	11.34	0.08	0.41	7.59	5.83
Storm	41 m/s	3.30	6.92	0.97	1.37	1.84	5.87
Centenary	41 m/s	2.02	5.81	0.89	1.16	0.97	3.80

### 3.9 Conclusion for Chapter 3

A precast segment prestressed concrete spar platform intended for mass production capable of supporting a 10 MW offshore RWT is developed and successfully demonstrated in this study as an alternative to a steel spar. The following conclusions are drawn from the obtained results:

1. The proposed concrete spar can be applied to support an RWT. The structure is shown to avoid the structural resonance induced by wave excitation, as confirmed by a spectral analysis that indicates significant response motions that are much smaller than the input wave energies.
2. The motions of the wind turbine determined by OpenFAST calculations indicate that the wind turbine operation increases all significant motions of the spar, particularly the pitch motion. The wind effects must therefore be included in further spar design optimization processes.
3. A rated-wind speed under the storm condition, in which the waves exhibit their highest energy, can be considered as the dominant case for the design of the spar. The highest forces can be expected at the rated wind speed because at this value, the rotor thrust coefficient that governs the rotor thrust force generated by the control system of the RWT is the highest. Although the typhoon condition produces the highest wind speeds, this wind would result in a relatively small thrust force as the control system will manipulate the wind turbine to shut it down.

### Nomenclature in Chapter 3

A	hull draft length
B	hull air gap length
C	hull–tower connection length
CG	center of gravity
COB	center of buoyancy
D	hull external diameter
DOF	degree of freedom
E	hull thickness
$f$	wave frequency
$f_p$	peak of the wave frequency spectrum
F	hull internal tank diameter
FE	finite element
FOWT	floating offshore wind turbine
G	hull internal tank thickness
GM	metacentric height
H	hull internal tank wall thickness
$H_{max}$	maximum wave height
$H_s$	significant wave height
I	fixed ballast height
$i$	$i$ -index corresponding to DOF
IEA	International energy agency
ISSC	International ship and offshore structure congress
J	water ballast height
K	bottom lid height
$Max.PtfmPitch$	maximum platform pitch angle
$Max.PtfmSurge$	maximum platform surge motion

<i>Max.TwrBsFxt</i>	maximum tower base shear force in the x direction
<i>Max.TwrBsFyt</i>	maximum tower base shear force in the y direction
<i>Max.TwrBsFzt</i>	maximum tower base shear force in the z direction
<i>Max.TwrBsMxt</i>	maximum tower base bending moment in the x direction
<i>Max.TwrBsMyt</i>	maximum tower base bending moment in the y direction
<i>Max.TwrBsMzt</i>	maximum tower base bending moment in the z direction
<i>Max.RoThrust</i>	maximum thrust force of the wind turbine rotor
<i>Mean.MoorTension</i>	mean mooring line tension
<i>Mean.PtfmPitch</i>	mean platform pitch angle
<i>Mean.PtfmSurge</i>	mean platform surge motion
<i>Mean.TwrBsFxt</i>	mean tower base shear force in the x direction
<i>Mean.TwrBsFyt</i>	mean tower base shear force in the y direction
<i>Mean.TwrBsFzt</i>	mean tower base shear force in the z direction
<i>Mean.TwrBsMxt</i>	mean tower base bending moment in the x direction
<i>Mean.TwrBsMyt</i>	mean tower base bending moment in the y direction
<i>Mean.TwrBsMzt</i>	mean tower base bending moment in the z direction
<i>Mean.RoThrust</i>	mean thrust force of the wind turbine rotor
MSL	mean sea level
RAO	response amplitude operator
<i>RAO<sub>11</sub></i>	response amplitude operator of surge motion
<i>RAO<sub>33</sub></i>	response amplitude operator of heave motion
<i>RAO<sub>55</sub></i>	response amplitude operator of pitch motion
RWT	reference wind turbine
<i>S<sub>11</sub></i>	power spectrum of surge motion response
<i>S<sub>33</sub></i>	power spectrum of heave motion response
<i>S<sub>55</sub></i>	power spectrum of pitch motion response
<i>S<sub>w</sub></i>	power spectrum of wave

$Th$	thickness
$T_p$	peak period of the wave spectrum
$U$	wind speed

### References in Chapter 3

- [1] Lee, C. H., and Newman, J. N., 2013, "WAMIT User Manual, Version 7.0," WAMIT Inc, Chestnut Hill, Massachusetts.
- [2] Jonkman, J. M., and Buhl, M. L. Jr., 2005, *FAST User's Guide – Updated August 2005*, NREL/TP-500-38230, 15020796.
- [3] Munbua, W., Hasan, M. S., Malta, E. B., Gonçalves, R. T., Fujiyama, C., and Maekawa, K., 2022, "Conceptual Design of a Prestressed Concrete Spar Floater Supporting a 10 Mw Offshore Wind Turbine," *International Conference on Ocean, Offshore and Arctic Engineering*, American Society of Mechanical Engineers, Hamburg, Germany.
- [4] Hopstad, A. L. H., Argyriadis, K., Manjock, A., Goldsmith, J., and Ronold, K. O., 2018, "DNV GL Standard for Floating Wind Turbines," *International Conference on Offshore Mechanics and Arctic Engineering*, American Society of Mechanical Engineers, p. V001T01A020.
- [5] Bortolotti, P., Tarres, H. C., Dykes, K., Merz, K., Sethuraman, L., Verelst, D., and Zahle, F., 2019, "IEA Wind TCP Task 37: Systems Engineering in Wind Energy – WP2.1 Reference Wind Turbines," p. 138.
- [6] Suzuki, H., Shiohara, H., Schnepf, A., Houtani, H., Carmo, L. H. S., Hirabayashi, S., Haneda, K., Chujo, T., Nihei, Y., Malta, E. B., and Gonçalves, R. T., 2020, "Wave and Wind Responses of a Very-Light FOWT with Guy-Wired-Supported Tower: Numerical and Experimental Studies," *JMSE*, **8**(11), p. 841.
- [7] Malta, E. B., 2019, "EdtoolsX User's Manual 2020."

- [8] Pesce, C. P., Amaral, G. A., and Franzini, G. R., 2018, "Mooring System Stiffness: A General Analytical Formulation with an Application to Floating Offshore Wind Turbines," *International Conference on Offshore Mechanics and Arctic Engineering*, American Society of Mechanical Engineers, p. V001T01A021.
- [9] Stansberg, C. T., Contento, G., Hong, S. W., Irani, M., Ishida, S., Mercier, R., Wang, Y., Wolfram, J., Chaplin, J., and Kriebel, D., 2002, "The Specialist Committee on Waves Final Report and Recommendations to the 23<sup>rd</sup> ITTC," *Proceedings of the 23<sup>rd</sup> ITTC*, **2**, pp. 505–551.
- [10] Ramachandran, G. K. V., Robertson, A., Jonkman, J. M., and Masciola, M. D., "Investigation of Response Amplitude Operators for Floating Offshore Wind Turbines: Preprint," p. 10.
- [11] Wenfei Xue, 2016, "Design, Numerical Modelling and Analysis of a Spar Floater Supporting the DTU 10MW Wind Turbine," M.S. thesis, Marine Technology, Norwegian University of Science and Technology.
- [12] Munbua, W., Hasan, M. S., Malta, E. B., Gonçalves, R. T., Fujiyama, C., and Maekawa, K., 2021, "Conceptual Design of a Spar Prestressed Concrete Floating Platform Supported 10 MW Offshore Wind Turbine," *JWEA 43<sup>rd</sup> Wind Energy Symposium*, Tokyo, Japan, p. 1.
- [13] Takata, T., Takaoka, M., Gonçalves, R. T., Houtani, H., Yoshimura, Y., Hara, K., Oh, S., Dotta, R., Malta, E. B., Iijima, K., and Suzuki, H., 2021, "Dynamic Behavior of a Flexible Multi-Column FOWT in Regular Waves," *JMSE*, **9**(2), p. 124.

## **CHAPTER 4**

### **MODEL TEST**

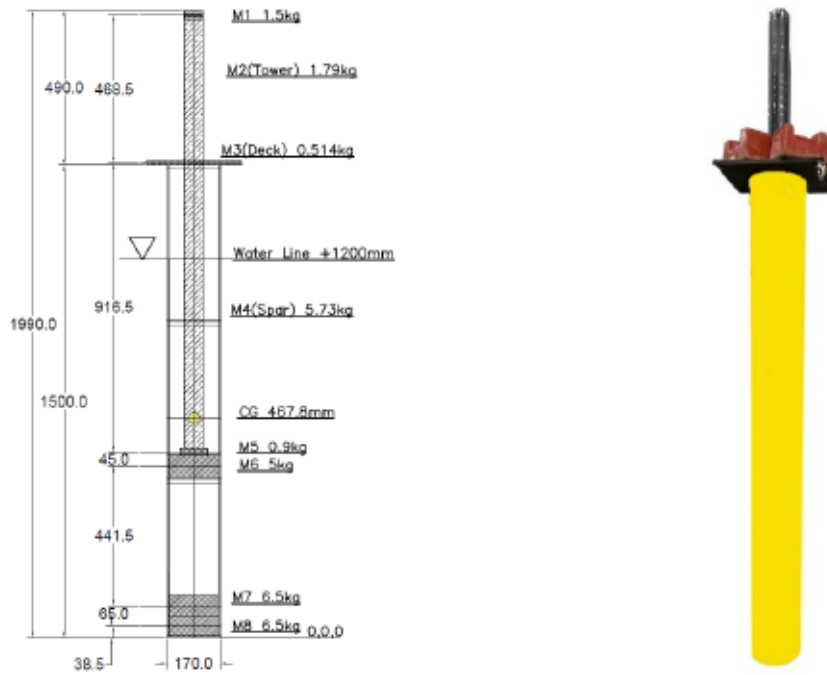
#### **4.1 Introduction**

The aim of this chapter is to investigate the hydrodynamic behavior of the proposed spar under wave action. One of the indicators to validate this behavior is the Response Amplitude Operators (RAOs), which is the response of the model to the wave, developed from model testing. In the experiment, the spar-scaled model 1:100 is excited by three wave conditions, and the response motions are captured. Once the time domain of the recorded waves and response motions are successfully converted to the frequency domain and presented in terms of the power spectrum, RAOs can be defined. Then RAOs of the experimental results and the simulation analysis can be compared. The experimental results are converted by applying Froude Scaling to represent the actual scale. The results show fairly good agreement with the numerical analysis in terms of the surge and heave motions; however, in pitch motion, the analysis shows higher RAO. The natural periods of the model obtained from the experiment are beyond the range of the waves, confirmed the model can avoid resonance phenomena induced by wave excitation. The results are consistent with the full-scale analysis.

#### **4.2 Experiment Setup**

##### **4.2.1 Reduced Scale Model**

The model designed for the experiment is 1/100 of the full-scale analysis model, which is represented a long draft spar floater, as shown in Figure 4.1a, and the reduced scale model is shown in Figure 4.1b. The Froude Scaling [1] is applied to this experiment (Table 4.1). It is the most commonly used in the water wave problem because inertia is the most predominant force in the system. The Froude law considers the effect of gravity on the system and contains the gravitational acceleration term, which can be defined as the ratio of inertia to gravitational force developed on an element submerged in fluid [1]. The main dimensions and properties of the floater are shown in Tables 4.2 and 4.3, respectively.



(a) The main dimension of the scale model [mm]      (b) A figure of the reduced scale model

**FIGURE 4.1:** Main dimensions and mass distribution of the scale model

**TABLE 4.1:** Scale factors using Froude Scaling

Characteristic	Scale Factor	Characteristic	Scale Factor
Length [m]	$\lambda$	Mass [kg]	$\lambda^3$
Time [s]	$\lambda^{1/2}$	Natural period [s]	$\lambda^{1/2}$
Force [N]	$\lambda^3$		

**TABLE 4.2:** Main dimensions of the floater

Dimension	Prototype Full Scale	Model Scale (1/100)
Draft	120 [m]	1200 mm
Diameter	17 [m]	1700 mm
Hull Thickness	0.6 [m]	600 mm



**TABLE 4.3:** Main properties of the floater

Property	Prototype Full Scale	Model Scale (1/100)
Structural mass	26,965 [ton]	27.1 [kg]
Water Displacement	27,227 [ton]	27.1 [kg]
Water Line	120 [m]	1200 [mm]
CG	51.53 [m]	467.8 [mm]
CB	60.04 [m]	582.6 [mm]
GM	8.66 [m]	116.3 [mm]

#### 4.2.2 Wave Tank Setup

The experiments are performed in a towing tank at the University of Tokyo. The dimension of the tank is 85.0m x 3.5m x 2.4 m (length x width x depth). The model is installed around 50 m. away from the wave generator [2]. Four horizontal moorings composed of wires and springs are attached to the model to keep it in position and prevent it from drifting. Details of the experimental setup are shown in Figure 4.2.

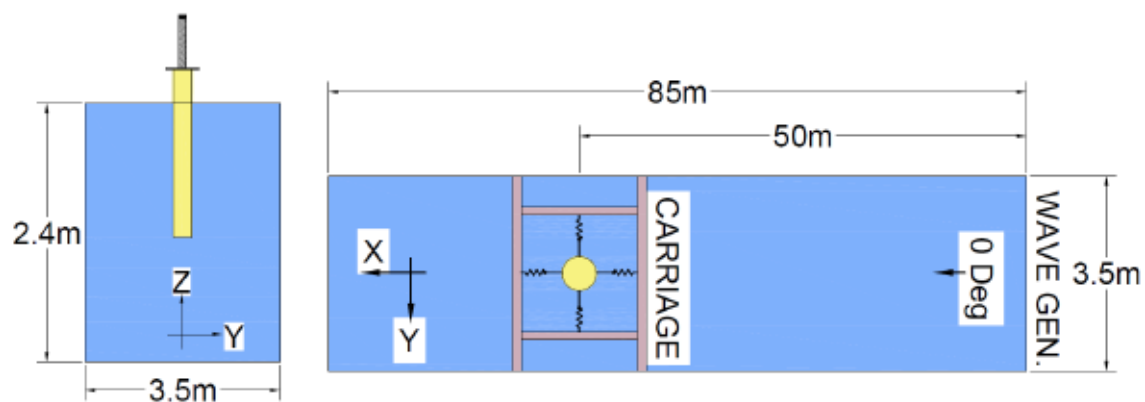


**FIGURE 4.2:** Experiment setup and towing tank dimension

In the wave experiment, the six-degree-of-freedom (DOFs) motions of the model and the incident wave are measured. The 6DOFs rigid body motions of the model are defined as the motion of the center of gravity. The floating body motions are captured by the Qualysis® Optical Motion Capture System, having four cameras. The wave probe is installed between the wave generator and the experimental model [2].

### 4.2.3 Environmental Conditions

Experiments under irregular waves are conducted under three different wave conditions, operational, storm, and centenary. Each wave is performed in three wave signals. In the case of storm conditions, which proceed highest wave energy, the wave height is reduced to 8 cm. to avoid the influence of wave reflection due to the limitation of the towing tank. The peak periods  $T_p$  and significant wave height  $H_s$  of each wave condition are shown in Table 4.4. The ISSC spectra of the prototype full-scale wave and model-scale are shown in Figure 4.3 [3].

**TABLE 4.4:** Irregular wave in full-scaled analysis and the model test

Conditions	Significant Wave Heights ( $H_s$ )		Peak Period ( $T_p$ )	
	Prototype Full Scale	Model Scale (1/100)	Prototype Full Scale	Model Scale (1/100)
Operational	2.5 [m]	2.5 [cm]	9.0 [s]	0.90 [s]
Storm	9.6 [m]	8.0 [cm]	13.5 [s]	1.35 [s]
Centenary	4.0 [m]	4.0 [cm]	16.1 [s]	1.61 [s]

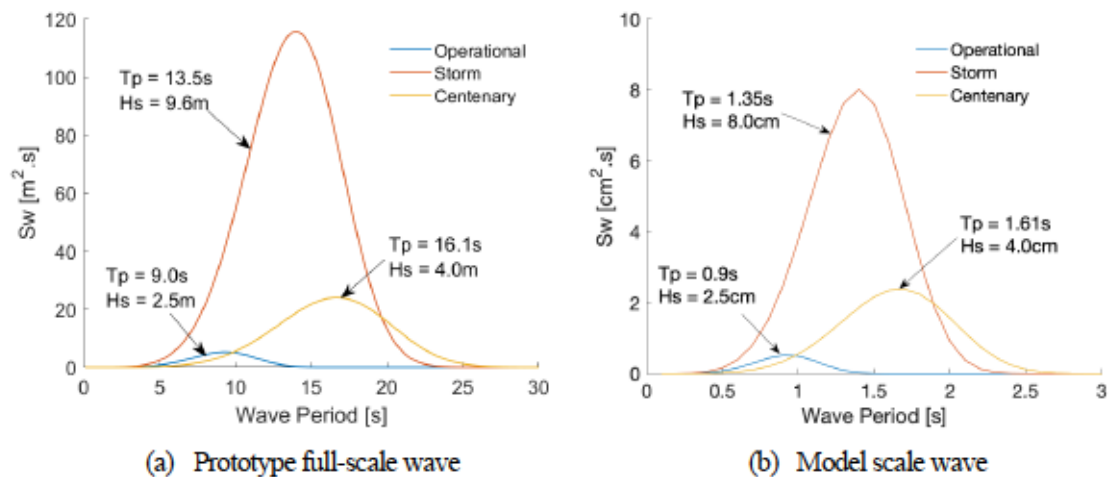


**FIGURE 4.3:** Prototype full-scale wave and model-scale wave

The recorded wave amplitude in the time domain and the conversion to the frequency domain of the irregular waves performed in the experiment are shown in Figures 4.4 to 4.6. We can observe that the

operational wave proceeds the most energy between 0.5 Hz and 2.5 Hz., the storm wave has the most energy between 0.5 Hz and 2.0 Hz, and the centenary wave also has the most energy between 0.5 Hz and 2.0 Hz, as shown in Figures 4.4b to 4.6b respectively.

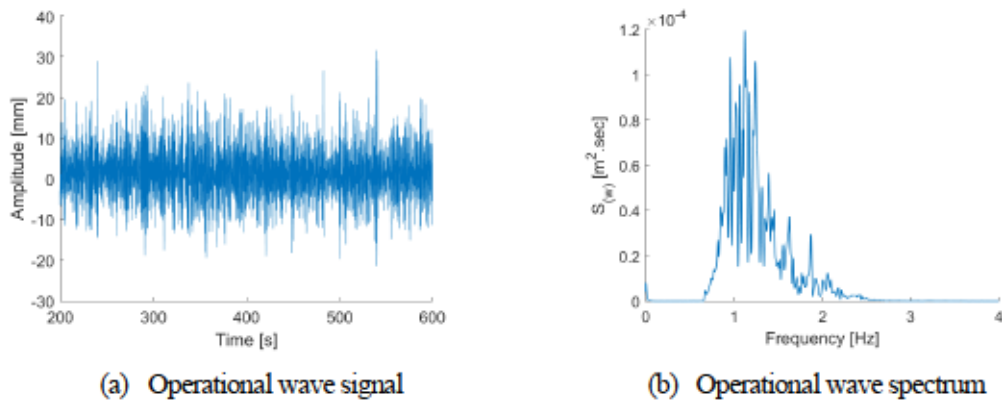


**FIGURE 4.4:** Operational wave's signal and spectrum

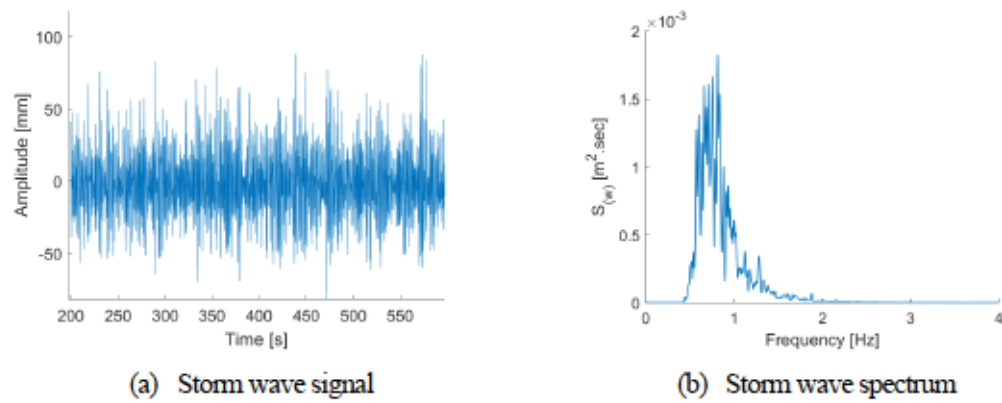


**FIGURE 4.5:** Storm wave's signal and spectrum

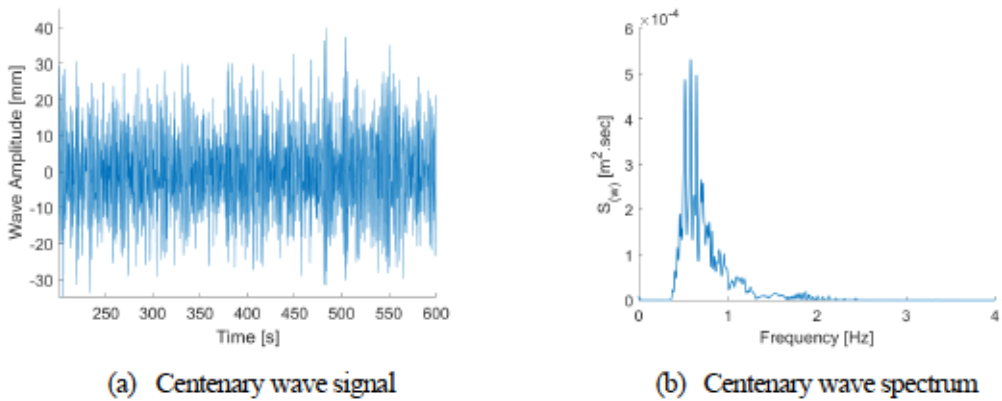


**FIGURE 4.6:** Centenary wave's signal and spectrum

### 4.3 Response Motion of the Model

Two main experiments are conducted for the spar model test, the first is a free vibration test without waves to define the natural frequency of the model. Second is the experiment with waves to observe the response of the model under wave action.

#### 4.3.1 Free Vibration Tests

The goal of the free vibration test is to define the natural frequency of the model in the condition without waves. Here, the initial forces are given to the model in 6DOFs, which are surge, sway, heave, roll, pitch, and yaw motions. The model responds largely at first when the initial forces are given and gradually stop, as can be observed in Figure 4.7a to 4.12a; then the process is repeated again for few times. The motion responses in the time domain are captured, shown in Figures 4.7a to 4.12a, and later they are converted to the frequency domain presented in Figures 4.7b to 4.12b.

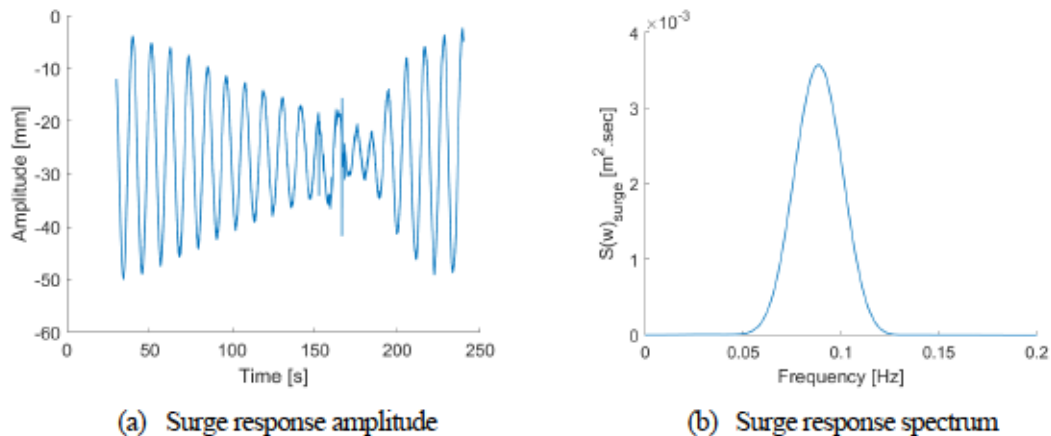
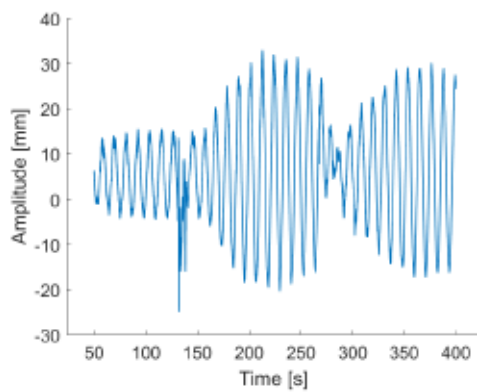
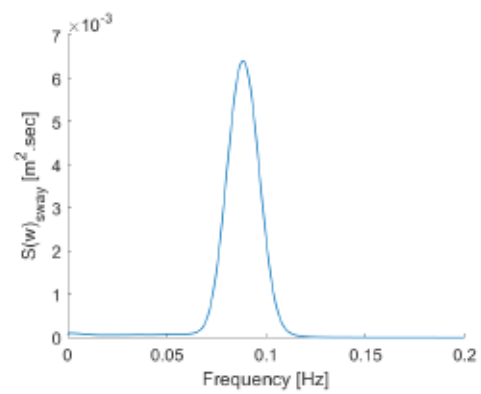


**FIGURE 4.7:** Surge motion response obtained from free vibration test

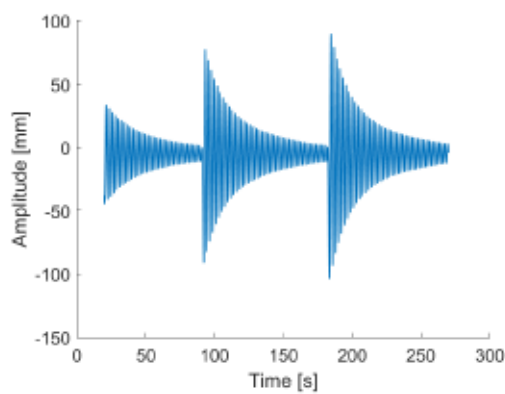


(a) Sway response amplitude

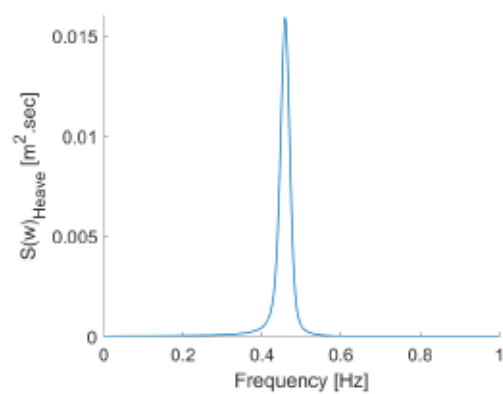


(b) Sway response spectrum

**FIGURE 4.8:** Sway motion response obtained from free vibration test

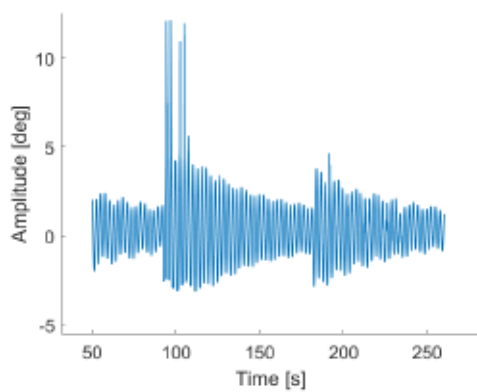


(a) Heave response amplitude

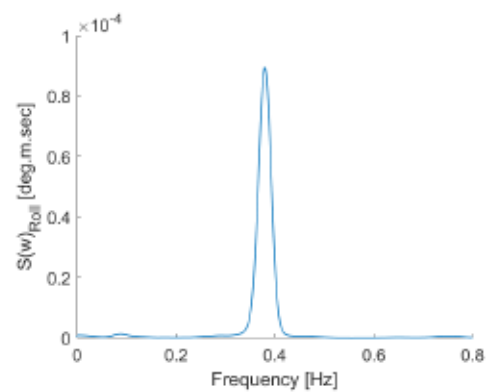


(b) Heave response spectrum

**FIGURE 4.9:** Heave motion response obtained from free vibration test



(a) Roll response amplitude



(b) Roll response spectrum

**FIGURE 4.10:** Roll motion response obtained from free vibration test

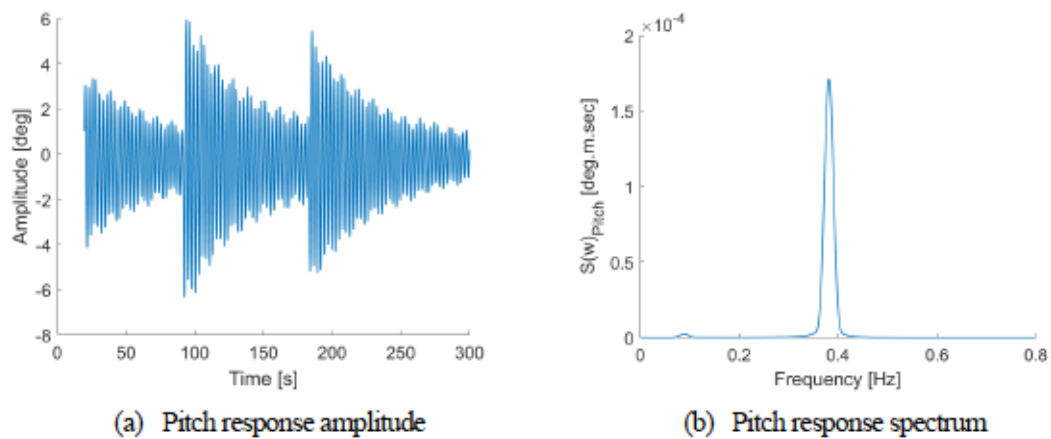


**FIGURE 4.11:** Pitch motion response obtained from free vibration test

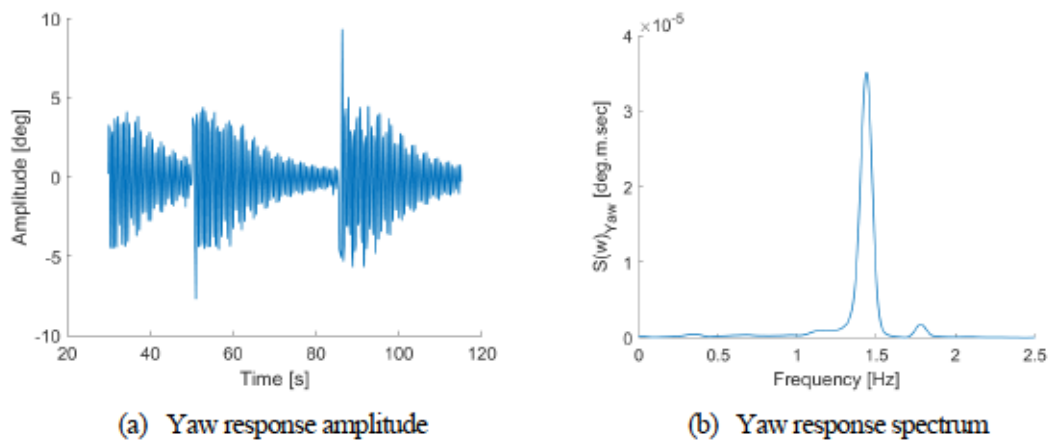


**FIGURE 4.12:** Yaw motion response obtained from free vibration test

Here, we can observe very small peaks in some range of frequencies, but the highest peaks are clear to be seen (Figures 4.7b to 4.12b). In the free vibration test without waves, the response energy of the structure is not disturbed by the wave energy, the response represents the structural response itself; therefore, a clear peak is expected to be observed in each motion. The natural frequency of each DOFs can be defined at the highest peak of the response spectrum, which means a specific range of frequency that the structure will respond largest. When  $\omega_n$  is the natural frequency of the structure unit Hz, the natural period can be defined by

$$T_n = \frac{1}{\omega_n} \quad (4-1)$$

The natural frequency and the natural period of the model scale obtained from the free vibration test are shown in Table 4.5.

**TABLE 4.5:** Natural periods obtained from the free vibration test

Degree of Freedom	Natural Frequency $\omega_n$ [Hz]	Natural Period $T_n$ [s]
Surge	0.088	11.35
Sway	0.089	11.29
Heave	0.459	2.18
Roll	0.379	2.64
Pitch	0.382	2.62
Yaw	1.429	0.70

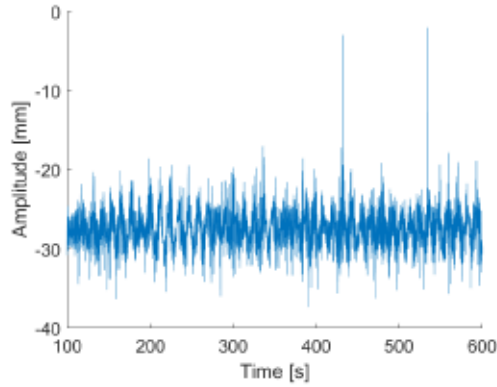
### 4.3.2 Experiments with Waves

The goal of the experiment with waves is not only to define the RAOs, but also to confirm the natural period of the structure; and to access the resonance phenomena that must be avoided. The motion responses in the time domain of the experiment with wave are captured and converted to the frequency domain presented in Figures 4.13 to 4.30. Unlike the free vibration test, the response spectra of the model under wave action show several peaks attributed to wave energies disturbing (Figure 4.13b to 4.30b). However, the highest peak of the response spectrum, which means the natural frequency of each DOF of the model, can be clearly observed particularly in surge, heave, pitch and yaw motions. The natural periods of the structure under wave actions, computed from Equation 4-1, are shown in Table 4.6.

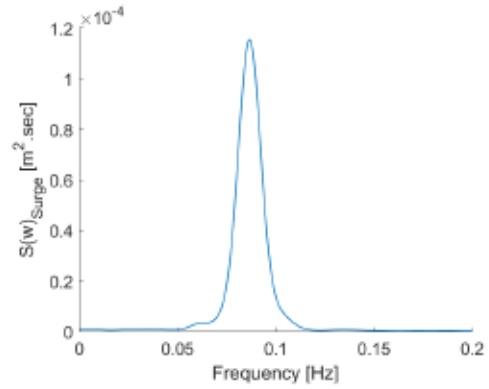
**TABLE 4.6:** The peak period obtained from the experiment with wave

Degree of Freedom	Peak Period $T_p$ [s]		
	Operational	Storm	Centenary
Surge	11.56	11.36	11.69
Sway	12.12	11.62	11.76
Heave	2.17	2.16	2.16
Roll	0.89	1.95	2.65
Pitch	2.64	2.62	2.63
Yaw	0.69	0.69	0.69

## Operational Wave

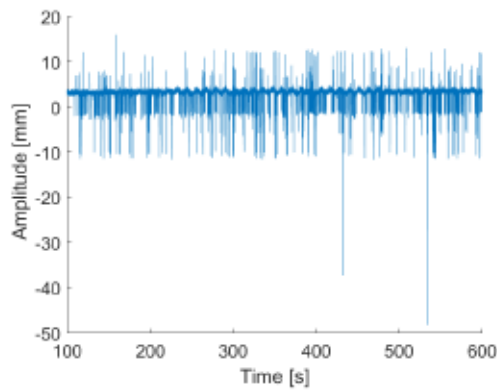


(a) Response amplitude

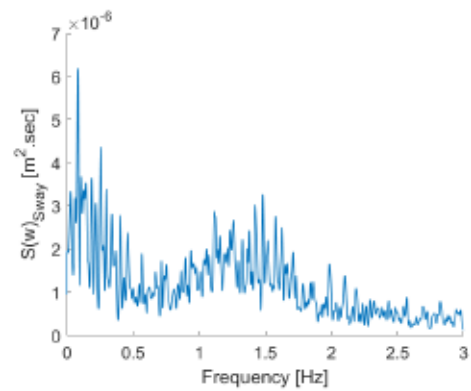


(b) Response spectrum

**FIGURE 4.13:** Surge motion response obtained from operational wave

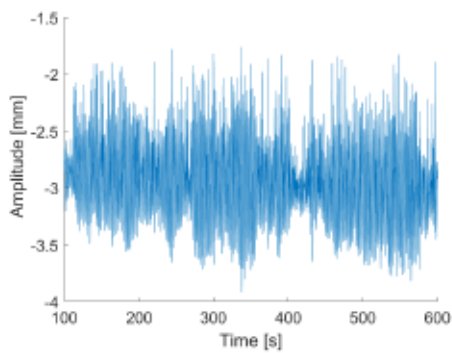


(a) Response amplitude

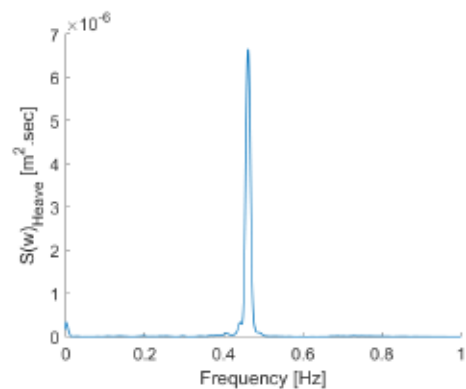


(b) Response spectrum

**FIGURE 4.14:** Sway motion response obtained from operational wave



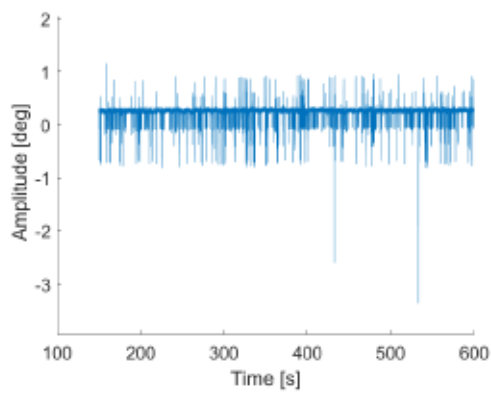
(a) Response amplitude



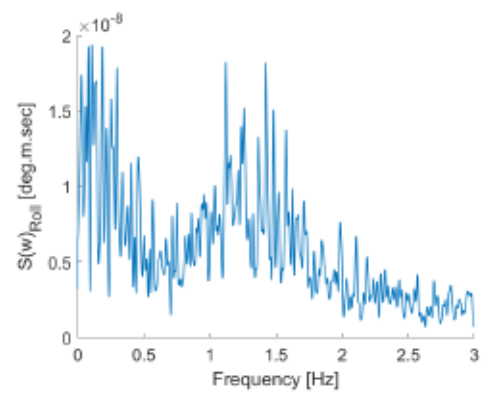
(b) Response spectrum

**FIGURE 4.15:** Heave motion response obtained from operational wave



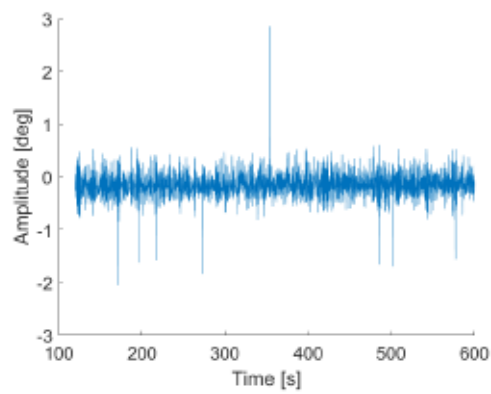


(a) Response amplitude

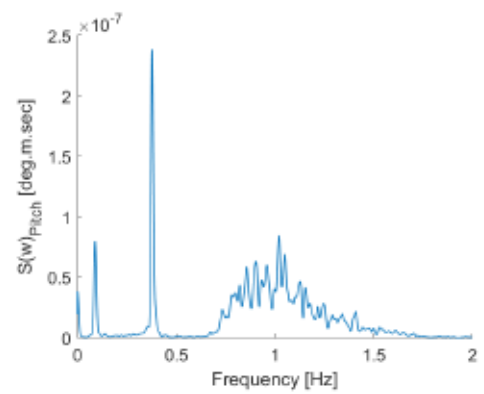


(b) Response spectrum

**FIGURE 4.16:** Roll motion response obtained from operational wave

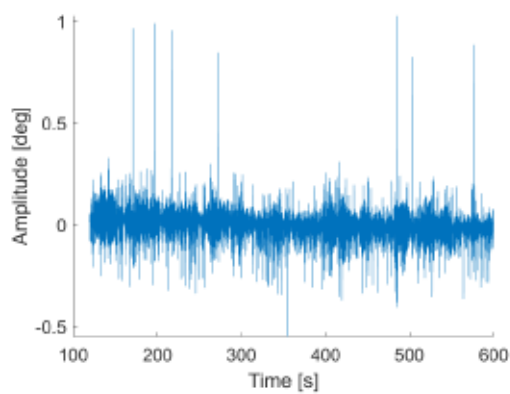


(a) Response amplitude

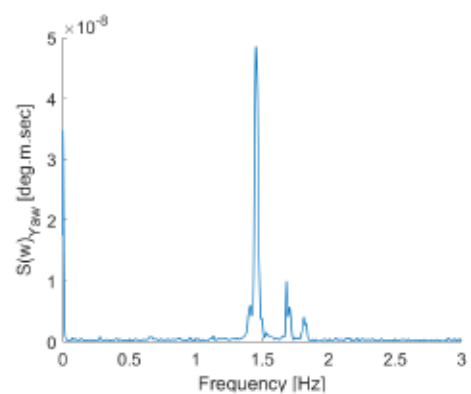


(b) Response spectrum

**FIGURE 4.17:** Pitch motion response obtained from operational wave



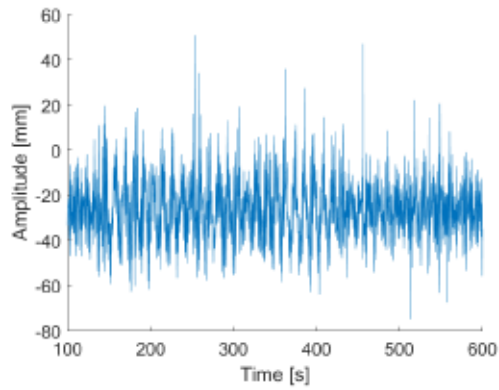
(a) Response amplitude



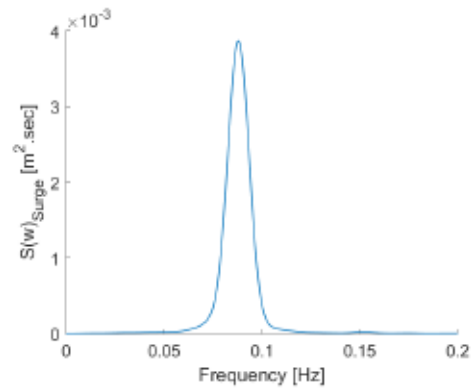
(b) Response spectrum

**FIGURE 4.18:** Yaw motion response obtained from operational wave

**Storm wave**

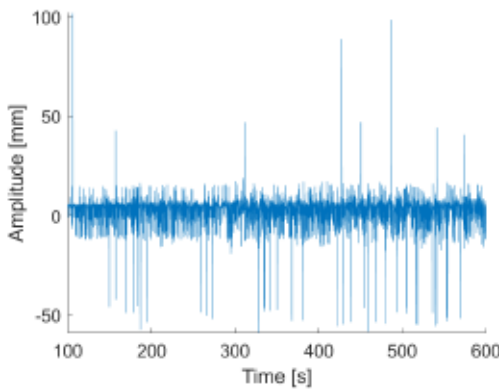


(a) Response amplitude

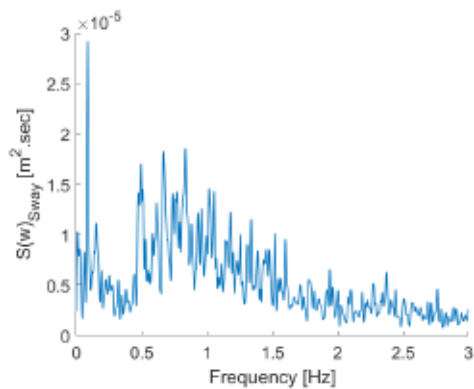


(b) Response spectrum

**FIGURE 4.19:** Surge motion response obtained from storm wave

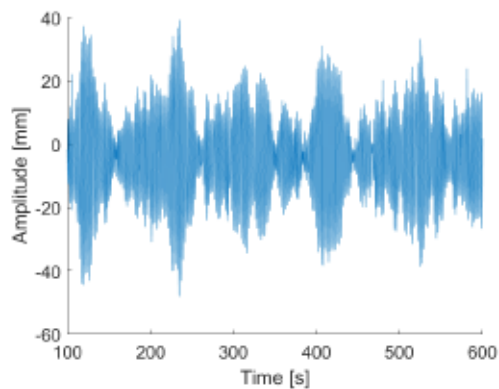


(a) Response amplitude

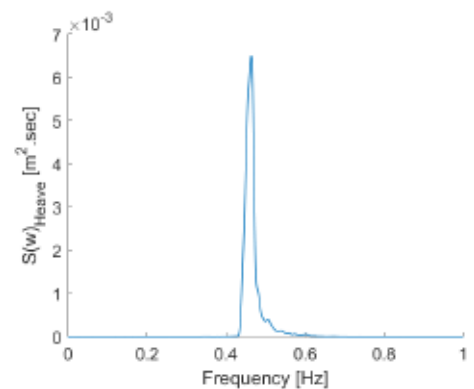


(b) Response spectrum

**FIGURE 4.20:** Sway motion response obtained from storm wave

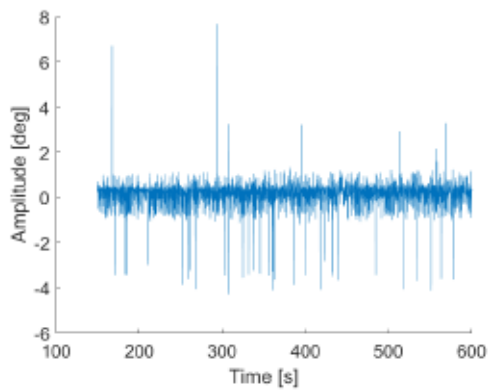


(a) Response amplitude

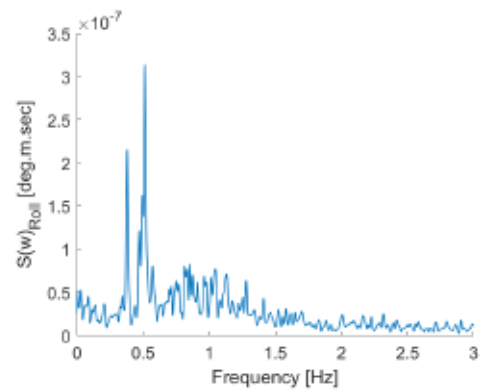


(b) Response spectrum

**FIGURE 4.21:** Heave motion response obtained from storm wave

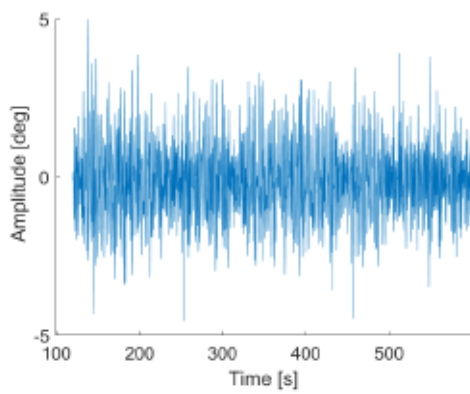


(a) Response amplitude

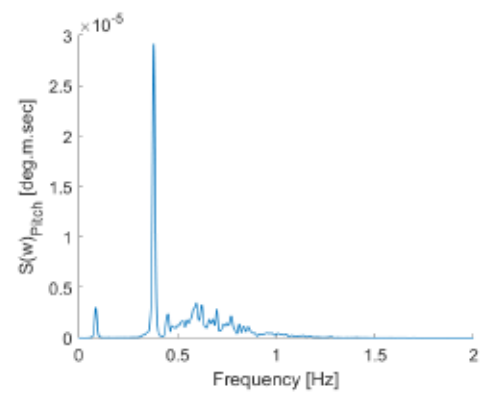


(b) Response spectrum

**FIGURE 4.22:** Roll motion response obtained from storm wave

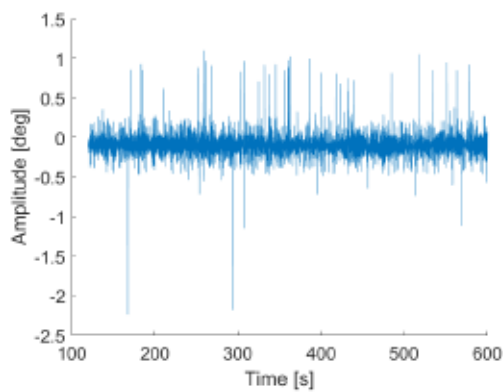


(a) Response amplitude

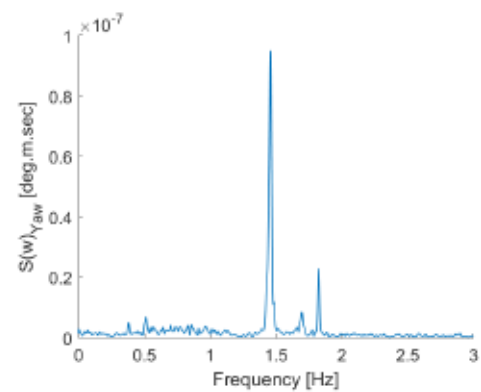


(b) Response spectrum

**FIGURE 4.23:** Pitch motion response obtained from storm wave



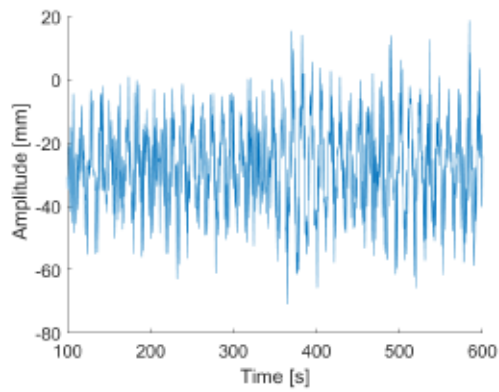
(a) Response amplitude



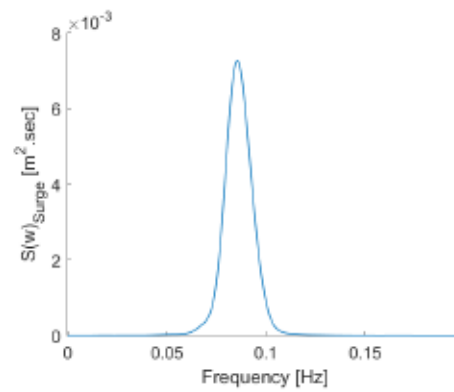
(b) Response spectrum

**FIGURE 4.24:** Yaw motion response obtained from storm wave

### Centenary wave

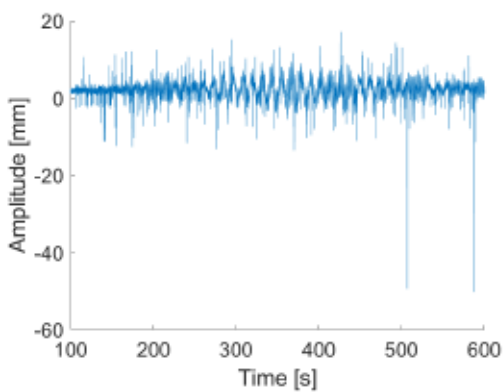


(a) Response amplitude

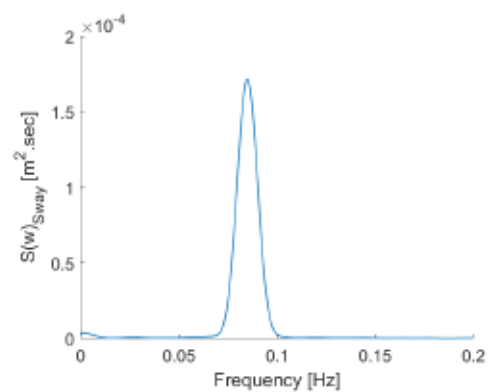


(b) Response spectrum

**FIGURE 4.25:** Surge motion response obtained from centenary wave

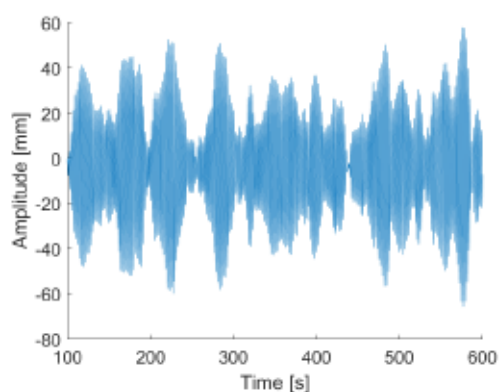


(a) Response amplitude

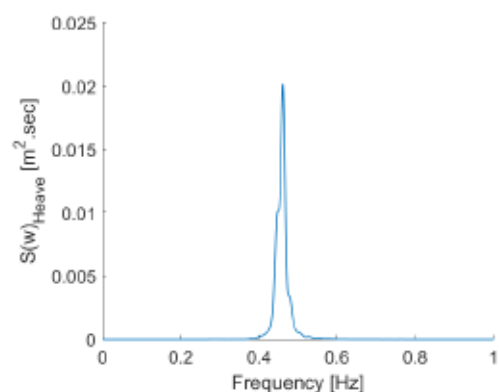


(b) Response spectrum

**FIGURE 4.26:** Sway motion response obtained from centenary wave



(a) Response amplitude



(b) Response spectrum

**FIGURE 4.27:** Heave motion response obtained centenary wave

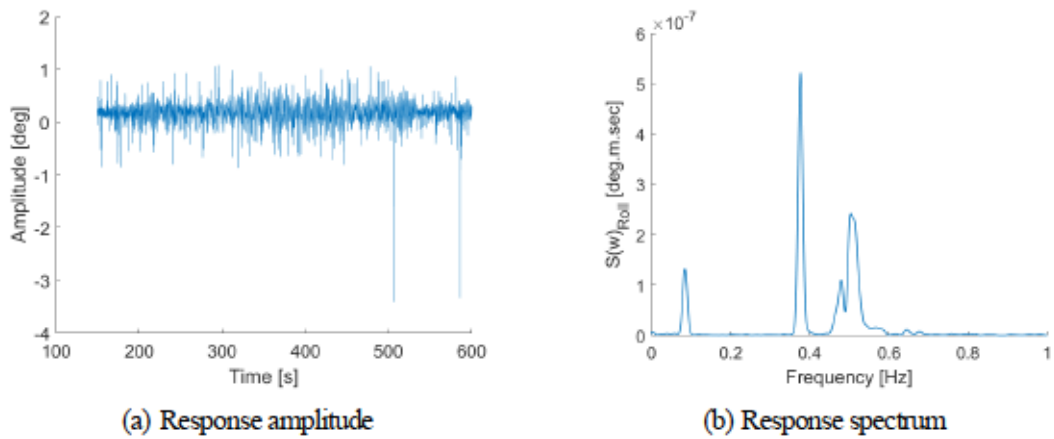


**FIGURE 4.28:** Roll motion response obtained centenary wave

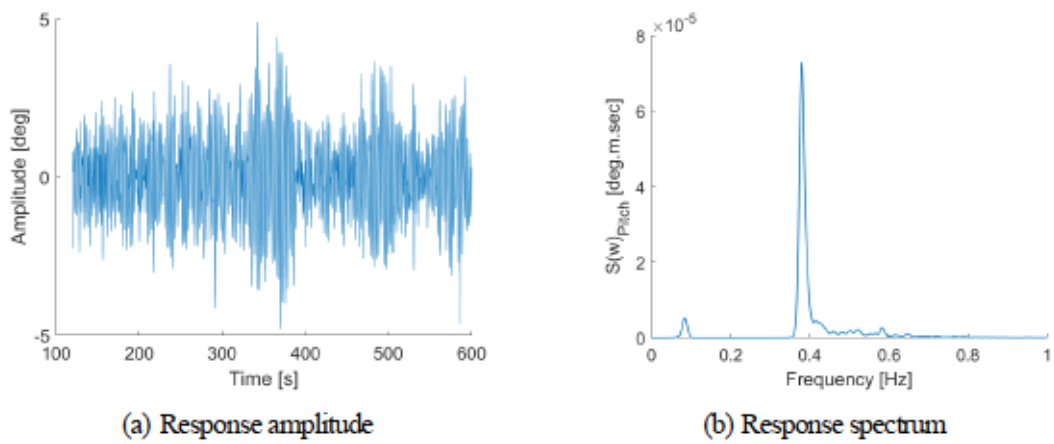


**FIGURE 4.29:** Pitch motion response obtained centenary wave

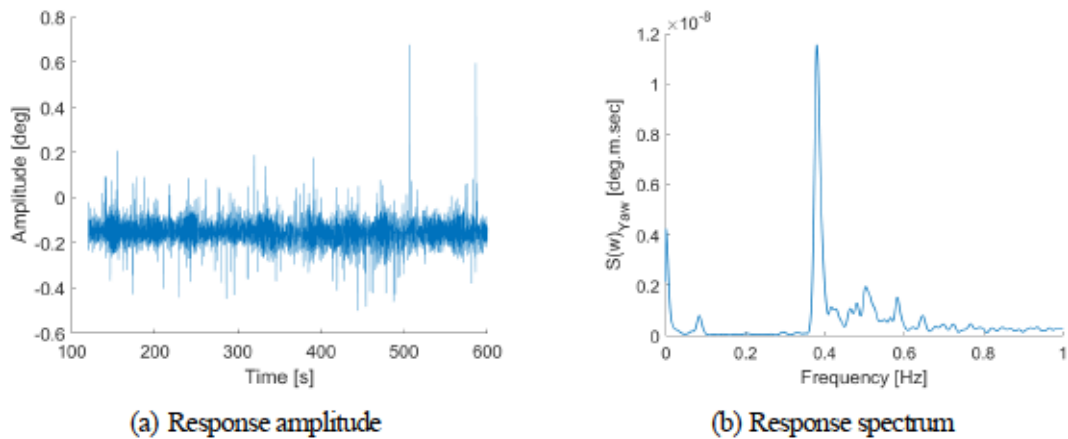


**FIGURE 4.30:** Yaw motion response obtained centenary wave

In Figures 4.13b to 4.30b, we can observe a first peak occurred at very low-frequency ranges (for example, Figure 4.30b), particularly in sway, roll, pitch, and yaw which are the low responses motions. However, it doesn't occur in the high response such as surge and heave motions. This is supposed to be the effect of mooring springs installed to protect the model from drifting. Therefore, the natural periods shown in Table 4.6 has not considered this first peak.

To confirm the structure's natural period, the comparison between responses under the free vibration test and the experiment with waves are compared and shown in Table 4.7. It can be noticed that the natural periods obtained from the free vibration test are close to the experiment with waves, except for the roll motion, which shows the different natural periods in each wave condition. However, for a cylindrical spar, we can observe the low response motions in sway, yaw, and roll (Figures 4.13b to 4.30b). The RAOs of sway, yaw, and roll motions are also almost zero (Section 4.3.3); therefore, the sway, yaw, and roll motions are not significant for a cylindrical symmetrical shape spar and are possible to be neglected in the motion analysis.

Compared with the period  $T_p$  of the waves (operational 0.9s, storm 1.35s, and centenary 1.61s from Figure 4.3b), the natural periods of the model scale shown in Table 4.7 are beyond the range of the waves. Therefore, it can avoid any structural resonance induced by wave excitation.

**TABLE 4.7:** Comparison of natural periods between free vibration and wave tests

DOFs	Free Vibration Test [s]	Experiment with Waves [s]		
		Operational	Storm	Centenary
Surge	11.35	11.56	11.36	11.69
Sway	11.29	12.12	11.62	11.76
Heave	2.18	2.17	2.16	2.16
Roll	2.64	0.89	1.95	2.65
Pitch	2.62	2.64	2.62	2.63
Yaw	0.70	0.69	0.69	0.69

### 4.3.3 Comparison of the Response Amplitude Operators (RAOs)

One goal of model testing is to develop the Response Amplitude Operators or RAOs, which is the magnitude of the linear transfer function  $H(\omega)$  between force function and response function [1], in other words, it is the response of the model to the wave. When the time domain of the recorded waves and response is converted to the frequency domain, the RAOs can be defined as

$$|H(\omega)|^2 = |RAO(\omega)|^2 = S_{yy}(\omega)/S_{xx}(\omega) \quad (4-2)$$

where the  $S_{xx}(\omega)$  is the autospectral energy density spectrum of the wave shown in Figures 4.4b to 4.6b, and  $S_{yy}(\omega)$  is the corresponding spectral density function of the responses, shown in Figures 4.13b to 4.30b. The plot of RAOs results limited the x-axis at the most energy range of each wave condition, are shown in Figures 4.31 to 4.33. (The RAOs in sway, roll, and yaw are found to be zero, which are not presented here).

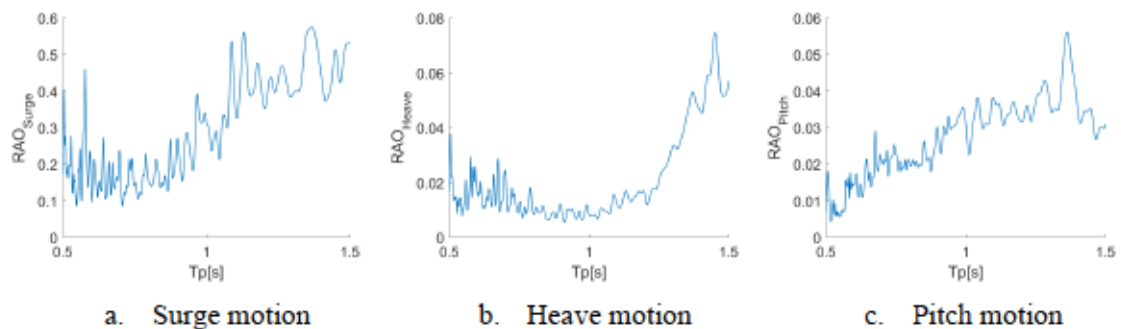


**FIGURE 4.31:** RAOs of the operational wave

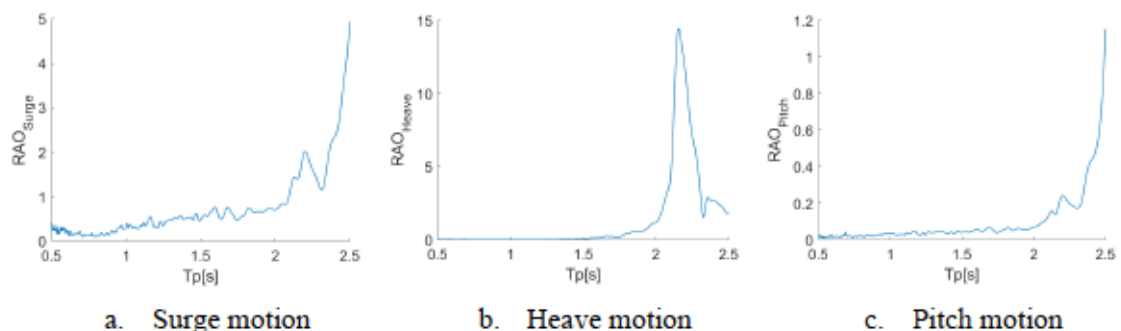


**FIGURE 4.32:** RAOs of the storm wave

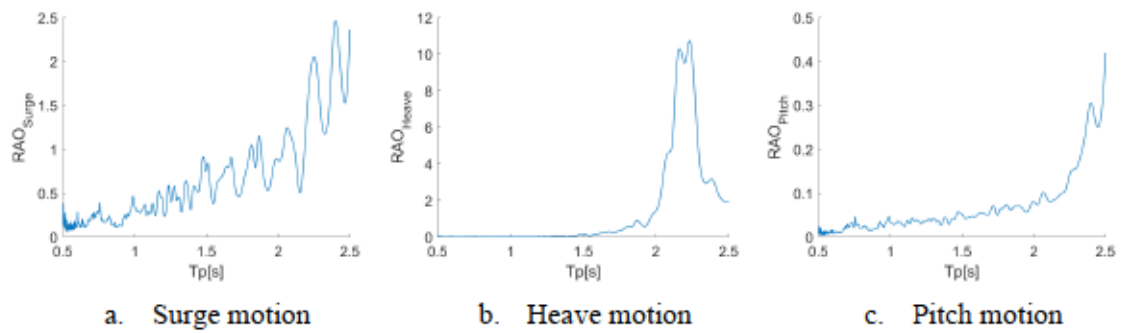


**FIGURE 4.33:** RAOs of the centenary wave

By applying Froude Scaling, the experimental results can be converted to the actual scale, then RAOs of the experimental and the theoretical results can be compared. The RAOs is the linear transfer function, and it is nondimensional; therefore, only the period  $Tp$  is converted to the actual scale using the scale factor shown in Table 4.1. The comparison of the RAOs between analytical results using numerical code WAMIT and the experimental results show in Figures 4.34 to 4.36. In numerical analysis, viscous damping is linearized; therefore, it returns the linear RAOs shown in the WAMIT results. On the other hand, viscous damping of the real fluid flow can be nonlinear; thus, we can observe the fluctuated line in the experimental results.

Figures 4.34 to 4.36 show good consistency trends between WAMIT and the experiment, particularly in terms of the surge and heave motions; however, numerical results show higher responses for the pitch motion which needs more investigation. Regarding the trend of the responses, these findings are consistent with the full-scale analysis in Chapter 3.

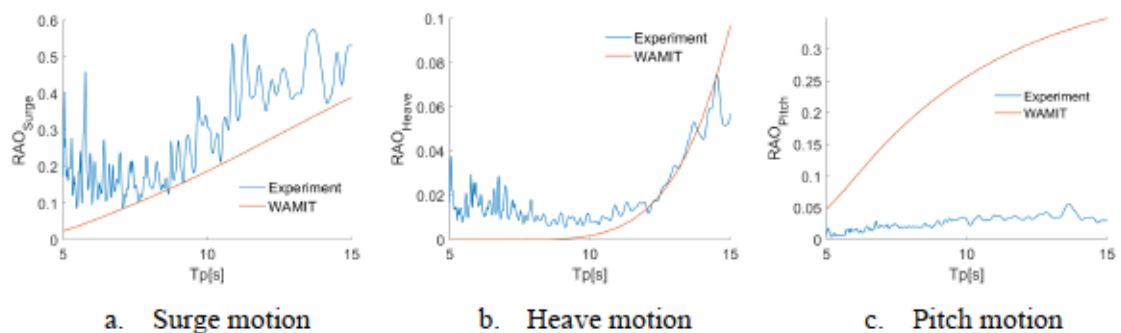


**FIGURE 4.34:** RAOs comparison of the operational wave



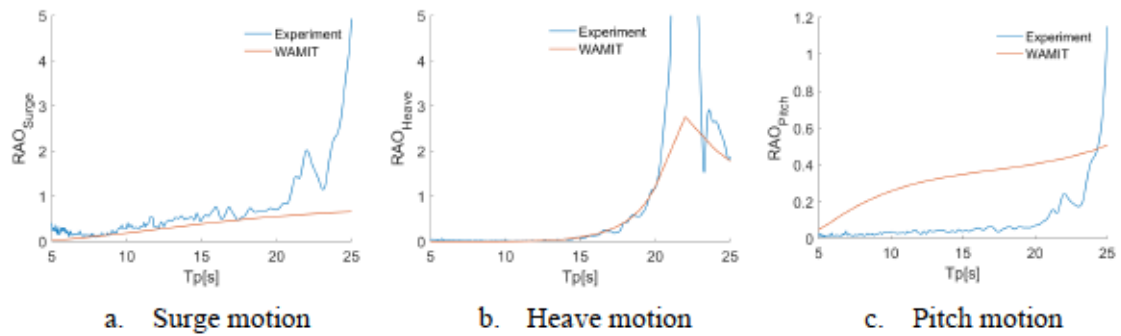


**FIGURE 4.35:** RAOs comparison of the storm wave

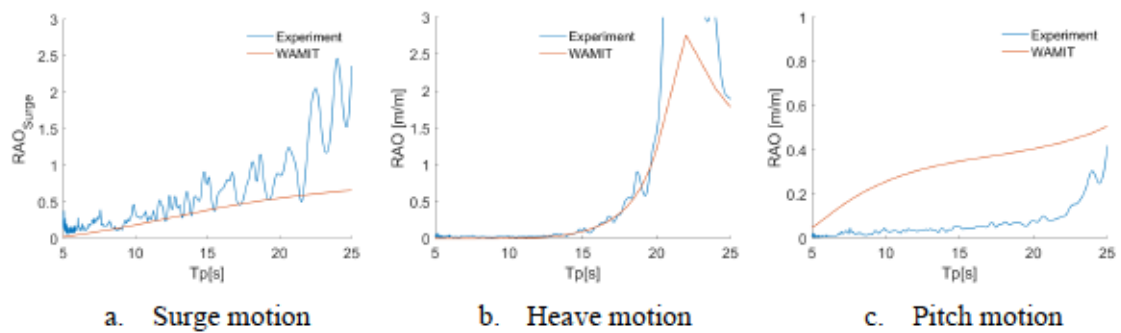


**FIGURE 4.36:** RAOs comparison of the centenary wave

Considering the larger pitch motion of the numerical analysis using WAMIT compared to the experimental results, three sources of the cause could be possible: the difference in inertia, viscous damping, and hydrodynamic added mass (Equation 2-33). The inertia force is computed based on the platform's mass and moment of inertia of waterplane area; therefore, for a cylindrical shape spar that is symmetric in  $x - y$  axes, it is supposed to be linear and constant. However, viscous damping and the hydrodynamic added mass of the rigid body under the real fluid flow can differ from the theoretical analysis. The lower responses of the experimental results may imply that there is higher damping in the actual fluid flow or there is higher hydrodynamic added mass in the numerical analysis model. Pitch motion should be investigated more in future studies.

#### **4.4 Conclusion for Chapter 4**

The experiment with waves of a spar-scaled model 1:100 is performed in the towing tank. The response motions are captured to confirm the hydrodynamic model under wave actions. Based on the experimental results, the following conclusions have been obtained.

1. It is observed that mooring springs installed to protect the model from drifting may affect the response motions, particularly in the low response such as roll, pitch, and yaw motions, as can be observed in the occurrence of a first peak at near-zero frequencies of the response spectrum.
2. The natural periods in 6DOFs obtained from the free vibration test are close to the experiment with waves (except for the roll motion). Therefore, the natural periods' range of the structure is confirmed.
3. The RAOs in the sway, roll, and yaw of the spar are found to be zeroes; therefore, the sway, yaw, and roll motions are not significant for a cylindrical symmetrical shape spar and are possible to be neglected in the motion analysis.
4. The RAOs comparison of the experiment and analytical analysis shows fairly good agreement in terms of the surge and heave motions; however, the analytical results show higher responses in pitch motion.
5. The difference in the pitch response between analytical and experimental results is supposed to cause by viscous damping and hydrodynamic added mass. The higher viscous damping is expected in the real fluid flow, or in another case, it has higher hydrodynamic added mass in the numerical analysis model.
6. The results show the natural periods of the scale model are away from input waves; therefore, it can avoid structural resonance induced by wave excitation.
7. The results obtained from the model test are consistent with the full-scale analysis; therefore, the hydrodynamic model is confirmed.

### Nomenclature in Chapter 4

CG	center of gravity
CB	center of buoyancy
DOF	degree of freedom
GM	metacentric height
$H_s$	significant wave height
$H(\omega)$	linear transfer function
M1	mass number 1 (plate 1.5 kg)
M2	mass number 2 (tower 1.79 kg)
M3	mass number 3 (deck 0.514 kg)
M4	mass number 4 (spar model 5.73 kg)
M5	mass number 5 (plate 0.9 kg)
M6	mass number 6 (plate 5 kg)
M7	mass number 7 (plate 6.5 kg)
M8	mass number 8 (plate 6.5 kg)
RAO	response amplitude operator
$S_{xx}(\omega)$	the autospectral energy density spectrum
$S_{yy}(\omega)$	the corresponding spectral density function of the responses
$T_p$	peak period of the wave spectrum
$T_n$	the natural period
$\omega_n$	the natural frequency
$\lambda$	scale factor

### References in Chapter 4

- [1] Chakrabarti, S. K., 1994, *Offshore Structure Modeling*, World Scientific, Singapore ;  
River Edge, NJ.

- [2] Takata, T., Takaoka, M., Gonçalves, R. T., Houtani, H., Yoshimura, Y., Hara, K., Oh, S., Dotta, R., Malta, E. B., Iijima, K., and Suzuki, H., 2021, "Dynamic Behavior of a Flexible Multi-Column FOWT in Regular Waves," *JMSE*, **9**(2), p. 124.
- [3] Munbua, W., Hasan, M. S., Malta, E. B., Gonçalves, R. T., Fujiyama, C., and Maekawa, K., 2022, "Conceptual Design of a Prestressed Concrete Spar Floater Supporting a 10 Mw Offshore Wind Turbine," *International Conference on Ocean, Offshore and Arctic Engineering*, American Society of Mechanical Engineers, Hamburg, Germany.

## CHAPTER 5

### CONCRETE FINITE ELEMENT ANALYSIS AND STRUCTURAL DESIGN

#### 5.1 Introduction

This chapter aims to investigate the non-linear behavior of the proposed concrete spar floater supporting a 10MW floating offshore wind turbine and design structural concrete. The forces at the tower base and fairlead position are taken from the most dominant case of the couple dynamic analysis performed by OpenFAST, mentioned in Chapter 3. The predominant hydrodynamic pressure applied on the spar surface is taken from WAMIT. Finally, numerical analysis performed by Finite Element Code COM3 is utilized to capture the stress and strain distribution and design structural concrete.

#### 5.2 Finite Element Model

In this research, the Finite Element Code COM3, Concrete Model for 3Dimensional problems developed by Maekawa et al. [1], is utilized to conduct non-linear behavior assessments of the prestressed concrete spar. The constitutive models implemented in COM3 were developed for the specific path-dependent nonlinearity of reinforced concrete, mainly attributed to cracking, reinforcement plasticity, and bond interaction between concrete and reinforcement [1]. After the concrete crack, the stress mechanism becomes anisotropic in the crack direction. The constitutive laws of cracked concrete are presumed to comprise stress transfer parallel to the crack axis, stress transfer normal to the crack axis, and shear transfer along the crack, which can be derived from a strain developed in the RC element.

The FE model's mesh size of the proposed spar concrete is determined based on the function of each part to ensure the FE analysis captures the system behavior while minimizing the solution time. The COM3 convergence index order is set between 0.1%–1% or less than 3% of the total number of Gauss points in the non-linear event [2]. The final FE model is composed of 35,420 elements and 44,029 nodes. The minimum steel mesh size is set to 3.8 x 4.0 x 70 cm to capture the effects of high-stress localization in these parts; the mesh is set to various larger sizes for the

concrete parts, with a maximum size of 120 x120 x 200 cm. Figure 5.1 shows COM3 FE model mesh details.

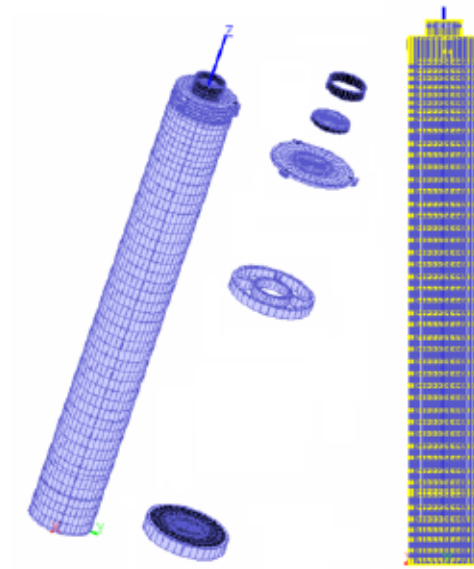


**FIGURE 5.1:** COM3 FE model mesh details

### **5.3 Material and Boundary Condition**

The conceptual design developed in this study is based on a normal concrete compressive strength of 41 MPa. The reinforcing bar Class SD40 with a yield strength of 390 MPa and a tensile strength of 560 MPa, is employed in the design. The reinforcement ratio is approximated using the initial design estimation considering the requirements of each part [3]. A reinforcement ratio of 0.1% is applied in all directions for the tower and fairlead connections. The reinforcement ratio of 0.7 % is applied in the x-direction and y-direction and 1.4% in the z-direction for the concrete hull to represent the prestressing tendons investigating stress-strain distribution at the beginning of FE analysis. Steel material class S355 with a yield strength of 355 MPa as defined in the European standard DIN EN 10025-2 [4] is applied to the steel tower and preliminary designed steel connection systems. Table 5.1 lists the concrete and steel materials utilized in the FE model.

The bond interface between concrete and steel material is modeled by the bond element under Mohr-Coulomb's frictional law with a frictional coefficient  $\mu$  of 0.6. In other words, a bond element is a thin element that transfers the force between two materials through the fictional force without any deformation; therefore, the stiffness of the bond element can be large to prevent any deformation. The bond element properties adopted on the contact surface are shown in Table 5.2.

The diameter of 15 mm of low-relaxation seven-wire strand class 270, with a tensile strength of 1850 MPa with VSL multi-strand system class E6-7 [5], is considered to be stressed by an unbonded post-tensioning system in the design. The ballast control system is designed considering the spar installation process comprising both solid ballast (black blast furnace slag with a unit weight of 28 kN/m<sup>3</sup>) and liquid ballast (seawater with a density of 10.26 kN/m<sup>3</sup>) [3]. Three lines of R4 stud diameter of 95 mm and unstretched length of 550 m, with each line at an angle of 120°, are applied as mooring lines.

Fairleads connecting the mooring lines are placed above mean sea level (MSL), considered to be restrained in the horizontal direction. The bottom end of the spar is constrained in the vertical direction to avoid any instability in the FE analysis under the assigned boundary conditions [3].

**TABLE 5.1:** Concrete and steel material properties

Material property	Concrete		Steel	
	Hull	Fairleads and tower connection	Class SD40 deformed bar	Class S355
Initial stiffness [MPa]	$2.2 \times 10^5$	$2.2 \times 10^5$	$2.1 \times 10^6$	$2.1 \times 10^6$
Poisson ratio	0.20	0.20	0.3	0.30
Unit weight [kN/m <sup>3</sup> ]	25.00	25.00	78.50	78.50
Tensile strength [MPa]	2.60	2.60	560.00	630.00
Compressive strength [MPa]	41.00	41.00	-	-
Yield strength [MPa]	-	-	390.00	355.00
Reinforcement ratio % (x, y, z)	0.7,0.7,1.4	0.1,0.1,0.1	-	-

**TABLE 5.2:** Bond element properties

Material property	Bond
Shear stiffness in closure mode [N/mm <sup>2</sup> /mm]	2.0 × 10 <sup>6</sup>
Normal stiffness in closure mode [N/mm <sup>2</sup> /mm]	2.2 × 10 <sup>6</sup>
Frictional coefficient	0.6
Shear stiffness in open mode [N/mm <sup>2</sup> /mm]	0.98
Normal stiffness in open mode [N/mm <sup>2</sup> /mm]	0.98

## 5.4 Hull Concrete under Water Pressure

In this study, hull concrete submerged in seawater is investigated. The impact of water pressure on the hull concrete is investigated by applying only the hydrostatic and hydrodynamic pressure to the hull surface. The load from upper part of the spar is not considered in FE analysis.

### 5.4.1 Hydrostatic and Hydrodynamics Pressure

Hydrostatic pressure is straightforward and depends on the water depth. It can be computed directly by the pressure formula as

$$P = \rho gh \quad (5-1)$$

Where  $g$  is gravitational acceleration 9.81 m/s,  $\rho$  represents the density of seawater 10.26 kN/m<sup>3</sup> and  $h$  denotes the water depth.

Hydrodynamic pressure, however, is taken from the predominant case of numerical analysis performed by WAMIT. The results show the storm wave with the wave heading (incident wave) of 180°, peak period  $T_p$  of 13.5 seconds given the maximum pressure, as found in the WAMIT pressure file. This is expected because a storm wave proceeds with the highest energy mentioned in Chapter 3. The plots of hydrodynamic pressure exciting on four faces of the



hull surface are shown in Figure 5.2. The hydrostatic and hydrodynamic pressure profiles applied to the COM3 FE model are shown in Figure 5.3.

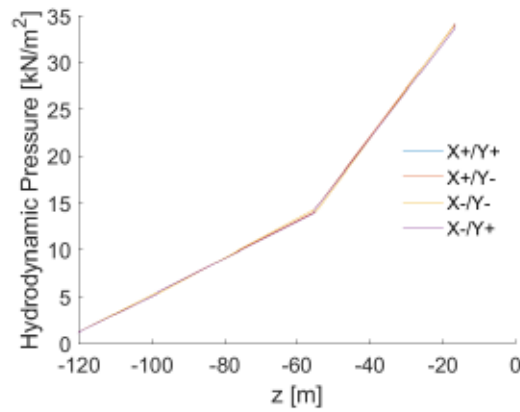


**FIGURE 5.2:** Hydrodynamic pressure excites on four faces of the hull surface using WAMIT

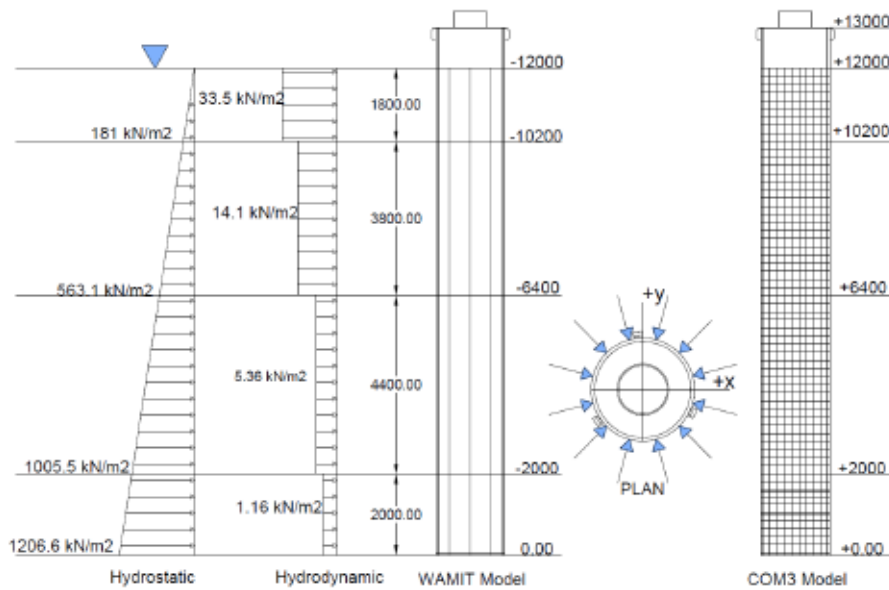


**FIGURE 5.3:** Hydrostatic and hydrodynamic pressure profile applied to FEM.

From Figure 5.3, we can observe the hydrodynamic pressure has the highest potential near the sea surface and decreases in deep water, opposite to hydrostatic pressure. In the case of a deep draft spar, the largest hydrostatic pressure is observed at the bottom part, while the hydrodynamic pressure is relatively small.

This becomes one of the disadvantages of a spar floating platform compared to other short draft floating platform concepts.

### 5.4.2 FE Analysis Results of Spar's Hull Concrete under Large Pressure

In order to investigate the hull concrete under this large pressure, only the pressure forces computed from hydrostatic and hydrodynamic pressure shown in Figure 5.3 are applied to the COM3 FE model.

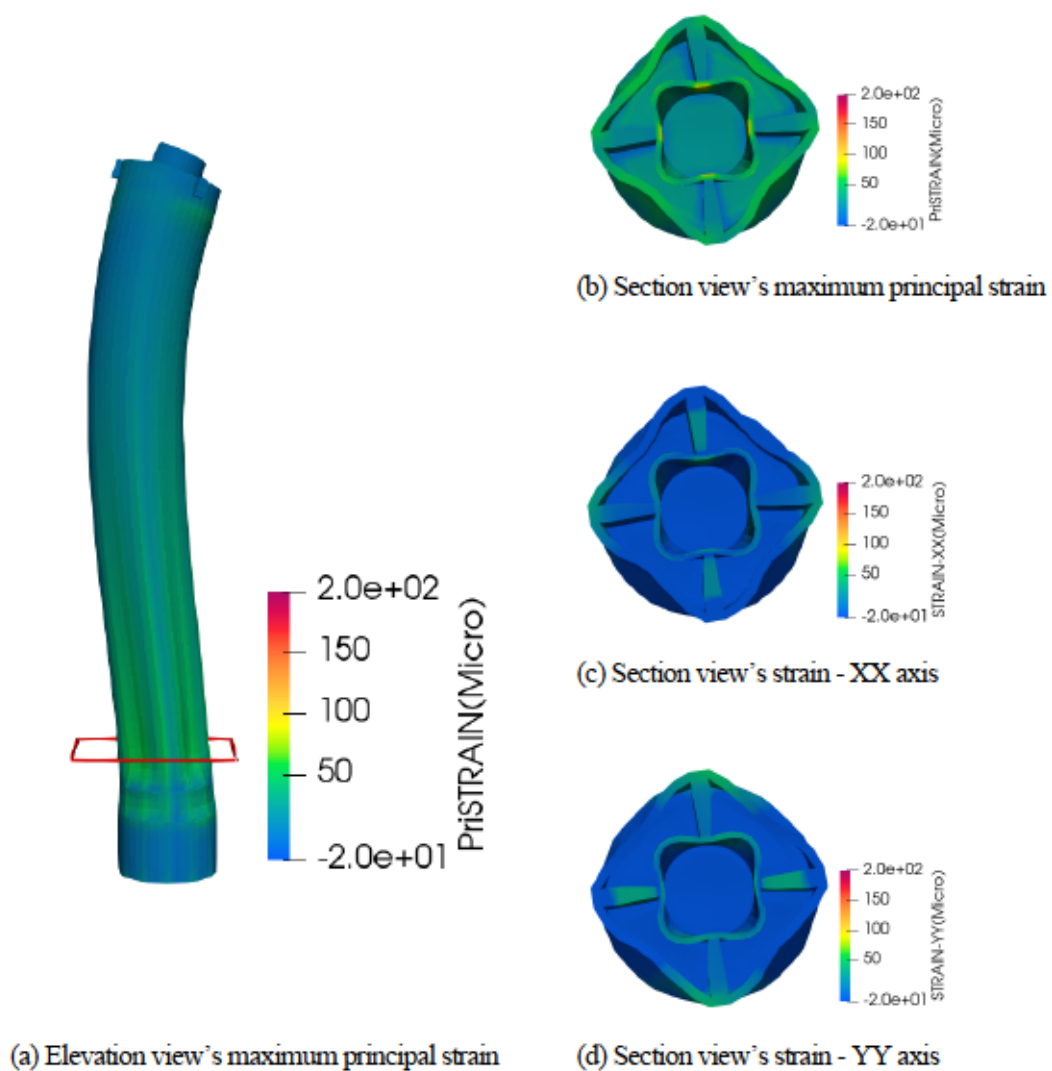


**FIGURE 5.4:** Structural deformation and strain distribution (scale factor 1000)

Despite that, there is concern that the structure could fail under the large hydrostatic pressure; however, the analysis results show the hull surface becomes under compression indicated by ultimate tensile strain ( $200 \mu\epsilon$ ) [6] as shown in Figure 5.4. This is attributed to enough thickness of hull concrete; in this case, the hydrostatic pressure functions as confinement. Therefore, the assumption of applying fixed in the vertical axis at the bottom end of the spar in the boundary condition is reasonable.

In Figure 5.4, we can observe the tensile strain in concrete doesn't exceed the ultimate tensile strain, the indicator of microcrack generating due to material softening [1]. Although there is small tension on the hull concrete, it is near zero and can be neglected. Therefore, it is not necessary to design circular prestressing tendons to resist any tensile force in the horizontal axis due to the water pressure. Only the vertical prestressing tendons need to be designed to resist the forces from the top part during the wind turbine operation.

## **5.5 Hull Concrete's Sectional Design**

In this section, the prestressed concrete design of the hull section will be first approximated and designed by hand calculation; after that, it will be implemented in the FE model.

### **5.5.1 Free Body Diagram**

As the results obtained from section 5.4, it is reasonable to simplify hand calculation by considering only the forces transfer from the top part of the spar to define the design bending moment of the section. Therefore, the forces applied to the structure are composed of the tower base forces and mooring tensions obtained from Chapter 3, which is presented in Table 5.3. The free-body diagram of the structure has been defined based on the structural deformation observed in Figure 5.4, shown in Figure 5.5.

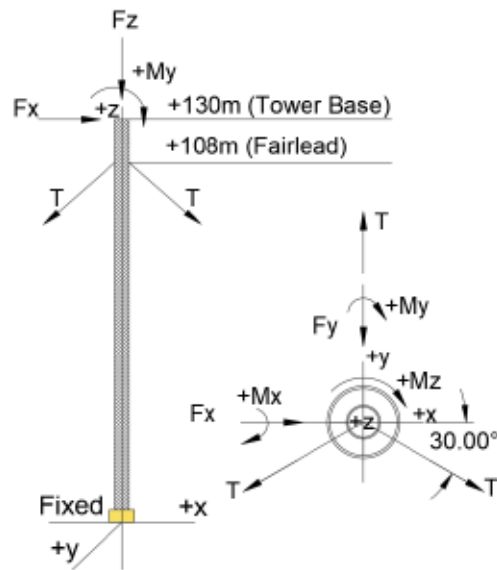


**FIGURE 5.5:** Free body diagram for the structural analysis

### 5.5.2 Design Flexural Bending Moment

The design bending moment obtained from Figure 5.5, which is the combination of tower base forces and mooring tension about the x-axis and the y-axis, is expressed in Equations 5-2 and 5-3

$$MX = -T * 108 - Fy * 130 + Mx \quad (5-2)$$

$$MY = Fx * 130 + My \quad (5-3)$$

**TABLE 5.3:** Maximum force under the operational and storm conditions

Description	Operational Condition			Storm Condition		
	11 [m/s]	25 [m/s]	41.9 [m/s]	11 [m/s]	25 [m/s]	41.9 [m/s]
Fx [kN]	2994	2046	-1194	3422	3354	-2907
Fy [kN]	-372	-947	111	-722	-1232	262
Fz [kN]	-13537	-13480	-13404	-13609	-13568	-13533
Mx [kN-m]	47661	102025	-10711	80551	128953	-25624
My [kN-m]	261274	162804	-178273	305523	-291623	-344843
Mz [kN-m]	3160	18407	4110	9841	30200	7808
Mooring Tension T [kN]	7916	2363	1590	7514	2386	1623

It is found that the operational condition, wind speed 11m/s, yielded a maximum bending moment  $M_X$  of 855,627 kN-m. Therefore, this moment will be kept as the design bending moment in subsequent analysis.

### 5.5.3 Ultimate Moment Capacity of a Circular Section Prestressed Concrete

The ultimate moment capacity of the section can be defined by applying the assumption of ASCE/PCI (1997) and ACI318 (ACI 2008) [7]. Figure 5.6 shows the concrete stress area and assumed stress distribution according to [7].

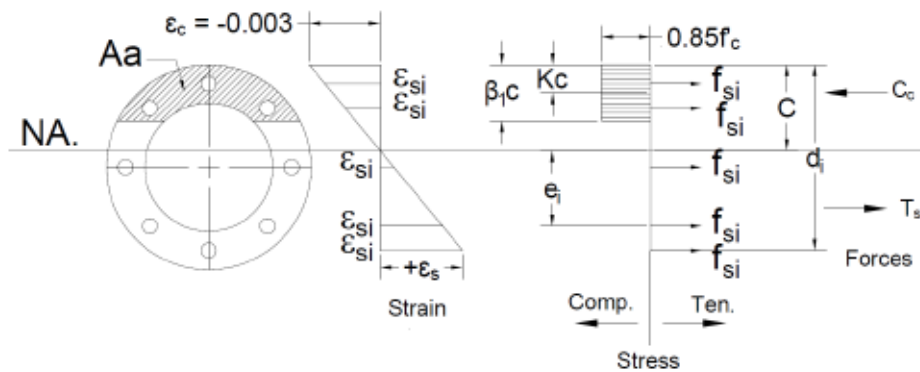


**FIGURE 5.6:** Concrete stress area and assumed stress distribution in a circular section

when;

$$C_c = 0.85f_c'Aa$$

$Aa$  = compressive area of the annular concrete section defined by equivalent stress block  $\beta_1 C$

$\beta_1 = 0.85$  for concrete strength  $f_c'$  of 27 MPa; 0.757 for  $f_c'$  of 41 MPa, and the minimum value is 0.65

$C$  = extreme compressive fiber to the natural axis (where strain  $\epsilon = 0$ )

$$KC \cong 0.5\beta_1 C$$

The assumptions to define ultimate moment capacity are as followings;

- The ultimate moment capacity of a circular at any given cross-section is a function of the prestressing steel and concrete strains.
- Steel and concrete are considered in the elastic and plastic ranges, respectively.
- The concrete compressive stress at failure is  $0.85f_c'$  (as taken from equivalent stress block methodology).
- The ultimate concrete compressive strain is  $\epsilon_c = 0.003$ .
- The yield steel strain is  $\epsilon_y = 0.01$ .
- The concrete tensile strength is neglected in flexural computations.
- The tensile strength of the prestressing tendons is neglected in the concrete compressive zone.
- The tensile strength of reinforcing bars is neglected.
- The conditions of compatibility and equilibrium are met.

The tensile capacity of the section can be expressed by

$$T_s = \Sigma A p_{st} f_{st} \quad (5-4)$$

The nominal moment capacity of the section is defined as

$$M_n = T_l e_l + Cc(C - KC) = A p_{st} f_{st} e_l + Cc(C - KC) \quad (5-5)$$

The ultimate moment capacity of the section is defined as

$$M_u = \phi M_n \quad (5-6)$$

$$\phi = 0.9$$

By trial and error until compatibility and equilibrium are met, the prestressed tendons were arranged to the hull section of the FE model, using 36 positions, with distancing between center to center of the adjacent

tendons is 10 degrees. Each position comprises 19 tendons utilizing low-relaxation 7-wire strands diameter of 15mm, Class270.

Figure 5.7 shows the stress and strain distribution of the section and the sectional design when the conditions of compatibility and equilibrium are met ( $T_s = C_c$ ). The results, without considering the safety factor  $\phi$ , show the nominal flexural capacity  $M_n = 1,392,163$  kN-m. And by applying safety factor  $\phi = 0.9$ , the ultimate flexural capacity can be defined as  $M_u = 1,252,947$  kN-m which is greater than the design bending moment  $MX$  of 855,627 kN-m and satisfied.

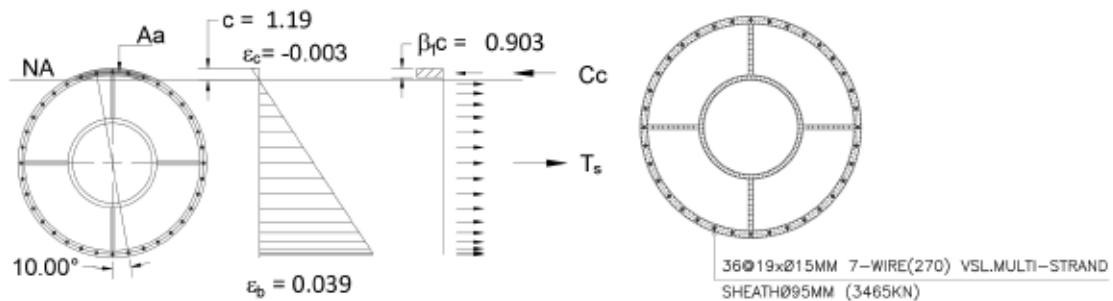


**FIGURE 5.7:** Stress and strain distribution of the section and the sectional design at equilibrium

#### 5.5.4 Interaction Diagram of the Section

In order to confirm the sectional capacity obtained from section 5.5.3 is capable of resisting the forces transfer from the wind turbine during operation, the interaction diagram of the section is determined in five control points [8]. The capacity of the section at each point which is pure tension, pure moment, tension-control, balance point (or compression-control), and pure compression, are shown in Table 5.4, where  $M_n$  is nominal flexural capacity, and  $N_n$  is nominal axial capacity.

The plot of the interaction diagram is presented as the M-N diagram and shown in Figure 5.8. The results indicate the design section can withstand the force transferred from the wind turbine to the prestressed concrete spar during wind turbine operation.

**TABLE 5.4:** Sectional capacity and the assumption at each control point

Point	$M_n$ [kN-m]	$N_n$ [kN]	Factor $\phi$	$\phi M_n$ [kN-m]	$\phi N_n$ [kN]
<b>Pure Tension</b> $T = \Sigma A_s F_y$	0	178114	0.90	0	160302
<b>Pure Moment</b> $T_s = C_c$	1392163	0	0.90	1252947	0
<b>Tension-Controlled</b> $\epsilon_c = -0.003, \epsilon_b = 2.5\epsilon_y$	1382527	-67156	0.90	1244274	-60441
<b>Balanced Point</b> $\epsilon_c = -0.003, \epsilon_b = 1\epsilon_y$	1454464	-217638	0.65	945401	-141465
<b>Pure Compression</b> $\epsilon_c = -0.003, \epsilon_b = 0.003\epsilon_y$	0	-1131446	0.65	0	-735440

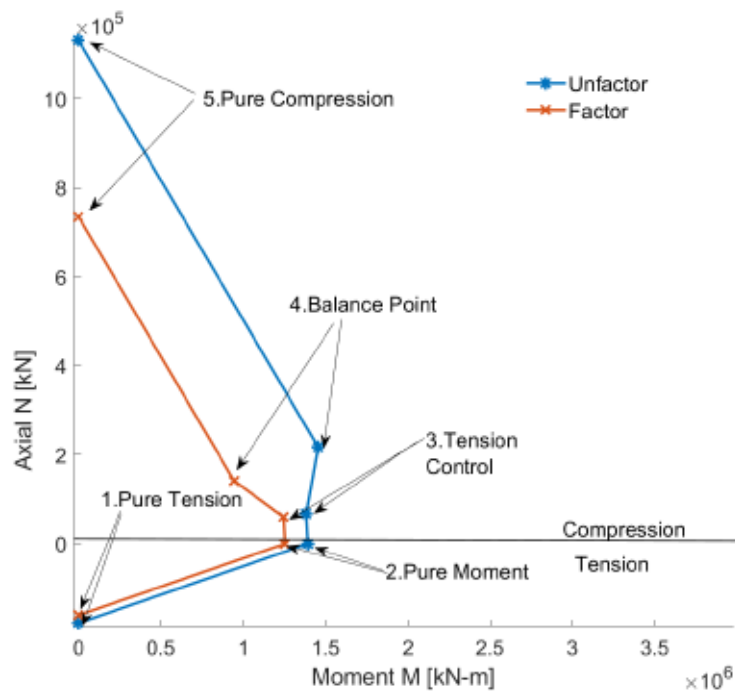


**FIGURE 5.8:** M-N diagram of the section at five control points



## 5.6 Tower Connection and Fairlead Connection Design

The connection between the steel tower and concrete spar as well as the fairlead connections are expected to have high potential stress concentrations because the forces transferred directly to these locations, causing a large deformation in the elements. As these connections are located above MSL, hydrostatic and hydrodynamic pressure have not been considered in this present FE analysis.

### 5.6.1 Study Cases and Loading Conditions

Table 5.5 shows five study cases of the FE analysis. CS1 and CS2 aim to observe the stress-strain distribution of the normal concrete models with reinforcement ratios of 0.1% and 1% without any connection design. After that, in CS3, CS4, and CS5, tower-connection design, mooring connection design and prestressed design will be applied to the model.

**TABLE 5.5:** The five study cases of FE analysis

Case	Case Details
CS1	A normal reinforced concrete (RC) with a 0.1% reinforcement ratio
CS2	A normal RC with a 1% reinforcement ratio
CS3	Applied a preliminary designed tower connection to CS1
CS4	Applied a preliminary designed mooring connection to CS3
CS5	Applied preliminary designed prestressing force to CS4

In this study, the highest forces selected from the dominant case of coupled dynamics simulation outputs in the time domain of OpenFAST will be applied to the FEM as static forces for a conservative structural design [3]. As presented in Table 5.3, the results indicated that a storm condition with a rated wind speed of 11 m/s yielded the highest tower base forces and mooring forces. The maximum tower base forces and mooring tension are therefore applied at the bottom of the steel tower and fairlead connections, respectively, as nodal forces with 20-timestep monotonic static loads.

## 5.6.2 FE Analysis and Preliminary Design of the Steel-Concrete Connections

### 5.6.2.1 Stress-strain concentrations of the FE model without connection systems

Study case CS1 is characterized by a normal reinforced concrete (RC) with a 0.1% reinforcement ratio. Localized stress and strain values without applying any connection systems and prestressing force are shown in Figure 5.9. For normal concrete, if the strain in concrete is greater than the ultimate concrete tensile strain ( $200 \mu\epsilon$ ), the microcrack starts to generate due to the material softening [1]. Thus, the red-highlighted area in Figure 5.9a represents the critical locations that must be strengthened to control crack development. Figure 5.9b presents the principal tensile stress. Although the red zone is higher than the concrete tensile strength (2.60 MPa), this stress can be transferred by the reinforcing bars because it remained within the elastic range of the steel material (yield strength of 390 MPa). Figure 5.9c shows that the principal compressive stress of concrete is mostly less than the concrete compressive strength utilized in this study; therefore, the normal concrete with a compressive strength of 41 MPa is applicable to design the proposed spar.

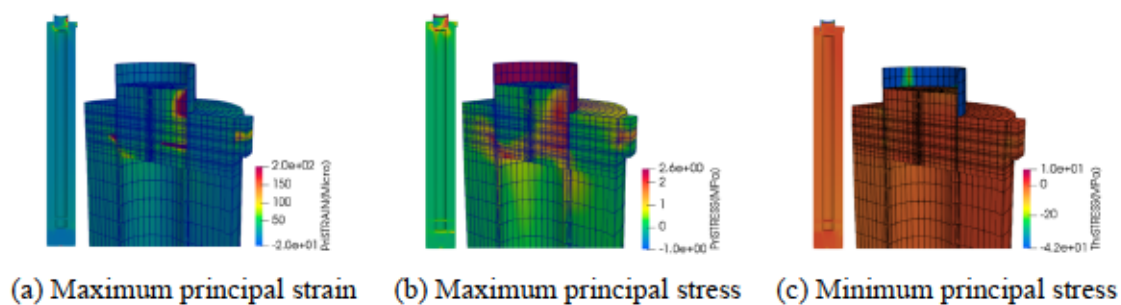


**FIGURE 5.9:** Stress-strain localization of normal RC with a 0.1% reinforcement ratio

Study case CS2 is characterized by a normal RC with a 1% reinforcement ratio. In this case, the higher reinforcement ratio of 1% is applied to the FE model. The results show smaller red areas than CS1, as presented in Figures 5.10a and 5.10b. This means tensile strain and tensile stress decreased due to more steels being implemented. However, the analysis results indicate that the stress-strain concentration still has a high potential at the steel-concrete connection parts.

Thus, it is necessary to design the connection system and prestressing force at the critical locations shown in the red zone of Figure 5.9a and 5.10a.

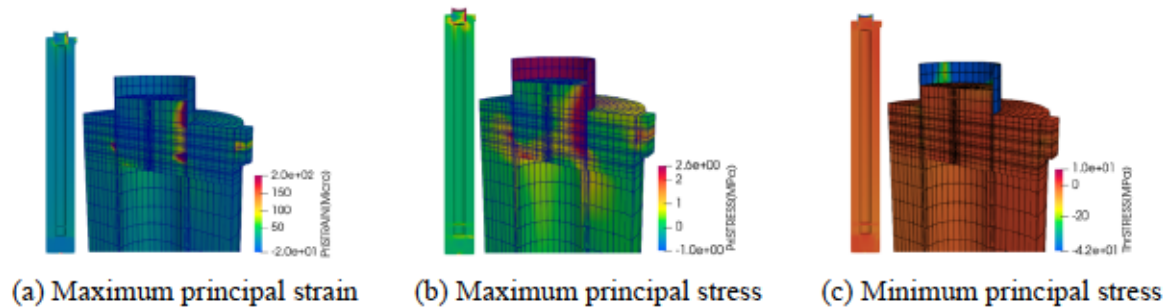


**FIGURE 5.10:** Stress-strain localization of normal RC with a 1% reinforcement ratio

### 5.6.2.2 Tower-spar connection design

In study case CS3, a preliminary designed tower connection to the model of normal RC with a 0.1% reinforcement ratio is applied. In this study case, the steel tower-spar concrete connection is designed by considering the critical area mentioned above. The preliminary embedded steel ring with triple rib layers is first utilized, as shown in Figure 5.11a and the detailed drawings presented in Figure 5.11b. This designed connection functions to lower and limit the concrete tensile strain developing cracks under the tower base. The analysis results show the pattern of strain distribution changed after implementing the designed steel ring, as presented in Figure 5.11c when compared to Figures 5.9a and 5.10a. The strain has now accumulated in high concentrations at the steel ribs and fairleads. The tensile strains of the critical elements located at the top rib and at the fairlead location are still much greater than the ultimate tensile strain.

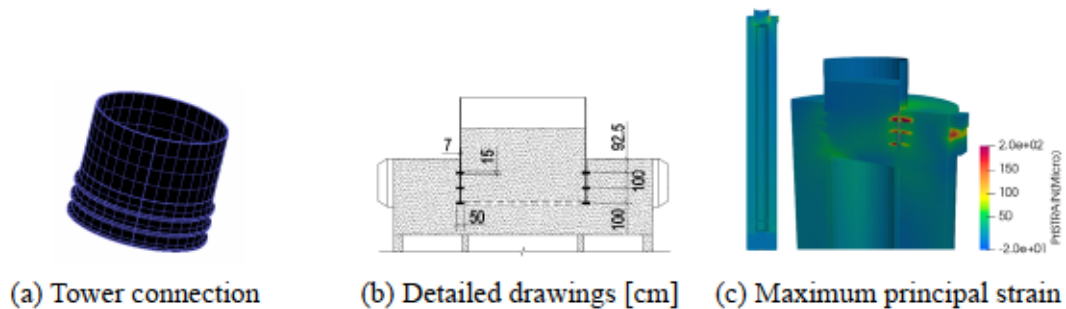


**FIGURE 5.11:** Preliminary designed tower connection and strain localization after installation

### 5.6.2.3 Fairleads connection design

In study case CS4, a preliminary designed mooring connection to the model of normal RC with a 0.1% reinforcement ratio installing tower connection (CS3) is applied. In this study case, the fairlead region is then investigated. This area is subjected to large tensile force transferred from mooring lines to the spar concrete. Rather than resisting by the reinforced concrete, this force is considered to be resisted by the two layers of a steel ring with triple connection plates shown in Figure 5.12a, and the detailed drawings presented in Figure 5.12b. The strain distribution after implementing this preliminary connection is presented in Figure 5.12c. The result shows the strain at the fairleads is now lower than the limit due to utilizing the steel material to resist these large tensions. The strain of the critical element at the tower connection are also significantly reduced compared to Figure 5.11c, which confirms the applicable designed mooring connection; however, it is still higher than the concrete ultimate tensile strain. Therefore, prestressed design is necessary to strengthen this critical area and limit crack development.

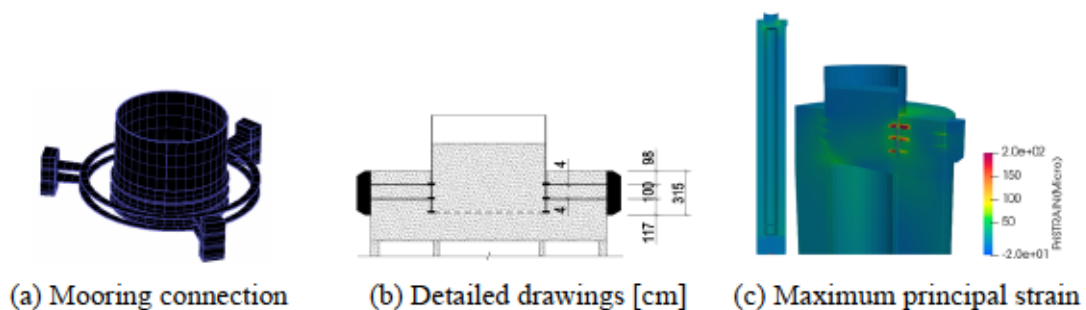


**FIGURE 5.12:** Preliminary designed mooring connection and strain localization after installation

### 5.6.2.4 Prestressed concrete design at the connection zone

In study case CS5, a preliminary designed prestressing force to the model of normal RC with a 0.1% reinforcement ratio installing both tower connection (CS3) and mooring connection (CS4) is applied. The prestressing force is then designed in this study case to limit crack generation and propagation at the critical area of the red zone presented in Figure 5.12c. Thus, the surrounding area of the rib plates of the tower connection is the area to arrange prestressing

tendons and apply prestressing force. Considering relaxation of prestressing steel that must not affect the structural performance during its service life, the initial stress  $0.6F_{py}$  [5] or prestressing force of 154 kN with initial strain 0.0055, is applied to 7 tendons (total of 1078 kN) of the low-relaxation 7-wire strands diameter of 15mm, Class270, utilizing the multi-strand anchorage system. The profile tendons and reinforced details of a normal RC with a 0.1% reinforcement ratio employed in FE analysis are shown in Figures 5.13a and 5.13b, respectively. The strain distribution after applying prestressing force is shown in Fig 5.13c, where the red-highlighted area is now left only at the top rib.

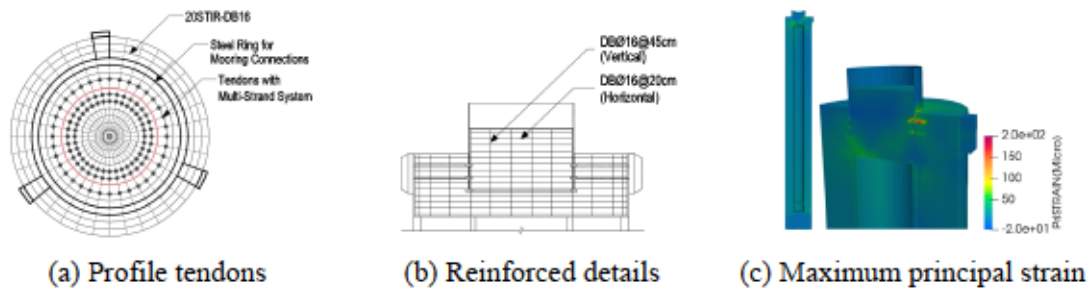


**FIGURE 5.13:** Preliminary designed prestressed concrete and strain localization after installation

#### 5.6.2.5 Stress-strain relationship of the critical member after applying connection system and prestressing force

CS5's stress-strain relationship in the z-axis, in which the concrete was pre-compressed by prestressed tendons, and the maximum principal stress-strain relationship of the critical member are plotted together with those of CS3 and CS4. The analysis results show that the concrete strain is greatly reduced attributed to applying prestressing force, particularly in the z-axis, as shown in Figure 5.14a, which is now lower than the ultimate tensile strain  $200 \mu\epsilon$ , and the principal tensile strain is reduced nearly to the limit, as presented in Figure 5.14b, which is acceptable. Therefore, the prestressed design satisfies the design objective of crack control.

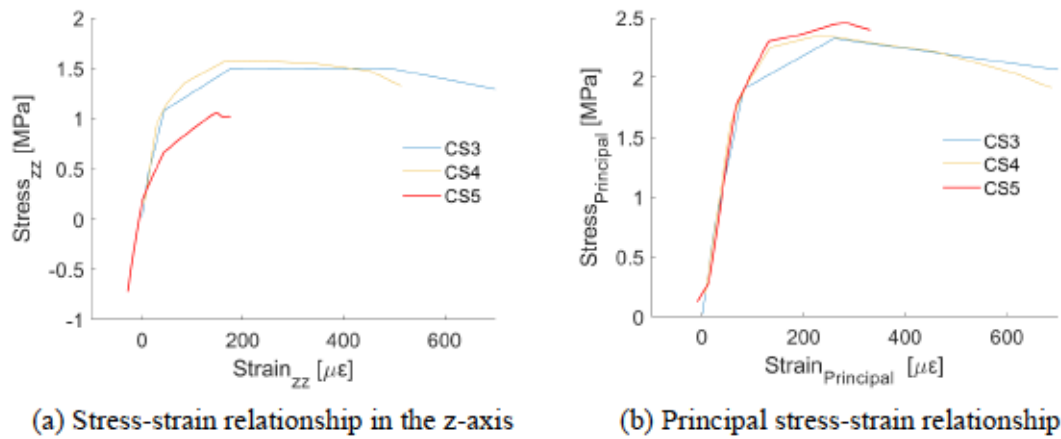


**FIGURE 5.14:** Stress-strain relationship of a critical element of study cases CS3, CS4 and CS5

### 5.6.3 Structural Behavior of the Five Study Cases

The inclination of the tower in vertical and horizontal directions subjected to the bending moment of the wind turbine under operation are presented as the  $M$ - $\phi$  diagram shown in Figures 5.15a and 5.15b. In CS1, the tower deformation, represented by  $\phi$ , has increased linearly in proportion to the applied bending moment. Similarly, CS2 shows smaller deformation attributed to a higher reinforcement ratio of 1% implemented. For CS3, CS4, and CS5, the linear graphs have changed to steep slopes due to applying the designed connection systems and prestressing forces. It shows much smaller tower deformation in both directions than CS1 and CS2, in which the connection system has not been installed.

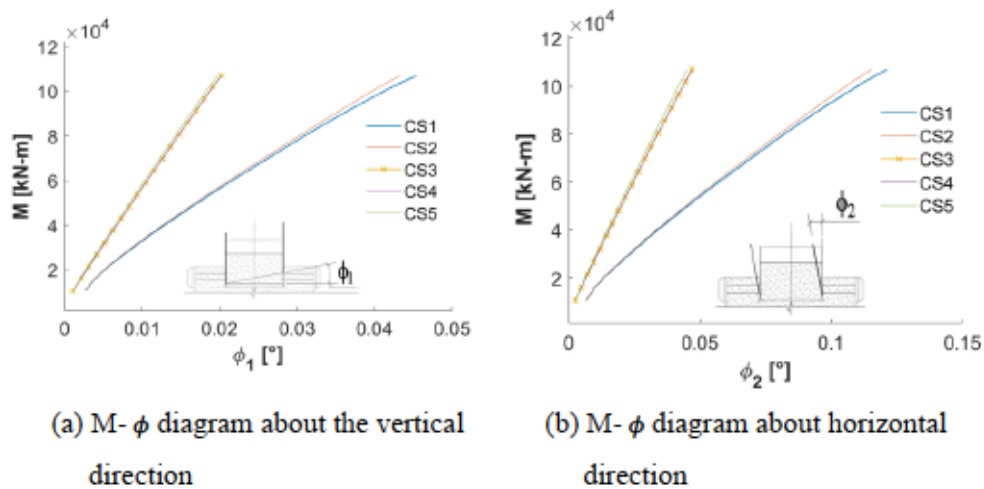


**FIGURE 5.15:**  $M$ - $\phi$  diagrams in vertical and horizontal directions of the five study cases

Interestingly, the difference in tower deformation between CS3 and CS4 is very small so that the graph almost overlaps with each other and is near CS5. This means the tower deformation is contributed to the tower connection rather than the mooring connection and prestressed design. The mooring connection has prevented the large tensile force transferring to the tower connection zone, and the prestressing force has limited concrete tensile strain; as a result, cracks generation and propagation stop.

The example of structural displacements before and after implementing a tower connection system (CS1 and CS3) are shown in Figures 5.16a and 5.16b. It can be observed that the tower connection prevents the steel tower from buckling failure and pulling out of the concrete spar floater due to large bending moment during wind turbine operation. The connection systems and prestressed design successfully prevent the tower from large deformation and satisfy the design objective of crack control.

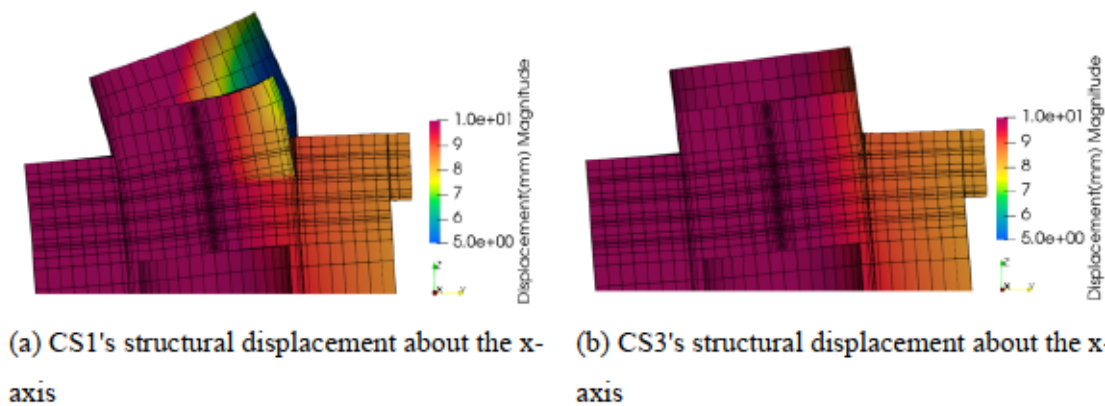


**FIGURE 5.16:** Structural displacements of study cases CS1 and CS3 (scale factor 300)

### 5.7 FE Analysis Results of a Proposed Concrete Spar

Now it is time to integrate the structural design of the proposed precast segment prestressed concrete spar obtained from Sections 5.5 and 5.6. The static forces applied to the FE model will comprise the maximum tower base forces, mooring tension, hydrostatic and hydrodynamic forces. These forces will be applied to the FE model as nodal forces with 35-timestep monotonic static loads to avoid any instability in FE analysis.

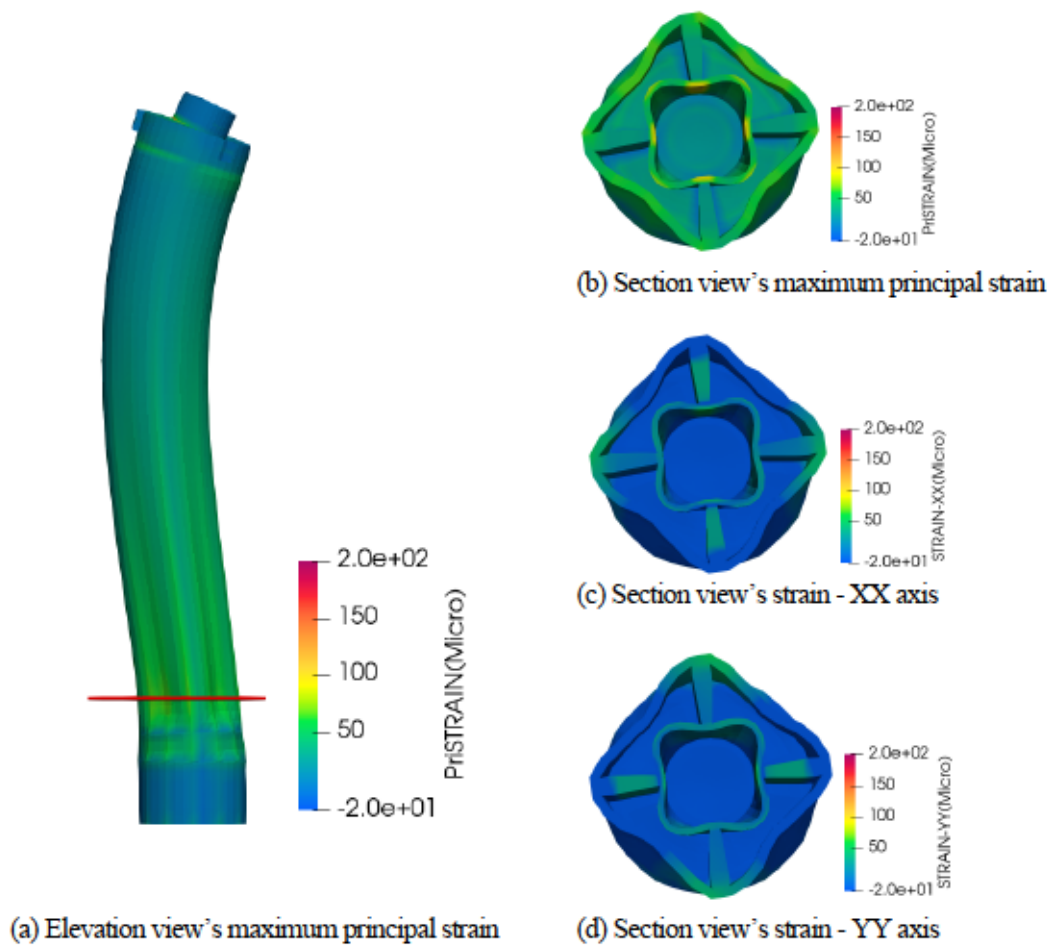


**FIGURE 5.17:** Structural deformation and strain distribution (scale factor 1000)

The FE model in this study has installed tower connection, fairlead connection, and prestressing tendons obtained from the previous sections. The initial strain of 0.0055 is applied to all prestressing steel; in other words, the initial stress below  $0.6F_{py}$  is applied to the tendons. Consequently, the effect of the relaxation of prestressing steel will be very small and will not affect the structural performance during its service life of 25-30 years [5]. The reinforcing bars are designed for shear (stirrup) following JSCE [6] and ACI [8] design standards. The bond reinforcement is considered for the structure containing unbonded tendons [5]. Therefore, the reinforcement ratio 0.1% is applied in the x and y directions, and 0.2% is applied in the z direction in the FE model.



The FE analysis results show the proposed spar can resist the forces without structural failure and is confirmed by low tensile strain. This implies that the proposed spar can support the 10MW reference wind turbine. Figure 5.17 shows the structural deformation and strain distribution of the FE analysis.

### 5.8 Advantages of the Proposed Concrete Spar

Simple and competitive are the advantages of this proposed spar. According to the simple shape, it is easy to cast, assemble and simple for unskilled laborers in any local community to join the concrete work. Meanwhile, it's competitive in using low-cost materials, normal concrete, and doesn't require high-skill labor. In terms of weight, the 130m-proposed spar weight of 18,000 Tons, a 6m-hull concrete segment weight of 700 Tons, and 20 hull concrete segments are needed for one spar. Figure 5.18 shows the sectional design of precast segment hull concrete and the final reinforcement of the hull and tower connection.

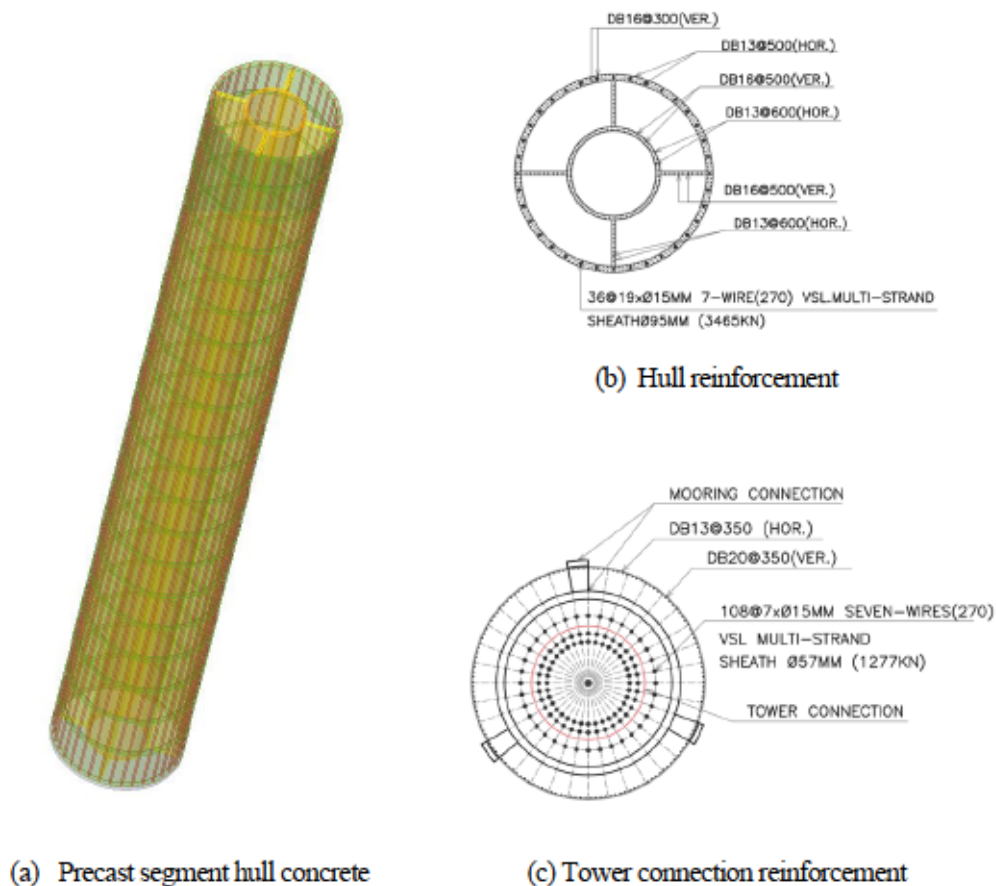


**FIGURE 5.18:** Precast segment hull concrete and final design reinforcement.

To illustrate the idea, assuming a construction project of a floating offshore wind farm capacity of 1GW with a 30-year license, we will need 100-unit concrete spars weighing 1,800,000 tons of concrete. If the concrete plants have a capacity of 900,000 tons per year, the concrete work is possible to finish in two years. Precast concrete is well known as industry mass production; therefore, construction work is possible to finish faster than steel manufacturers.

## **5.9 Conclusion for Chapter 5**

The non-linear behavior of spar concrete was investigated in FE analysis. Steel-concrete connections for towers and fairleads, as well as structural design for a prestressed concrete spar floater supporting a 10 MW floating offshore wind turbine, are demonstrated in this study. Based on the results, the following conclusions are earned:

1. The highest hydrodynamic pressure is obtained from a wave heading of  $180^\circ$ , peak period 13.5 seconds (storm wave) of the WAMIT analysis results. This is expected because a storm wave creates the highest wave energy.
2. For a deep draft spar, hydrostatic pressure becomes a dominant force in designing the structure. Hydrodynamic pressure has the highest potential near the seawater surface, but it decreases in the deep water. On the other hand, hydrostatic pressure is relatively large exciting at the bottom part of the spar. This becomes one of the disadvantages of a spar floating platform compared to other short draft floating platform concepts.
3. Although there is a concern that the structural analysis could fail under the large hydrostatic pressure, it is found that, for a spar concrete with thick enough hull thickness, the hull surface becomes under compression. Therefore, it is not necessary to design pretesting force in the horizontal axis to resist any tensile force attributed to water pressure.
4. The FEA results show concrete compressive stress is generally lower than the compressive capacity of the normal strength concrete of 41 MPa applied in this study. Therefore, normal concrete can be used to design a spar concrete to realize an economic structure.

5. The highest stress and strain concentrations occur in the steel-concrete connection parts as expected. A concrete strain that is over the ultimate tensile strain will initiate cracking; this area is highlighted as the critical area for designing prestressing force.
6. The preliminary design of a steel ring with triple rib layers applied at the tower connection can change the pattern of dispersal strain distribution under the steel tower by accumulating at the steel ribs, which is useful for structural design.
7. The preliminary design of the two layers of a steel ring with triple connection plates applied for the fairlead connections successfully resists the large tensile forces transferred from mooring lines to the proposed concrete spar. It can also prevent these forces from transferring to the critical zone located around the tower base area, as confirmed by the concrete strain significantly reduced in the critical element after implementing this connection type.
8. The preliminary connection systems and prestressed design have successfully prevented the steel tower from buckling failure and pulling out of concrete due to the large bending moment under the operation of the wind turbine, as well as the crack generation and propagation in concrete parts of the proposed spar.
9. The proposed prestressed concrete spar can be applied to support an RWT during operation, as shown in the interaction diagram of the section. This is confirmed by FE analysis results that show no structural failure.

### **Nomenclature in Chapter 5**

$A_a$	compressive area of the annular concrete section defined by an equivalent stress block $\beta_1 C$
$A_{p_{st}}$	area of each prestressing bar
$C_c$	compressive capacity of the section (force)
$e_l$	distance from the natural axis $NA$ of the section to the center of each prestressing bar
$f_c'$	concrete compressive strength
FE	finite element
FEA	finite element analysis

FEM	finite element model
$F_{py}$	yield stress of the prestressing bar
$f_{st}$	the tensile stress of each prestressing bar
$F_x$	tower base shear force in the $x$ direction
$F_y$	tower base shear force in the $y$ direction
$F_z$	tower base shear force in the $z$ direction
$g$	gravitational acceleration 9.81 m/s
$h$	water depth
$K_c$	distance from the top fiber to the compression force of section $\cong 0.5\beta_1$
$M_x$	tower base bending moment in the $x$ direction
$M_X$	design flexural bending moment in the $x$ direction
$M_Y$	design flexural bending moment in the $y$ direction
$M_y$	tower base bending moment in the $y$ direction
$M_z$	tower base bending moment in the $z$ direction
$M_n$	nominal moment capacity of the section
$M_u$	ultimate moment capacity of the section
$NA$	natural axis of the section
$P$	water pressure
RC	reinforced concrete
T	mooring line tension
$T_p$	peak period of the wave spectrum
$T_s$	the tensile capacity of the section (force)
$\epsilon_c$	ultimate concrete compressive strain
$\epsilon_s$	steel strain of prestressing bar
$\epsilon_{st}$	steel strain of each prestressing bar
$\epsilon_y$	yield steel strain of prestressing bar
$\rho$	density of seawater 10.26 kN/m <sup>3</sup>

$\phi$  ultimate capacity safety factor 0.90 for flexural and 0.65 for axial capacity.

## References in Chapter 5

- [1] Maekawa, K., Okamura, H., and Pimanmas, A., 2003, *Non-Linear Mechanics of Reinforced Concrete*, CRC Press.
- [2] Maekawa, K., 2008, *Multi-Scale Modeling of Structural Concrete*, Crc Press.
- [3] Munbua, W., Hasan, M. S., Malta, E. B., Gonçalves, R. T., Fujiyama, C., and Maekawa, K., 2022, "Conceptual Design of a Prestressed Concrete Spar Floater Supporting a 10 Mw Offshore Wind Turbine," *International Conference on Ocean, Offshore and Arctic Engineering*, American Society of Mechanical Engineers, Hamburg, Germany.
- [4] Bortolotti, P., Tarres, H. C., Dykes, K., Merz, K., Sethuraman, L., Verelst, D., and Zahle, F., 2019, "IEA Wind TCP Task 37: Systems Engineering in Wind Energy - WP2.1 Reference Wind Turbines," p. 138.
- [5] Collins, M. P., and Mitchell, D., 1997, *Prestressed Concrete Structures*, Response Publications.
- [6] 2010, *JSCE (2007). "Standard Specification for Concrete Structures, Design,"* Japan Society of Civil Engineers (JSCE), Shinjuku, Tokyo.
- [7] null, null, Oliphant, W. J., and Sherman, D. C., 2012, *Prestressed Concrete Transmission Pole Structures*, American Society of Civil Engineers.
- [8] Committee 318, A. C. I., 2014, *Building Code Requirements for Structural Concrete (ACI 318-14): An ACI Standard : Commentary on Building Code Requirements for Structural Concrete (ACI 318R-14), an ACI Report*, American Concrete Institute.

## CHAPTER 6

### PROPOSED FAIRLEAD CONNECTIONS

#### 6.1 Introduction

The chapter aims to design and propose the fairlead connections, the position that mooring lines connect to spar concrete. Five types of fairlead connections are studied, and the fatigue analysis is then carried out to evaluate the structure's service life.

#### 6.2 FE Model

As of the previous study in Chapters 3 and 5, the large tensile force transfers from mooring lines to spar concrete through the fairlead positions. In this chapter, only the fairlead connection is investigated; therefore, only the connection zone is modeled in FE analysis.

First, the connection plate is approximated and designed by hand calculation to resist maximum mooring tension obtained from the coupled dynamic analysis results, as mentioned in Chapter 3 and Chapter 5. The maximum mooring tension of 7,514 kN is selected from a wind speed of 11m/s at storm conditions. Steel material class S355 with a yield strength of 355 MPa is applied to design the steel plate. The FE model has installed tower connection and applied prestressing force obtained from Sections 5.6. The bottom part of the model is fixed in the applying boundary conditions. The 3D FE meshes model of the connection zone and the main preliminary dimension of the steel connection plate, unit millimeter [mm], are shown in Figure 6.1.

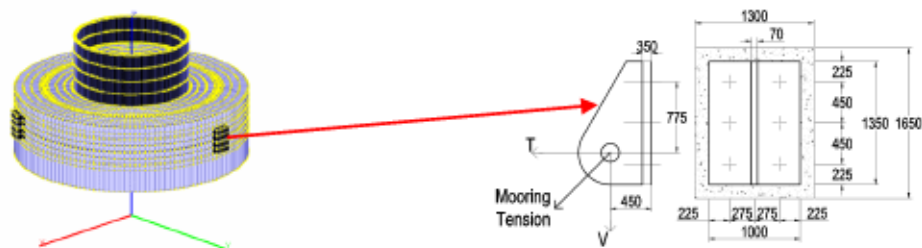


**FIGURE 6.1:** 3D FE model of the connection zone and main dimension of the steel connection plate

### 6.3 Five Types of Proposed Fairlead Connections

There are five types of fairlead connections proposed in this section which stress and strain distribution are investigated. Table 6.1 shows the name and the concept of each type. The drawings and FE model of each connection type are shown in Figures 6.2 to 6.6.

In these models, the same steel material (class S355) designed for the connection plate is applied to the steel plate. The high-strength wire rope 6x37 class IWRC EEIPT diameter 74 mm is selected and applied to the steel wire of the wire-plate and wire-wire models. Anchor bolts (AM), diameter 28 mm conformed to S355CN with tensile strength 490 MPa [1], embedded length of 1200mm, are utilized to the anchor bolt and anchor bolt-prestress model. The deformed prestressing bar diameter of 36 mm with tensile strength 1030 MPa initial strain 0.003 is applied to the anchor bolt-prestress model.

Note that the concrete needs to be cast in full sections for four connection types (except for the anchor bolt-prestress model) because the interlocking mechanism between steel and concrete is necessary to resist large mooring tension. However, for type five, the anchor bolt-prestress model, concrete can be cast in a hollow section due to prestressing force is applied to the connection system resisting the mooring tension.

**TABLE 6.1:** Name and concept of the fairlead connection systems

Name	Concept
1. Plate-Plate model	The connection plate is connected to the steel plate and two-layer steel ring, the same concept as Chapter 5.
2. Wire-Plate model	The connection plate is connected to the steel plate and two-layer steel wire.
3. Wire-Wire model	The connection plate is connected to the steel wire and two-layer steel wire.
4. Anchor Bolt model	The connection plate is connected to 6 anchor bolts embedded in concrete, as a normal connection.
5. Anchor Bolt – Prestress model	The connection plate is connected to 6 anchor bolts embedded in concrete, and deformed prestressing bar are applied

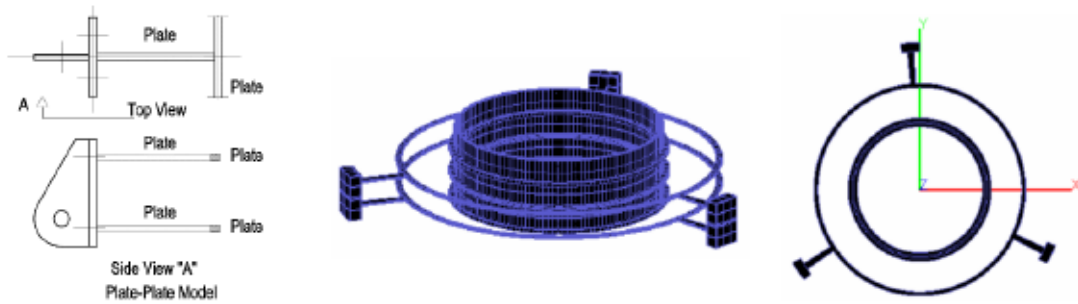


**FIGURE 6.2:** Drawing and FEM of Plate-Plate model

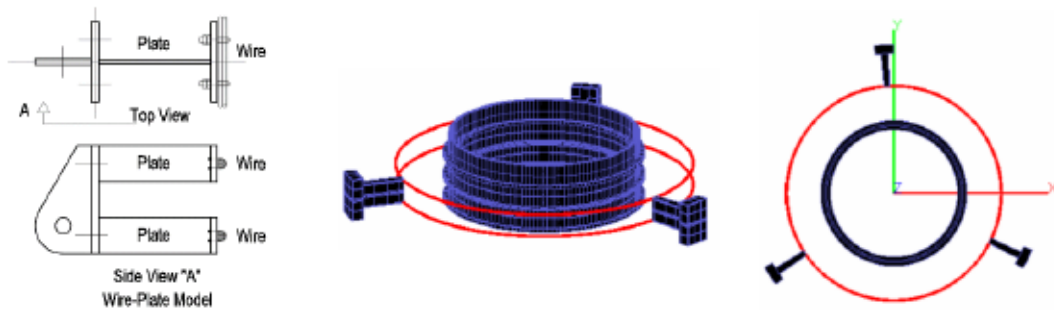


**FIGURE 6.3:** Drawing and FEM of Wire-Plate model

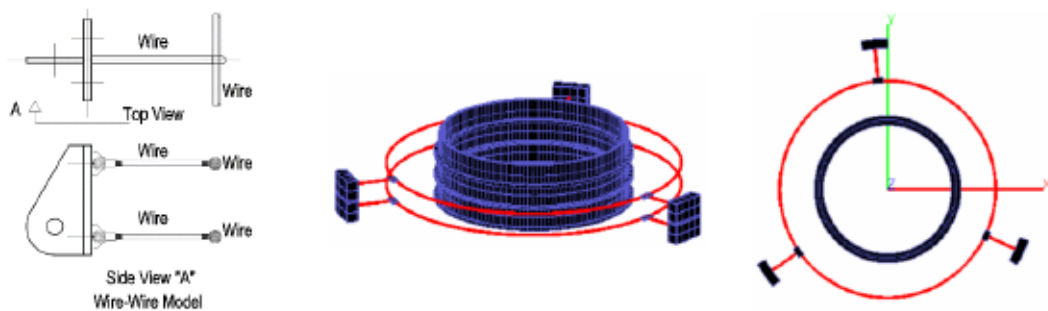


**FIGURE 6.4:** Drawing and FEM of Wire-Wire model



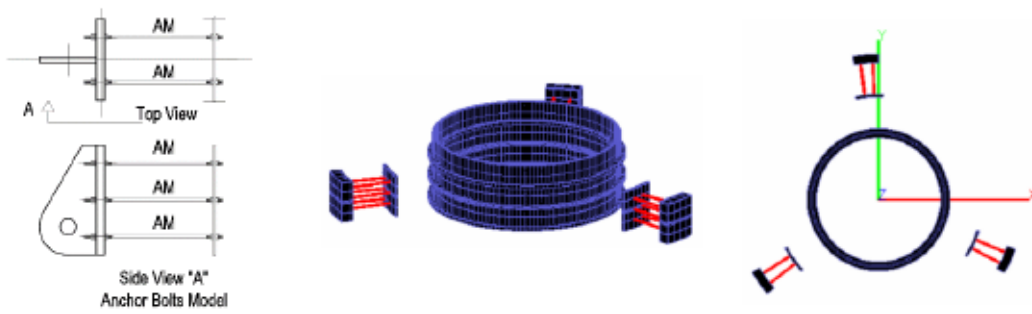


**FIGURE 6.5:** Drawing and FEM of Anchor Bolt model

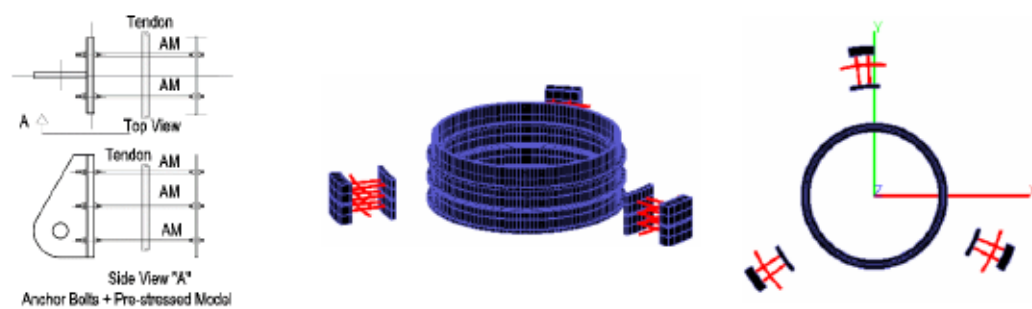


**FIGURE 6.6:** Drawing and FEM of Anchor Bolt – Prestress model

## 6.4 FE Analysis Results

### 6.4.1 Stress and Strain Distribution

In this section, the 20-time step monotonic static loads are applied to the FE model (Section 5.6). The location of the critical element, with a high stress-strain concentration, can be indicated by the distribution of principal strain, tensile stress, and compressive stress. Figures 6.7 to 6.11 show the results of the stress-strain distribution obtained from FE analysis.

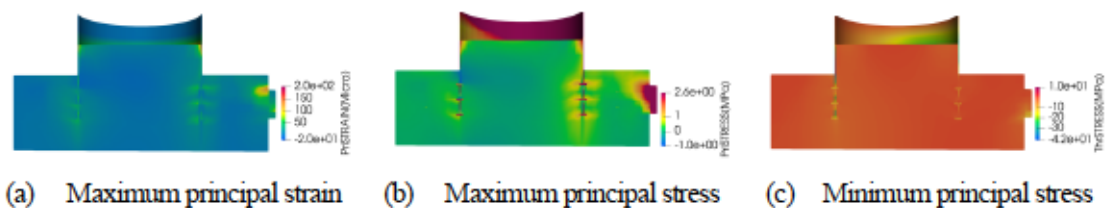


**FIGURE 6.7:** Stress-strain distribution of Plate-Plate model

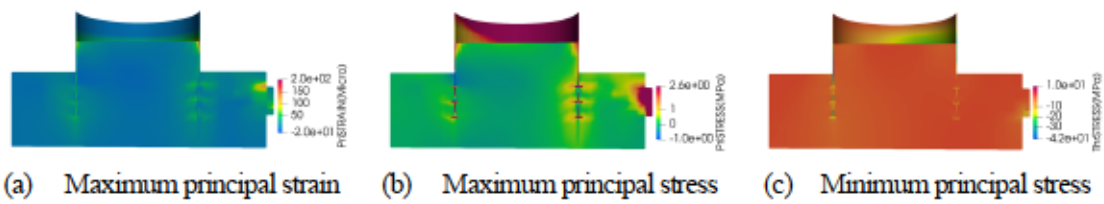


**FIGURE 6.8:** Stress-strain distribution of Wire-Plate model

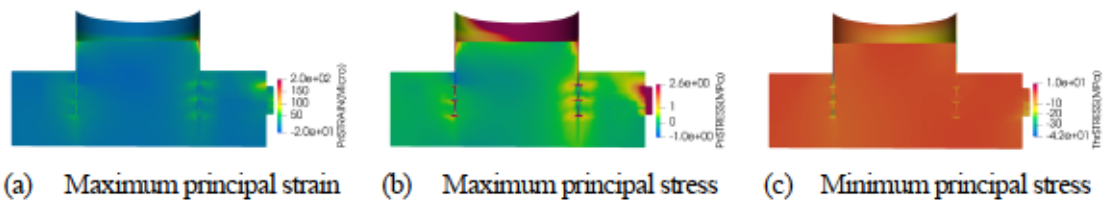


**FIGURE 6.9:** Stress-strain distribution of Wire-Wire model

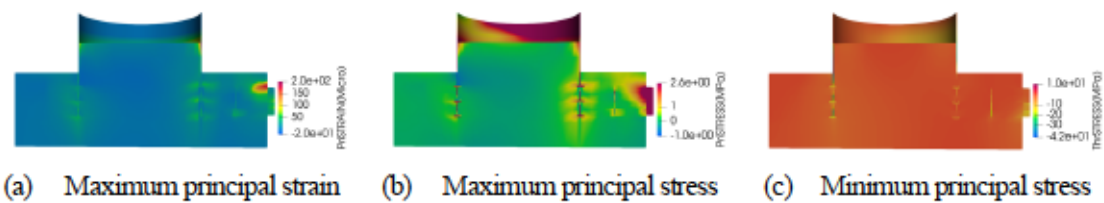


**FIGURE 6.10:** Stress-strain distribution of Anchor Bolt model

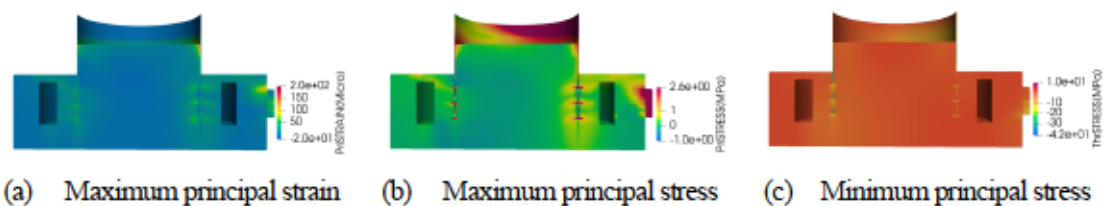


**FIGURE 6.11:** Stress-strain distribution of Anchor Bolt–Prestress model

In all connection types, the location that strains in concrete is over than the ultimate tensile strain ( $200 \mu\epsilon$ ) located above the connection plate. In this case, microcracks start to generate due to material softening [2] at the red highlighted areas shown in Figure 6.7a to 6.11a. This can be expected because it is consistent with the direction of mooring tension applied to FEM, as shown in Figure 6.1. Therefore, concretes located around the top part of the connection plate are under

tension. The tensile stress of concrete is over than the tensile strength of 2.6 MPa in this location, as the red highlighted areas shown in Figure 6.7b to 6.11b.

On the other hand, concretes located around the bottom part of the connection plate are under compression. However, the compressive stress of concrete is lower than the compressive capacity 41MPa, as shown in Figures 6.7c to 6.11c. Concrete under tensile force and compressive force around the connection plate of fairlead connections significantly affect the structure's service life which needs to be investigated. The fatigue analysis is then conducted in the following section.

## **6.5 Fatigue Analysis**

### **6.5.1 Load Conditions**

Fatigue analysis is performed on the five connection types by applying the load magnitude obtained from section 5.6. First, the results of a storm condition with a wind speed of 11 m/s are selected. These forces are applied to the model with a 10-timestep monotonic static force to avoid any instability of the element. Therefore, the load magnitude is divided by ten, considering each time step equivalent to one second.

Next, in the fatigue analysis, the model is treated by loading ten steps and unloading ten steps until the failure occurs in the form of cracking, crushing, and other forms of concrete failure and yielding of reinforcement [3]. Therefore, it takes 10 seconds to complete one loading cycle (10 steps) and another 10 seconds to complete one unloading cycle. In sum, 20 seconds are needed to complete a cycle of loading and unloading. In other words, the loading rate is 0.2 Hz.

Since it takes time to compute the time-dependent scenario when a huge number of cycles are needed, the magnificient factor,  $\xi$ , in terms of the logarithmic derivative, is applied to speed up this computation [4]. By doing so, the load of 460 time-step with around 84.38 million cycles is applied to the FE model. Figure 6.12 shows load magnitude versus time of the mooring tension applied at the fairlead connection; the highest magnitude is 7,514 kN, and the lowest magnitude is 0 kN.

This magnitude is approximately 95% load level of the connection plate tensile capacity. Note that the actual capacity of the proposed fairlead connections will be much higher considering the interface between

concrete and embedded steel material integrated with the connection plate capacity. However, the failure mode of the system is expected to first appear at the connection plate in the form of yielding after resisting large mooring tension. Therefore, it is reasonable that in fatigue analysis, the capacity of fairlead connections is considered only the tensile capacity of the connection plate.

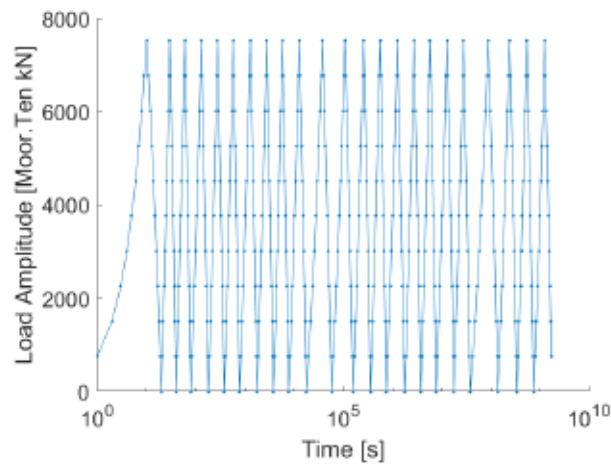
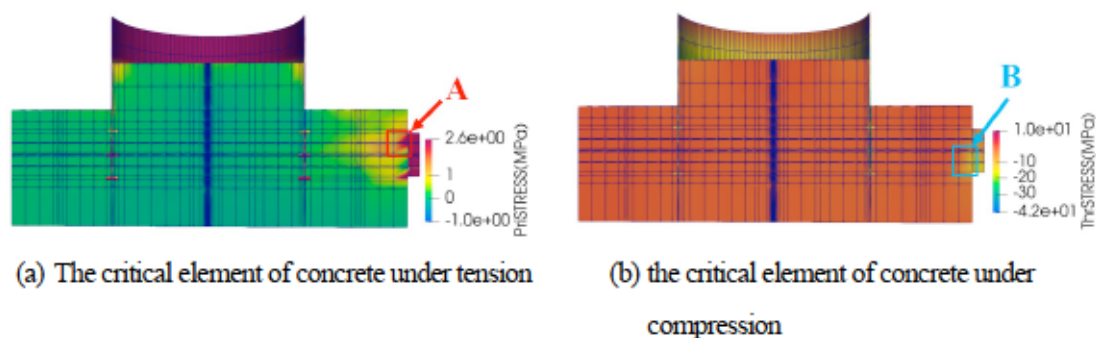


**FIGURE 6.12:** Load amplitude of mooring tension versus time applied at fairlead connection

### 6.5.2 Fatigue Life Estimation

The critical elements of concrete under tension and compression can be defined as mentioned in Section 6.4. The location of the critical elements taken for fatigue analysis shows in Figure 6.13. Note that, in this model, the mooring tensions were applied to the FE model in the vertical direction (ZZ-axis). Therefore, tensile stress and compressive stress of the elements in this axis are dominant and will be taken to evaluate the fatigue life of the structure.



(a) The critical element of concrete under tension

(b) the critical element of concrete under compression

**FIGURE 6.13:** Location of the critical elements taken for fatigue life estimation

### 6.5.2.1 Fatigue life of concrete under tension

According to CEB-FIP model code 1990 [5], the fatigue life of concrete under pure tension and tension-compression can be evaluated as;

When  $\sigma_{ct,max} > 0.026|\sigma_{c,max}|$

$$\text{Log}N = 12(1 - S_{ct,max}) \quad (6-1)$$

where;

$S_{ct,max}$  is the maximum tensile stress level defined by  $\sigma_{ct,max}/f_{ctk,min}$

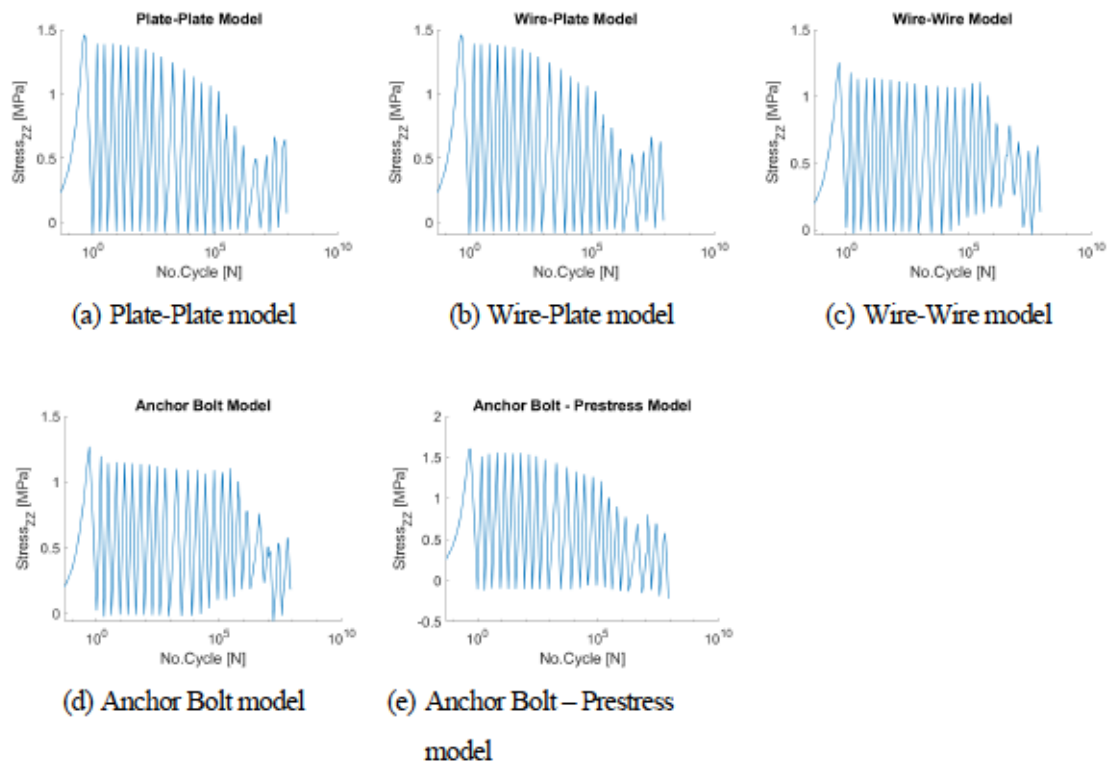
$\sigma_{c,max}$  is the maximum compressive stress

$\sigma_{ct,max}$  is the maximum tensile stress

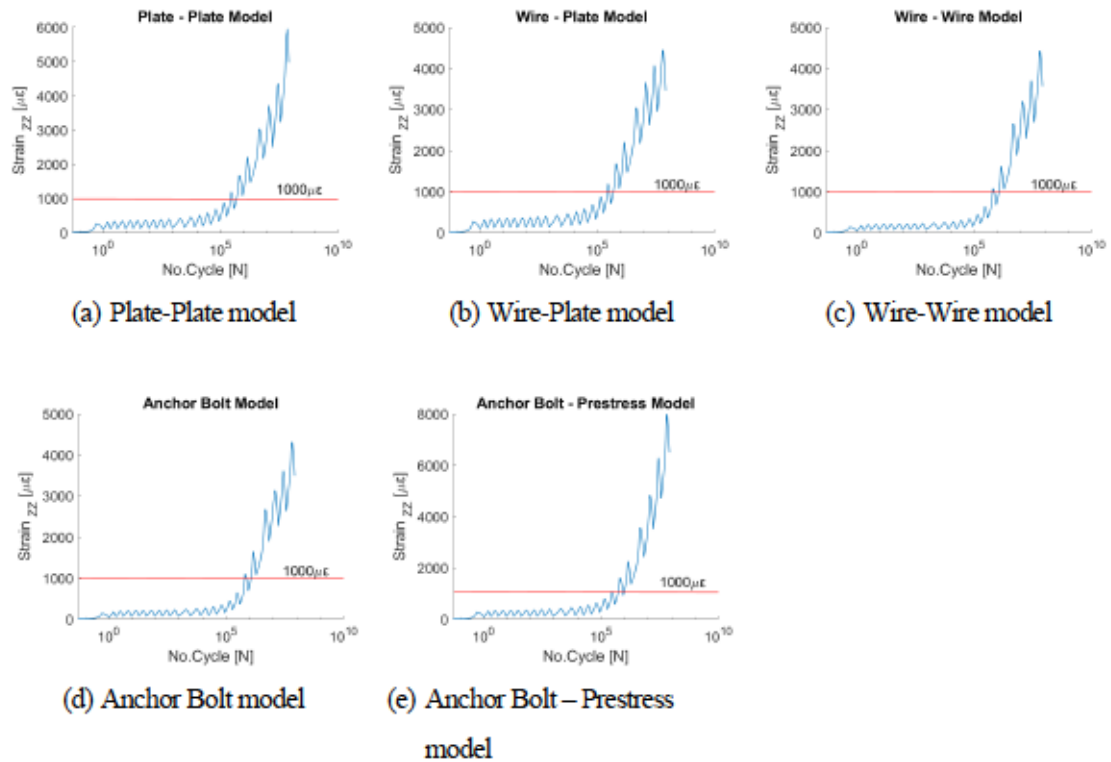
$f_{ctk,min}$  is minimum tensile strength

Figure 6.14 shows stress amplitude and the number of cycles of the critical element under tension. The element has started to lose tensile stiffness at around one million cycles ( $10^6$ ) in all connection types. After that, we can observe tension stiffening behavior, which increases the tensile stiffness after a concrete crack at around ten million ( $10^7$ ) cycles.

As mentioned in Chapter 2, in high cyclic fatigue with low-stress amplitude, tensile fatigue of concrete is attributed to bond creep deterioration and reduction of tension stiffness after the initial cracking. Time-dependent tension creep, path-dependent fracturing, and accumulated fatigue damage become dominant. That the element has lost tensile stiffness because of these sources.



**FIGURE 6.14:** Stress amplitude and the number of cycles of concrete under tension



**FIGURE 6.15:** Tensile strain and the number of cycles of concrete under tension

Figure 6.15 shows the tensile strain and the number of cycles of the critical element under tension. The results complied with Figure 6.14 that the strain suddenly changed to a steep slope after one million ( $10^6$ ) cycles due to loss of tensile stiffness. If the point that tensile strain is over  $1000 \mu\epsilon$  set as the reference point, the fatigue life of the fairlead connections under tensile force can be determined as shown in Table 6.2.

**TABLE 6.2:** Fatigue life approximated by the reference point of tensile strain

Name	No. of Cycle [N]
1. Plate-Plate Model	$4.8789e^5$
2. Wire-Plate Model	$4.8789e^5$
3. Wire-Wire Model	$1.1379e^6$
4. Anchor Bolt Model	$1.0879e^6$
5. Anchor Bolt – Prestress Model	$8.8789e^5$

The results in Table 6.2 show the wire-wire model yields the highest fatigue life with 1.1 million ( $10^6$ ) cycles, the plate-plate and wire-plate models obtained the lowest with 0.49 million ( $10^5$ ) cycles.

On the other hand, the fatigue life evaluated from the model code utilizing Equation 6-1 indicates that under tensile force, the wire-wire model yields the highest number of cycles  $N$  to failure of 0.96 million ( $10^5$ ) cycles, and the anchor bolt-prestress model obtained the lowest of 0.02 million ( $10^4$ ) cycles attributed to higher tensile stress levels ( $S_{ct,max}$ ). The fatigue life and S-N relationship evaluated from the model code are shown in Table 6.3.

**TABLE 6.3:** Fatigue life of the concrete under tensile force evaluated by the model code

Name	$S_{ct,max}$	$LogN$	$N$
1. Plate-Plate Model	0.5837	4.9955	$9.8978e^4$
2. Wire-Plate Model	0.5837	4.9954	$9.8937e^4$
3. Wire-Wire Model	0.5016	5.9809	$9.5689e^5$
4. Anchor Bolt Model	0.5067	5.9200	$8.3180e^5$
5. Anchor Bolt – Prestress Model	0.6413	4.3044	$2.0156e^4$

The concrete fatigue resistance can be determined by applying the tensile stress levels  $S_{ct,max}$  (Table 6.3) and the number of cycles  $N$  (Table 6.2) to the S-N curve of CEB-FIP model code 1990 restriction, as shown in Figure 6.16. The results show all connection types are above the restriction line. However, the expected fatigue life from the reference research [6], [7] mentioned that offshore wind structures must withstand up to 1,000 million ( $10^9$ ) load cycles during their normal design service life of 20 to 25 years. Despite the fact that 1,000 million load cycles seem very huge and hardly occur in real service life, but the lower fatigue life of concrete under tension indicates the possibility of cracking at the fairlead zone, which can be improved in the next design phase.

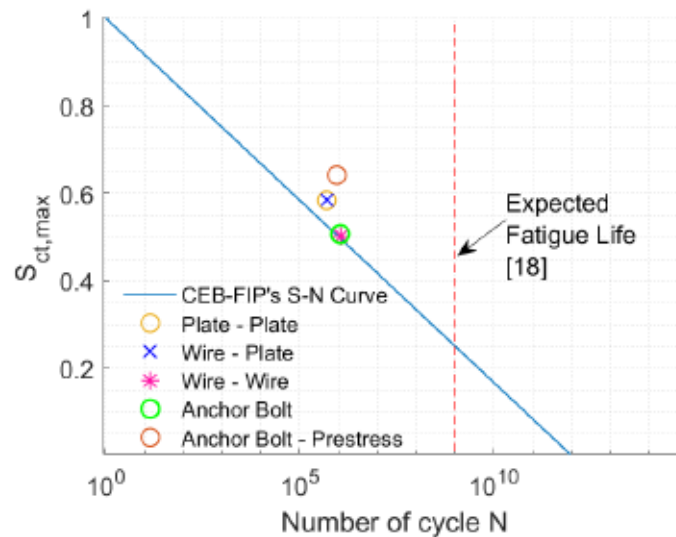


**FIGURE 6.16:** S-N relation of concrete under tension according to the model code

For the concrete under tensile force, we can observe the fatigue life obtained from analysis results is longer than the model code's prediction. As mentioned before, this FE model has installed connection systems, prestressed tendons, and reinforcing bars embedded in the concrete. The interaction of concrete and steel materials in the 3-dimensional FE analysis has significantly played an essential role in the fatigue life of concrete under tension. On the other hand, the model code's formula has predicted the fatigue life based on experimental results of pure concrete material under uniaxial force. Therefore, it is reasonable that, on the



tensile side, the highest number of cycles to failure computed by the model code is lower than those approximated by numerical analysis.

### 6.5.2.2 Fatigue life of concrete under pure compression

According to CEB-FIP model code 1990 [5], the fatigue life of concrete under pure compression can be evaluated from Equations 6-2 to 6-4.

For  $0 \leq S_{c,min} \leq 0.8$

$$\text{Log}N_1 = (12 + 16S_{c,min} + 8S_{c,min}^2)(1 - S_{c,max}) \quad (6-2)$$

$$\text{Log}N_2 = 0.2\text{Log}N_1(\text{Log}N_1 - 1) \quad (6-3)$$

$$\text{Log}N_3 = \text{Log}N_2(0.3 - 0.375.S_{c,max})/\Delta S_c \quad (6-4)$$

here;

If  $\text{Log}N_1 \leq 6$ , then  $\text{Log}N = \text{Log}N_1$

If  $\text{Log}N_1 > 6$ , and  $\Delta S_c \geq 0.3 - 0.375.S_{c,min}$ , then  $\text{Log}N = \text{Log}N_2$

If  $\text{Log}N_1 > 6$ , and  $\Delta S_c < 0.3 - 0.375.S_{c,min}$ , then  $\text{Log}N = \text{Log}N_3$

where;

$S_{c,min}$  is the minimum compressive stress level defined by  $|\sigma_{c,min}/f_{ck,fat}|$

$S_{c,max}$  is the maximum compressive stress level defined by  $|\sigma_{c,max}/f_{ck,fat}|$

$\Delta S_c$  is the stress range

$f_{ck,fat}$  is fatigue reference compressive strength [5], when the age of concrete (compressive strength 41 MPa) at the beginning of fatigue loading after casting is 30 days:  $f_{ck,fat} = 28.75$  Mpa

The compressive stress and the number of cycles of the element under compression in the x, y and z axes obtained from the FE analysis, are shown in Figures 6.17 to 6.19, respectively. Although the amplitudes of the compressive stress are very small in all axes, the highest

compressive stress magnitude occurs on the z-axis, as shown in Figure 6.19. This confirmed the predominant stress amplitude to be taken for fatigue analysis.

In Figure 6.19, we can observe the concrete component started to lose compressive stiffness after applying 10 million cycles ( $10^7$ ); however, the stress amplitudes are relatively small compared to the concrete compressive capacity 41 MPa; thus, it is possible that the concrete crack under compression does not occur.

For a high cycle fatigue of concrete under compression with lower stress levels, the slow-rate creep associated with ambient states in micro-pores becomes predominant. This creep is added to the elasto-plastic and fracture model in the plastic term. It is an irreversible reaction and represented by sliders. Compressive fatigue is attributed to time-dependent plasticity, path-dependent fracturing, as well as accumulated cyclic fatigue damage, as mentioned in Chapter 2. These are the sources that result in the compressive stiffness loss of an element.

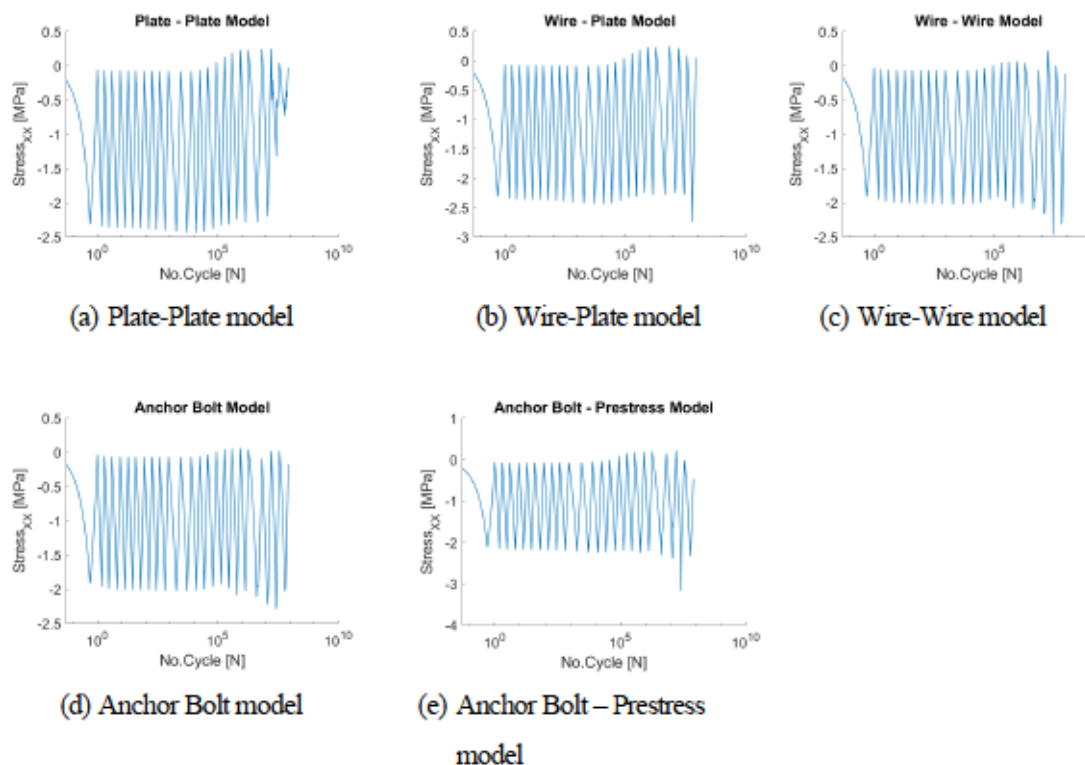


**FIGURE 6.17:** Stress amplitude in the x-axis and number of cycles of concrete under compression

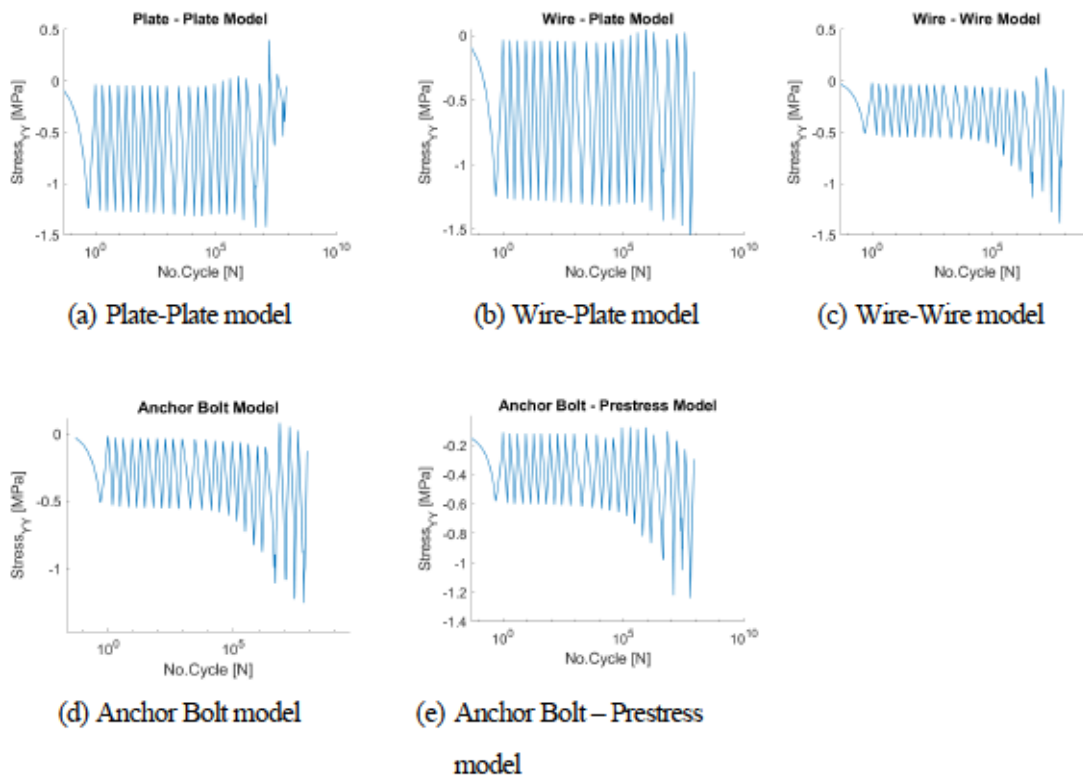


**FIGURE 6.18:** Stress amplitude in the y-axis and number of cycles of concrete under compression

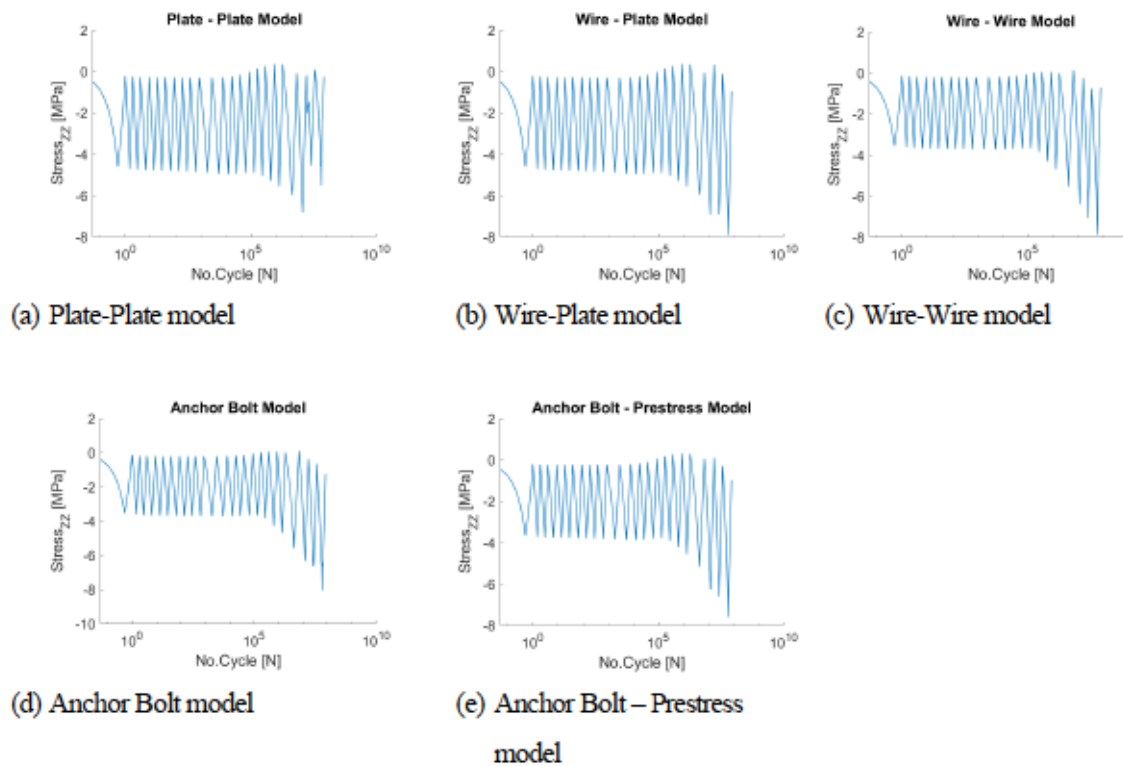


**FIGURE 6.19:** Stress amplitude in the z-axis and number of cycles of concrete under compression

Figure 6.20 shows compressive strain and the number of cycles of the element under compression on the z-axis. We can observe the slope of strain suddenly dropped after applying 1 million ( $10^5$ ) load cycles. However, except for the plate-plate model, the strain amplitudes of other models are small and don't reach the ultimate compressive strain ( $-3000 \mu\epsilon$ ). This means the approximated fatigue life is longer than 84.39 million ( $10^6$ ) cycles, the maximum number of load cycles applied in the analysis. For the plate-plate model, the fatigue life can be approximated at the point that compressive strain has reached the ultimate tensile strain, as shown in Table 6.4.

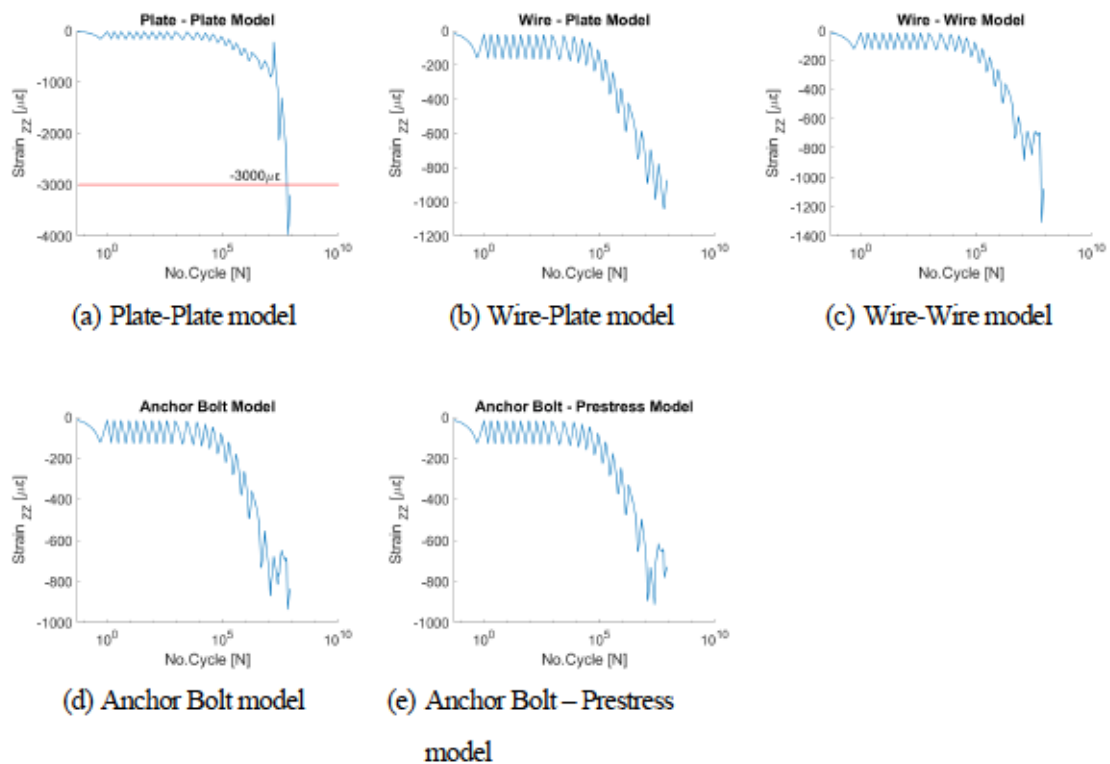


**FIGURE 6.20:** Compressive strain and the number of cycles of concrete under compression

**TABLE 6.4:** Fatigue life approximated by the reference point of compressive strain

Name	$LogN$	$N$
Plate-Plate Model	7.8088	$6.4388e^7$
Wire-Plate Model	$> 7.9263$	$> 8.4388e^7$
Wire-Wire Model	$> 7.9263$	$> 8.4388e^7$
Anchor Bolt Model	$> 7.9263$	$> 8.4388e^7$
Anchor Bolt – Prestress Model	$> 7.9263$	$> 8.4388e^7$

The fatigue life obtained from CEB-FIP model code 1990 utilizing Equations 6-2 to 6-4 is presented in Table 6.5. The results show that under compressive force, the number of load cycles  $N$  that cause fatigue failure is longer than 1000 million ( $10^8$ ) cycles in all models.

**TABLE 6.5:** Fatigue life of the concrete under compression evaluated by the model code

Name	$S_{c,max}$	$S_{c,min}$	$LogN$	$N$
1. Plate-Plate Model	0.2378	0.0127	20.2567	$1.8059e^{20}$
2. Wire-Plate Model	0.2752	0.0127	15.6134	$4.1058e^{15}$
3. Wire-Wire Model	0.2745	0.0048	15.0425	$1.1027e^{15}$
4. Anchor Bolt Model	0.2805	0.0037	14.3720	$2.3552e^{14}$
5. Anchor Bolt – Prestress Model	0.2649	0.0111	16.5989	$3.9714e^{16}$

The concrete fatigue resistance is determined by applying  $S_{ct,max}$  (Table 6.5), and the number of cycles  $N$  (Table 6.4) to the S-N curve of the model code. The results show all connection types are below the restriction line because the maximum load cycles applied in this analysis is around 84.39 million ( $10^6$ ) cycles. This number of load cycles is huge enough to observe the fatigue life of the structure. Nevertheless, except for the plate-plate model, the concrete strain of other models is very small and doesn't reach the ultimate compressive strain suggesting that they are safe from fatigue failure under compression. In this analysis, only the plate-plate model falls into the failure zone; it is at risk of fatigue failure. The design of the plate-plate model can be improved in the next design phase.

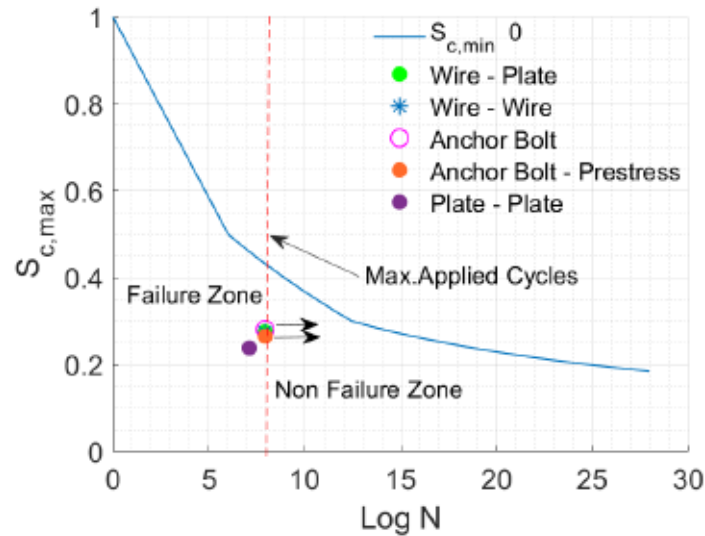


**FIGURE 6.21:** S-N relation according to the model code

Although there is a chance of fatigue failure under compression, keep in mind that it results from a small component taken from a superstructure. Therefore, it doesn't mean the structure will fail if one component failed. The fatigue life of the structure can be so much improved at the next design phase, and this study has suggested that point.

## 6.6 Conclusion for Chapter 6

Five fairlead connection types are proposed and studied. The fatigue life of each type is evaluated, and the following conclusions are obtained.

1. All connection types satisfied the design objective to control crack development at the fairlead connection zone; indicated by concrete tensile strain that is lower than the ultimate tensile strain.
2. The results of the stress-strain distribution obtained from FE analysis of the five connection types show that concrete components located around the top part of the connection plate are under tension; concrete components at the bottom part are under compression. This complies with the load applied to the FE model. The elements with high-stress concentrations are taken from this location to investigate concrete fatigue under tensile and compressive force.

3. The fatigue analysis results of the concrete under tension show the fatigue life estimated by FE analysis is longer than the prediction of the model code. The interaction between concrete and steel materials implemented in 3-dimensional FE analysis is the source of this phenomenon.
4. Under tensile fatigue, the fatigue life evaluated by FE analysis is longer than the model code. However, it is below the expected 1000 million cycles. Lower tensile fatigue life indicates the possibility of cracking at the fairlead zone, which can be improved in the following design phase.
5. Under compressive fatigue, only the plate-plate model has a possibility of fatigue failure. The compressive strain of other connection types doesn't reach the ultimate compressive strain, even if 84 million cycles are applied to the model. The design of the plate-plate model can be improved in the next design phase.
6. Although there is a possibility of fatigue failure under compression, it is the result of a small component taken from a superstructure. This doesn't mean the structure will fail if one component failed. The fatigue life of the structure can be drastically improved at the next design phase, and this study has suggested that point.

### **Nomenclature in Chapter 6**

FE	finite element
FEA	finite element analysis
FEM	finite element model
$f_{ck}$	compressive strength
$f_{ck,fat}$	fatigue reference compressive strength
$f_{ctk,min}$	minimum tensile strength
Hz	Hertz
$LogN$	common logarithm (base 10) of the number of cycles
$N$	the number of cycles
RC	reinforced concrete

$S_{ct,max}$	the maximum tensile stress level
$S_{c,min}$	the minimum compressive stress level
$S_{c,max}$	the maximum compressive stress level
$\Delta S_c$	the stress range
$\sigma_{c,max}$	the maximum compressive stress
$\sigma_{ct,max}$	the maximum tensile stress
$\xi$	magnificent factor
$\mu\epsilon$	micro strain

### References in Chapter 6

- [1] Ueda, Y., and Fujiyama, C., 2017, "Damage Process of Concrete around Anchor Frame inside Footing for Steel Pier," *Procedia engineering*, **171**, pp. 917–925.
- [2] Maekawa, K., Okamura, H., and Pimanmas, A., 2003, *Non-Linear Mechanics of Reinforced Concrete*, CRC Press.
- [3] Maekawa, K., 2008, *Multi-Scale Modeling of Structural Concrete*, Crc Press.
- [4] Quadri, A. I., and Fujiyama, C., 2021, "Numerical Analysis of RC Gerber Bridge Girder Subjected to Fatigue Loading," *Bridge Maintenance, Safety, Management, Life-Cycle Sustainability and Innovations*, H. Yokota, and D.M. Frangopol, eds., CRC Press, pp. 2682–2689.
- [5] 1993, *CEB-FIP MODEL CODE 1990*, Thomas Telford Publishing.
- [6] Mathern, A., von der Haar, C., and Marx, S., 2021, "Concrete Support Structures for Offshore Wind Turbines: Current Status, Challenges, and Future Trends," *Energies*, **14**(7), p. 1995.
- [7] Munbua, W., Hasan, M. S., Malta, E. B., Gonçalves, R. T., Fujiyama, C., and Maekawa, K., 2022, "Conceptual Design of a Prestressed Concrete Spar Floater Supporting a 10 Mw Offshore Wind Turbine," *International Conference on Ocean*,



*Offshore and Arctic Engineering*, American Society of Mechanical Engineers,  
Hamburg, Germany.

## **CHAPTER 7**

### **CONCLUSIONS AND RECOMMENDATIONS**

#### **7.1 General Conclusions**

A precast segment prestressed concrete spar platform intended for mass production capable of supporting a 10 MW offshore RWT is developed and successfully demonstrated in this study as an alternative to a steel spar. Based on the experimental and analytical results, the following conclusions are summarized.

#### **7.2 Coupled Dynamic Analysis of a Floating Wind Turbine**

The geometry of the proposed spar concrete is defined in this chapter, and later it is coupled with the 10MW RWT and mooring lines to perform coupled dynamics analysis. The response motions during the operation of the wind turbine structure are evaluated. The summary of the analytical results is obtained as follows:

1. The proposed concrete spar can be applied to support an RWT. The structure is shown to avoid the structural resonance induced by wave excitation, as confirmed by a spectral analysis that indicates significant response motions that are much smaller than the input wave energies.
2. The motions of the wind turbine determined by OpenFAST calculations indicate that the wind turbine operation increases all significant motions of the spar, particularly the pitch motion. The wind effects must therefore be included in further spar design optimization processes.
3. A rated-wind speed under the storm condition, in which the waves exhibit their highest energy, can be considered as the dominant case for the design of the spar. The highest forces can be expected at the rated wind speed because, at this value, the rotor thrust coefficient that governs the rotor thrust force generated by the control system of the RWT is the highest. Although the typhoon condition produces the highest wind speeds, this wind would result in a relatively small thrust force as the control system will manipulate the wind turbine to shut it down.

### 7.3 Model Test

The experiment with waves of a spar-scaled model 1:100 is performed in the towing tank. The response motions are captured to confirm the hydrodynamic model under wave actions. Based on the experimental results, the following conclusions have been obtained.

1. It is observed that mooring springs installed to protect the model from drifting may affect the response motions, particularly in the low response such as roll, pitch, and yaw motions, as can be observed in the occurrence of a first peak at near-zero frequencies of the response spectrum.
2. The natural periods in 6DOFs obtained from the free vibration test are close to the experiment with waves (except for the roll motion). Therefore, the natural periods' range of the structure is confirmed.
3. The RAOs in the sway, roll, and yaw of the spar are found to be zeroes; therefore, the sway, yaw, and roll motions are not significant for a cylindrical symmetrical shape spar and are possible to be neglected in the motion analysis.
4. The RAOs comparison of the experiment and analytical analysis shows fairly good agreement in terms of the surge and heave motions; however, the analytical results show higher responses in pitch motion.
5. The difference in the pitch response between analytical and experimental results is supposed to cause by viscous damping and hydrodynamic added mass. The higher viscous damping is expected in the real fluid flow, or in another case, it has higher hydrodynamic added mass in the numerical analysis model.
6. The results show the natural periods of the scale model are away from input waves; therefore, it can avoid structural resonance induced by wave excitation.
7. The results obtained from the model test are consistent with the full-scale analysis; therefore, the hydrodynamic model is confirmed.

#### **7.4 Concrete Finite Element Analysis and Structural Design**

The non-linear behavior of spar concrete was investigated in FE analysis. Steel-concrete connections for towers and fairleads, as well as structural design for a prestressed concrete spar floater supporting a 10 MW floating offshore wind turbine, are demonstrated in this study. Based on the results, the following conclusions are earned:

1. The highest hydrodynamic pressure is obtained from a wave heading of  $180^\circ$ , peak period 13.5 seconds (storm wave) of the WAMIT analysis results. This is expected because a storm wave creates the highest wave energy.
2. For a deep draft spar, hydrostatic pressure becomes a dominant force in designing the structure. Hydrodynamic pressure has the highest potential near the seawater surface, but it decreases in the deep water. On the other hand, hydrostatic pressure is relatively large exciting at the bottom part of the spar. This becomes one of the disadvantages of a spar floating platform compared to other short draft floating platform concepts.
3. Although there is a concern that the structural analysis could fail under the large hydrostatic pressure, it is found that, for a spar concrete with thick enough hull thickness, the hull surface becomes under compression. Therefore, it is not necessary to design pretesting force in the horizontal axis to resist any tensile force attributed to water pressure.
4. The FEA results show concrete compressive stress is generally lower than the compressive capacity of the normal strength concrete of 41 MPa applied in this study. Therefore, normal concrete can be used to design a spar concrete to realize an economic structure.
5. The highest stress and strain concentrations occur in the steel-concrete connection parts as expected. A concrete strain that is over the ultimate tensile strain will initiate cracking; this area is highlighted as the critical area for designing prestressing force.
6. The preliminary design of a steel ring with triple rib layers applied at the tower connection can change the pattern of dispersal strain distribution under the steel tower by accumulating at the steel ribs, which is useful for structural design.

7. The preliminary design of the two layers of a steel ring with triple connection plates applied for the fairlead connections successfully resists the large tensile forces transferred from mooring lines to the proposed concrete spar. It can also prevent these forces from transferring to the critical zone located around the tower base area, as confirmed by the concrete strain significantly reduced in the critical element after implementing this connection type.
8. The preliminary connection systems and prestressed design have successfully prevented the steel tower from buckling failure and pulling out of concrete due to the large bending moment under the operation of the wind turbine, as well as the crack generation and propagation in concrete parts of the proposed spar.
9. The proposed prestressed concrete spar can be applied to support an RWT during operation, as shown in the interaction diagram of the section. This is confirmed by FE analysis results that show no structural failure.

## **7.5 Proposed Fairlead Connections**

Five fairlead connection types are proposed and studied. The fatigue life of each type is evaluated, and the following conclusions are obtained.

1. All connection types satisfied the design objective to control crack development at the fairlead connection zone; indicated by concrete tensile strain that is lower than the ultimate tensile strain.
2. The results of the stress-strain distribution obtained from FE analysis of the five connection types show that concrete components located around the top part of the connection plate are under tension; concrete components at the bottom part are under compression. This complies with the load applied to the FE model. The elements with high-stress concentrations are taken from this location to investigate concrete fatigue under tensile and compressive force.
3. The fatigue analysis results of the concrete under tension show the fatigue life estimated by FE analysis is longer than the prediction of the model code. The interaction between concrete and steel materials implemented in 3-dimensional FE analysis is the source of this phenomenon.

4. Under tensile fatigue, the fatigue life evaluated by FE analysis is longer than the model code. However, it is below the expected 1000 million cycles. Lower tensile fatigue life indicates the possibility of cracking at the fairlead zone, which can be improved in the following design phase.
5. Under compressive fatigue, only the plate-plate model has a possibility of fatigue failure. The compressive strain of other connection types doesn't reach the ultimate compressive strain, even if 84 million cycles are applied to the model. The design of the plate-plate model can be improved in the next design phase.
6. Although there is a possibility of fatigue failure under compression, it is the result of a small component taken from a superstructure. This doesn't mean the structure will fail if one component failed. The fatigue life of the structure can be drastically improved at the next design phase, and this study has suggested that point.

## **7.6 Recommendations for the Future Study**

1. This study demonstrates a simplified FE analysis by applying the maximum forces transferred to the spar as timesteps monotonic static loads. In actual behavior, a FOWT is under dynamic excitation attributed to wave and wind action as well as the effects of the wind turbine control system. The dynamic forces should therefore be applied in future FE analyses.
2. The design load cases considered to design a proposed prestressed concrete spar are simplified to nine cases for a feasible study. The load cases are obtained from three wave conditions performed with three wind conditions, considering winds and waves in the co-directional and uni-directional directions. The complete set of design load cases specified in the design standards (e.g., ClassNK, DNV, and IEC) should be applied in future studies.
3. The fatigue assessment of the proposed fairlead connections is evaluated by FE analysis. It should be investigated more in the experiment on the structural scale in future studies.